Proposal to Build an Off-Axis Detector

to Study $\nu_\mu \rightarrow \nu_e$ Oscillations in the NuMI Beamline

NOνA

NuMI Off-Axis ν_e Appearance Experiment

(P929)

March 15, 2004

The NOνA Collaboration

Argonne, Athens, Caltech, UCLA, Cambridge, Fermilab,
College de France, Harvard, Indiana, ITEP, Lebedev,
Louisiana State, Michigan State, Minnesota/Duluth,
Minnesota/Minneapolis, Munich, Stony Brook,
Northern Illinois, Ohio, Oxford, Rio de Janeiro, Rochester,
Rutherford, South Carolina, Stanford, Texas A&M,
Texas/Austin, Tufts, Virginia, Virginia Tech, Washington,
William & Mary, Wisconsin, York

I. Ambats, D. S. Ayres, J. W. Dawson, G. Drake, M. C. Goodman, J. J. Grudzinski, V. J. Guarino, T. Joffe-Minor, D. E. Reyna, R. L. Talaga, J. L. Thron, R. G. Wagner
Argonne National Laboratory, Argonne, IL

D. Drakoulakos, N. Giokaris, P. Stamoulis, S. Stiliaris, G. Tzanakos, M. Zois
University of Athens, Athens, Greece

B. Barish, J. Hanson, D. G. Michael, H. B. Newman, C. W. Peck, C. Smith, J. Trevor, H. Zheng
California Institute of Technology, Pasadena, CA

D. B. Cline, H. Wang, Y. Chen, K. Lee, Y. Seo, X. Yang
University of California, Los Angeles, CA

M. Thomson
University of Cambridge, Cambridge, United Kingdom

J. Beacom, R. Bernstein, G. Bock, S. Brice, L. Camilleri*, S. Childress, B. Choudhary, J. Cooper**, R. Hatcher, D. Harris, J. Hylen, H. Jostlein, D. Koolbeck, J. Kilmer, P. Lucas, V. Makeev, A. Marchionni, O. Mena, S. Mishra, R. Plunkett, S. Parke, S. Pordes, R. Rameika, R. Ray, R. Schmitt, P. Shanahan, P. Spentzouris, R. Wands, R. Yarema
Fermi National Accelerator Laboratory, Batavia, IL

T. Patzak, R. Piteira
College de France, Paris, France

G. J. Feldman**, N. Felt, A. Lebedev, J. Oliver, M. Sanchez, S.-M. Seun
Harvard University, Cambridge, MA

C. Bower, M. Gebhard, M. D. Messier, S. Mufson, J. Musser, B. J. Rebel, J. Urheim
Indiana University, Bloomington, IN

I. Trostin
Institute For Theoretical And Experimental Physics, Moscow, Russia

V. Ryabov, A. Y. Terekhov
P. N. Lebedev Physical Institute, Moscow, Russia

W. Metcalf
Louisiana State University, Raton Rouge, LA

C. Bromberg, J. Huston, R. Miller, R. Richards
Michigan State University, East Lansing, MI

A. Habig
University of Minnesota, Duluth, MN

T. Chase, K. Heller, P. Litchfield, M. Marshak, W. Miller, L. Mualem, E. Peterson, D. Petyt, K. Ruddick, R. Rusack
University of Minnesota, Minneapolis, MN

P. Huber, M. Lindner, W. Winter
Technische Universität München, Munich, Germany

R. Shrock
State University of New York, Stony Brook, NY

C. Albright
Northern Illinois University, DeKalb, IL

C. R. Brune, D. S. Carman, K. H. Hicks, S. M. Grimes, A. K. Opper
Ohio University, Athens, OH

G. Barr, J. H. Cobb, K. Grzelak, N. Tagg
University of Oxford, Oxford, United Kingdom

H. Nunokawa
Pontifícia Universidade Católica do Rio de Janeiro, Rio de Janeiro, Brazil

A. Bodek, H. Budd, S. Manly, K. McFarland, W. Sakumoto
University of Rochester, Rochester, NY

T. Durkin, R. Halsall, T. Nicholls, G. F. Pearce, A. Weber
Rutherford Appleton Laboratory, Chilton, Didcot, United Kingdom

T. Bergfeld, K. Bhaskaran, A. Godley, S. R. Mishra, C. Rosenfeld, K. Wu
University of South Carolina, Columbia, SC

S. Avvakumov, G. Irwin, S. Murgia, S. Wojcicki, T. Yang
Stanford University, Stanford, CA

E. Tetteh-Lartey, M. Watabe, R. Webb
Texas A&M University, College Station, TX

J. Klein, S. Kopp, K. Lang, M. Proga
University of Texas, Austin, TX

H.R. Gallagher, T. Kafka, W.A. Mann, J. Schneps, A Sousa
Tufts University, Medford, MA

C. Dukes, L. Lu, K. Nelson, A. Norman
University of Virginia, Charlottesville, VA

F. F. Chen, K. Creehan, N. K. Morgan, L. Piilonen, R. H. Sturges, R. B. Vogelaar
Virginia Polytechnic Institute and State University, Blacksburg, VA

J. Rothberg, T. Zhao
University of Washington, Seattle, WA

J. K. Nelson
The College of William and Mary, Williamsburg, VA

A.R. Erwin, C. Velissaris
University of Wisconsin, Madison, WI

S. Menary
York University, Toronto, Ontario, Canada

* On leave from CERN
** Temporary Co-Spokespersons

Table of Contents

1. Executive Summary

1.1. The Physics of NOνA

The past two decades have seen great advances in our understanding of neutrinos. Underground experiments detecting neutrinos produced in the sun and in the earth's atmosphere have shown that neutrinos have mass and that they oscillate from one species to another as they travel. These oscillations arise because the neutrino species produced in particle decays (electron, muon, and τ-type neutrinos) do not have specific masses but are combinations of neutrino species (simply called 1, 2, and 3-type neutrinos) that do have specific masses. The average distance a neutrino travels before it oscillates is proportional to its energy and inversely proportional to the difference of the squares of masses of the underlying species of neutrinos. The probability that an oscillation will occur is related to a parameter known as a mixing angle.

The neutrinos that come from the sun are electron-type neutrinos that oscillate to muon and τ-type neutrinos, characterized by the mixing angle θ_{12} and an oscillation length (normalized to an energy of 2 GeV) of approximately 35,000 km. Neutrinos produced by cosmic rays in the earth's atmosphere are primarily muon-type neutrinos that oscillate to τ–type neutrinos, characterized by the mixing angle θ_{23}, and an oscillation length (again normalized to an energy of 2 GeV) of approximately 1,000 km. A third type of neutrino oscillation is possible: the oscillation of muon-type neutrinos to electron-type neutrinos at the atmospheric oscillation length. These neutrino oscillations, which so far have not been observed, would be characterized by the mixing angle θ_{13}. The study of this last category of neutrino oscillations is the main goal of NOνA (**N**uMI **O**ff-Axis ν_e **A**ppearance Experiment)[1].

The significance of the search for these oscillations is that if they exist, i.e., if θ_{13} is not zero, then we will ultimately be able to determine the ordering of the neutrino masses and measure CP violation in neutrino oscillations. There is widespread belief that the very small neutrino masses are related to physics at an extremely high-energy scale, one that cannot be studied directly with accelerator beams. There is also theoretical speculation that CP violation by neutrinos could be one aspect of understanding why the universe is composed solely of matter, rather than equal amounts of matter and antimatter.

MINOS is one of the first generation of long baseline accelerator-based neutrino oscillation experiments.[2] This Fermilab experiment, which has a 730 km baseline, will start taking data in early 2005. The MINOS Far Detector is located in the lowest level of the Soudan mine in northern Minnesota and it sits directly on the center of the Fermilab NuMI neutrino beam line. The physics goals of the MINOS experiment are to verify the atmospheric neutrino oscillations, to improve the measurement of their parameters, and to perform a low-sensitivity measurement of θ_{13}.

We are proposing NOνA to utilize Fermilab's investment in the NuMI beamline by building a second-generation detector, which will have the primary physics goal of measuring θ_{13} with approximately a factor of 10 more sensitivity than MINOS. To accomplish this we make three major improvements on the MINOS detector:

(1) We increase the mass of the detector by a factor of 9, from 5.4 kT for MINOS to 50 kT for

[1] It is also possible that in addition to the three types of neutrinos produced in particle decays and interactions, there could exist additional types of neutrinos that are not produced in these decays and interactions. There is unconfirmed evidence for the existence of this type of neutrino, called a sterile neutrino, from an experiment at Los Alamos National Laboratory. This result is currently being checked by a Fermilab experiment, MiniBooNE. If the existence of sterile neutrinos is confirmed, it will greatly enrich the already rich physics of neutrino oscillations. Searching for evidence of sterile neutrinos will be part of the NOνA physics program.

[2] The other two first-generation experiments are K2K, an experiment in Japan now running over a 250 km baseline, and CNGS, an experiment in Europe over a 730 km baseline, that will start in 2006.

NOνA. At the same time, we decrease the cost per kT by about a factor of 3.

(2) We design a detector that is optimized for the identification of electron-type neutrino events. Specifically, we increase the longitudinal sampling from once every 1.5 radiation lengths[3] in MINOS to once every 0.3 radiation lengths in NOνA.

(3) We position the detector not directly on the NuMI beam, as MINOS is, but 10 to 14 km off the central part of the beam. This provides more neutrino events in the energy range in which the oscillation takes place, and fewer background events.

Once a signal for electron-type neutrino appearance is seen, NOνA can run an antineutrino NuMI beam to attempt to measure the ordering of the neutrino masses. Whether this will be successful will depend on the parameters that nature has chosen. However, the sensitivity of NOνA can be markedly increased by a five-fold increase in the NuMI beam intensity created by the construction of the Fermilab Proton Driver. Smaller, but still quite significant, increases in NOνA sensitivity can be provided much sooner by modest investments in the Fermilab accelerator complex, for example, by reducing the Main Injector cycle time to give more protons per year on the NuMI beamline target.

Since there are three unknown parameters to be measured — θ_{13}, the ordering of the mass states, and the parameter that measures CP violation — a third measurement may eventually be required in addition to neutrino and antineutrino measurements in NOνA to determine all three parameters. The third measurement could be done by moving the NOνA detector, building an additional detector on the NuMI beamline, rebuilding the NuMI beamline to point in a slightly different direction, or combining NOνA measurements with those taken elsewhere on different length baselines. Such experiments are being contemplated in Europe and Japan.[4]

We view NOνA as a second step in a step-by-step Fermilab program to measure all of the unknown parameters of neutrino oscillations. Each step will provide guidance on the optimum direction for the succeeding step.

1.2. The NOνA Detectors

The NOνA Far Detector will be a sandwich detector, like MINOS, with alternating layers of passive absorber and active detector elements. The iron absorber of MINOS will be replaced by particleboard in order to increase the ratio of radiation length to mass. The active absorber in MINOS is solid scintillator strips read out through wavelength-shifting fibers to multi-anode photomultipliers. Our baseline design for NOνA calls for liquid scintillator encased in 14.6 m long 30-cell titanium dioxide-loaded PVC extrusions. The 4 cm wide liquid scintillator cells are read out by U-shaped wavelength-shifting fibers into avalanche photodiodes (APDs). This configuration gives better performance at lower cost than that of MINOS. The liquid scintillator is less expensive than solid scintillator and less costly to assemble. The APDs provide much higher quantum efficiency than photomultipliers and are cheaper. The high quantum efficiency of the APDs allows longer scintillator cells than those in MINOS.

However, this design is not without challenges. The APDs have very low gain requiring very low noise electronics. They must also be cooled to –15 C to reduce the noise level to an acceptable level. As part of our R&D plan for the coming year, we must verify the performance of the full liquid scintillator system.

---

[3] A radiation length is the average distance in which an electron loses 63% of its energy.

[4] T2K, a second-generation experiment being built in Japan, will send an off-axis beam from JPARC to the 50 kT SuperKamiokande detector over a 295 km baseline. It plans to begin operation in 2008. A possible future third-generation experiment on this baseline involves increasing the JPARC intensity by a factor of five and building a new detector with 20 times the mass of SuperKamiokande. There is discussion in Europe on building a third-generation experiment using a proposed CERN proton driver called the SPL. It would provide both a conventional neutrino beam and a beam based on the decay of accelerated ions (called a beta beam) over a 130 km baseline to a new, very massive detector to be built in the Frejus tunnel. It should be noted that neither of these proposed third-generation experiments would have a sufficiently long baseline to resolve the ordering of the neutrino mass states without NOνA data.

We have also developed an alternative technology for the active detectors — resistive plate chambers (RPCs) similar to those used in the BELLE experiment. We plan to review the R&D on both active detectors in December 2004 and come to a final decision on the active detector technology.

We have identified three acceptable sites for the Far Detector, two in Minnesota and one in Ontario. The baseline site is near Ash River, Minnesota, about 810 km from the NuMI target.

Unlike MINOS, the NOνA Far Detector will sit on the earth's surface. With the planned active shield on the top and sides of the detector, our calculations indicate that backgrounds from cosmic radiation will be acceptably low, largely due to the very short beam pulses from Fermilab, one 10 μs pulse every 2 seconds. Part of our R&D program is to verify these calculations with an experimental measurement in a prototype detector.

Like MINOS, NOνA will be a two-detector experiment. A small near detector with, as far as possible, the identical structure of the far detector will be constructed on the Fermilab site. Its function is to predict the expected rates of event types and their energy spectra in the far detector in the absence of oscillations. Differences seen between the events in the two detectors can then be attributed to oscillations.

We have constructed a detailed cost estimate for the full baseline experiment, including a generous contingency for items that have not yet been fully designed. The fully burdened cost in FY2004 dollars is 147.3 M$, of which 44.3 M$ is assigned to contingency.

Our technically driven schedule calls for Fermilab Stage 1 approval in June 2004, and a final active detector technology decision in December 2004, followed by full Fermilab approval in June 2005. Construction funding beginning October 2006 will allow the Near Detector and 15% of the Far Detector to be completed by October 2008, with the full Far Detector to be completed by the end of December 2011. Since the NuMI beam will be available throughout this entire period and the Far Detector is modular, we will be able to begin taking useful data in October 2008.

2. Introduction

In recent years, underground experiments have provided convincing evidence of neutrino oscillations of both solar and atmospheric neutrinos. With these measurements, we have an emerging framework with a rich structure in the lepton sector, which we can compare with a structure in the quark sector that has been studied for more than 25 years. An intriguing possibility is that CP violation exists in the lepton sector and that this asymmetry is somehow related to the fundamental matter-antimatter asymmetry of our Universe.

The flavor-changing transitions observed in atmospheric and solar neutrinos are most naturally described by a simple extension to the Standard Model, in which three types of neutrinos have masses and mix with each other. The three well-known flavor eigenstates, the electron, muon and tau neutrinos, are related to these mass eigenstates by the (3×3) unitary MNS matrix. The model explains the observed flavor-changing transitions as neutrino oscillations, described by mass differences Δm_{ij} and mixing angles θ_{ij} (which are parameters of the MNS matrix). The model also provides for CP violation in a natural way through a phase (δ) in the MNS matrix.

While measurements of atmospheric and solar neutrino oscillations have provided some information about the mass differences and two of the three mixing angles, we have (*e.g.,* from the CHOOZ reactor experiment) only an upper limit on the third mixing angle, θ_{13}. Measuring this parameter is key to obtaining a complete picture of the structure of the lepton sector. In particular, a non-zero value for θ_{13} is a prerequisite to both the ability to probe leptonic CP violation in the leptonic sector and to resolve the ordering of neutrino mass states. The latter can only be determined by matter effects, which occur when electron-type neutrinos propagate long distances through the earth. These measurements are the goal of the NuMI Off-Axis ν_e Appearance experiment (NOνA) described in this proposal.

Chapter 1 of the proposal provides an Executive Summary. Chapter 2 is this introduction. The body of the proposal begins with Chapter 3, which is a concise discussion of the physics motivation. This chapter provides a framework for understanding how the results of this proposed experiment relate to the results of other lepton sector experiments.

An overview of the proposed experiment is provided in Chapter 4. Essentially, we intend to measure electron neutrino appearance in a 50,000 metric ton far detector that will be located about 810 km from Fermilab and 10-14 km off the central axis of the NuMI beam. This off-axis location provides a lower energy, more monoenergetic neutrino beam, which is better suited for this measurement than the on-axis beam. A near detector will measure the electron neutrino content of the beam at Fermilab, characterize the detector response to neutrino events and perform crucial background studies. The NOνA Far Detector will be optimized to separate charged current electron-neutrino events from neutrino events producing neutral pions. The proposed detector is a planar tracking calorimeter with low-density, low-Z, wood absorber and active tracking elements located every 1/3 of a radiation length. In the baseline design, the active elements are ~540,000 cells filled with liquid scintillator. Each cell is 2.5 cm × 4 cm × 14.6 m and is grouped together with 29 other cells in a single PVC extrusion. The scintillator will be read out with wavelength-shifting fibers and avalanche photodiodes. We are also developing an alternate design with glass resistive plate chambers (RPCs) as the active tracking elements. This alternate is described in the Appendix.

Chapter 5 presents additional discussion of the possible contribution of this experiment to the ultimate understanding of the mixing parameters in the lepton sector and possible leptonic CP violation. It is likely that multiple experiments, possibly using both neutrino beams and neutrinos from reactors, will be required to fully measure the several leptonic mixing parameters. Chapter 6 provides information about the design methodology for the Far Detector and the several technologies that were considered in the design process. The details of the baseline detector design are described in Chapter 7. The detector consists of three mostly independent systems: the passive absorber, the active scintillator and the photodetectors. It is in many ways similar to the MINOS detector and the active detector design borrows heavily from

MINOS. Simulations of the NOνA Detector also make extensive use of the code developed for MINOS. These simulations have motivated a likelihood analysis algorithm for NOνA events. The details of this algorithm and the results of these simulations are described in Chapter 8. Chapter 9 discusses potential backgrounds to the electron neutrino oscillation signal and the use of the NOνA Near Detector in determining background levels in the Far Detector signal. Chapter 10 estimates the cosmic ray background resulting from the detector's location on the earth's surface and describes the active shield we plan to implement around the detector.

Chapter 11 provides information about three possible sites for the Far Detector, two in Minnesota and one in Ontario. The "baseline" site is close to the northernmost road in the United States near the NuMI beamline, known as the Ash River Trail. We also describe the preliminary design of the building required to house the detector.

The sensitivity of this experiment depends on the product of the detector acceptance—size and sensitivity—and the beam intensity. Chapter 12 discusses beam requirements for this experiment. We also discuss the impact of the proposed Fermilab Proton Driver on this program. Although the Proton Driver is not required for the first phase of the experiment, it provides a natural upgrade path for a Fermilab world-leading program in understanding the physics of the lepton sector. Chapter 13 summarizes our current cost and schedule estimates for the experiment. As already indicated, the Appendix provides additional information about resistive plate chambers (RPCs) as a tracking technology for the Far Detector.

In essence, we lay out in this proposal a major step in a program of experiments to study couplings in the lepton sector, with an eventual goal of measuring leptonic CP violation. NOνA is a natural next step after MINOS. Once this experiment determines the θ_{13}-coupling, it will be possible at Fermilab, likely with the Proton Driver, to go on to the next phase of mass hierarchy and leptonic CP measurements.

When the first neutrinos appear in the NuMI beamline about 9 months from now, they will represent a very significant step forward for particle physics. At a length of more than 800 km, the NOνA baseline will be nearly three times as long as the baseline in T2K (JPARC Phase 1) and somewhat longer than the baseline from CERN to Gran Sasso. Thus, with the NuMI beam, Fermilab has a unique capability to answer some of the most important questions that can be asked in elementary particle physics, both today and in the foreseeable future.

3. Physics Motivation

3.1. Introduction

Recently the SuperKamiokande [1], K2K [2] and Soudan 2 [3] experiments have provided very strong evidence that the muon neutrino undergoes flavor changing transitions. These transitions are seen for neutrinos whose path length divided by energy (L/E) is of order ~500 km/GeV. Super-Kamiokande also has some supporting evidence that muon neutrinos are transformed primarily into tau neutrinos. Although the SuperKamiokande detector has some sensitivity to flavor transitions of electron neutrinos, their data provides no evidence that electron neutrinos are involved in these transitions. In fact, the CHOOZ [4] reactor experiment provides a tighter constraint on the upper limit on the probability of electron neutrino flavor transitions of order 5-10%, at the values of L/E for which SuperKamiokande sees muon neutrino flavor transitions. This leaves open the interesting and important question: What is the role of the electron neutrino in flavor transitions at these values of L/E? A measurement or stringent limit on the probability of $\nu_\mu \rightarrow \nu_e$ for values of L/E of order 500 km/GeV is an important step in understand these neutrino flavor transitions in atmospheric neutrinos. As the NuMI beam is primarily a ν_μ beam, the observation of ν_e appearance would address this question directly. This measurement is the primary goal of the experiment described by this proposal.

The SNO [5] experiment has recently reported large transitions of solar electron neutrinos to muon and/or tau neutrinos both with and without salt added to the heavy water. SuperKamiokande [6] studying solar neutrinos and KamLAND [7] studying reactor neutrinos also see large electron neutrino flavor transitions. From a combined analysis, the L/E for these flavor transitions is a factor of ~30 times larger than the L/E for flavor transitions in atmospheric muon neutrinos. These transitions occur for an L/E such that the transition probability $\nu_\mu \rightarrow \nu_e$ measured by an experiment in the NuMI beam will also have some sensitivity to the flavor transitions associated with solar neutrinos through interference effects.

The LSND [8] experiment has reported small muon anti-neutrino to electron anti-neutrino transitions for values of L/E that are less than two orders of magnitude smaller than the transitions seen in atmospheric neutrinos. However this transition probability is very small, on the order of 0.3% of the one observed for atmospheric and solar neutrinos. If this result is confirmed by the mini-BooNE [9] experiment, this transition could be an important background for a measurement of $\nu_\mu \rightarrow \nu_e$ transitions at the larger values of L/E associated with atmospheric neutrinos.

3.2. Neutrino Mixing

Extensions to the Standard Model are required to explain the phenomena described here. The simplest and most widely accepted extension is to allow the neutrinos to have masses and mixings such that these phenomena are explained by neutrino oscillations. The masses and mixing of the neutrinos in these extensions would be the low energy remnant of some yet to be determined high energy physics. Thus, neutrino masses and mixing provide a unique window on physics that is inaccessible to current or near future collider experiments. One popular theory is the so called "seesaw" scenario where the active left handed neutrinos seesaw off their heavier right handed (sterile) partners leaving three very light Majorana neutrinos. It is already clear that the masses and mixings in the neutrino sector are very different from the masses and mixings in the quark sector and that a detailed understanding of the neutrino masses and mixings will be important in differentiating fermion mass theories. Also, they may provide the key to advancing our theoretical understanding of this fundamental question.

If the neutrinos have masses and mixings then the neutrino mass eigenstates, $\nu_i = (\nu_1, \nu_2, \nu_3, \ldots)$ with masses $m_i = (m_1, m_2, m_3, \ldots)$ are related to the flavor eigenstates $\nu_\alpha = (\nu_e, \nu_\mu, \nu_\tau, \ldots)$ by the equation

$$|\nu_\alpha\rangle = \sum_i U_{\alpha i} |\nu_i\rangle \qquad (1)$$

The charged weak current, for the neutrino flavor states, is given by $J_\lambda = \overline{\nu}_L \gamma_\lambda \ell_L$, where $\ell = (e, \mu, \tau)$ is the vector of charged lepton mass eigenstates. In the absence of light sterile neutrinos, the 3 × 3 lepton mixing matrix U is unitary. Lepton flavor mixing was first discussed (for the 2 × 2 case) by Maki, Nakagawa, and Sakata.

If we restrict the light neutrino sector to the three known active flavors and set aside the LSND results[1], then the unitary matrix MNS matrix, U, can be written as

$$U = \begin{pmatrix} c_{13}c_{12} & c_{13}s_{12} & s_{13}e^{-i\delta} \\ -c_{23}s_{12} - s_{13}s_{23}c_{12}e^{i\delta} & c_{23}c_{12} - s_{13}s_{23}s_{12}e^{i\delta} & c_{13}s_{23} \\ s_{23}s_{12} - s_{13}c_{23}c_{12}e^{i\delta} & -s_{23}c_{12} - s_{13}c_{23}s_{12}e^{i\delta} & c_{13}c_{23} \end{pmatrix} \quad (2),$$

where $c_{jk} \equiv \cos\theta_{jk}$ and $s_{jk} \equiv \sin\theta_{jk}$.

With this labeling, the atmospheric neutrinos oscillations are primarily determined by the θ_{23} and Δm^2_{32} parameters, whereas the solar neutrino oscillations depend on θ_{12} and Δm^2_{12}, where $\Delta m^2_{ij} = m^2_i - m^2_j$. From SuperKamiokande we already have some knowledge of $|\Delta m_{32}{}^2| = (1.5 - 3.5)\times 10^{-3}$ eV^2 and $0.35 < \sin^2\theta_{23} < 0.65$ (*i.e.*, $\sin^2 2\theta_{23} > 0.91$). Note the substantial uncertainty in these atmospheric measurements. In contrast, the combined analysis of the SNO, SK and KamLAND experiments gives $\Delta m^2_{21} = +7.1 \pm 2.0 \times 10^{-5}$ eV^2 and $\sin^2\theta_{12} = 0.5$ excluded at more than 5σ. This corresponds to $0.71 < \sin^2 2\theta_{12} < 0.91$. For the purposes of this experiment our knowledge of the solar parameters is already in good shape and is expected to improve with time.

CHOOZ (and SuperK) provide us with a limit on $\sin^2 2\theta_{13} < 0.18$. The CHOOZ limit is dependent on the input value used for $|\Delta m_{32}{}^2|$; for the current central value 2.5 $\times 10^{-3}$ eV^2, this limit is $\sin^2 2\theta_{13} < 0.14$, while for $|\Delta m_{32}{}^2| = 2.0\times 10^{-3}$ eV^2, it is $\sin^2 2\theta_{13} < 0.18$ [4]. Thus, the proposed long-baseline neutrino oscillation experiment to search for $\nu_\mu \to \nu_e$ will be sensitive to a substantial range below this upper bound.

The MINOS experiment [10] will provide a 10% measurement of the atmospheric Δm^2_{32} but probably will not improve our knowledge of θ_{23}. This experiment has sensitivity to $\sin^2 2\theta_{13}$ only about a factor of two below the CHOOZ bound. Any future reactor experiment to measure $\sin^2 2\theta_{13}$ could improve our knowledge of this important parameter but such an experiment has no sensitivity to θ_{23}, the sign of Δm^2_{32} or the CP violating phase δ. Therefore, such a reactor experiment is truly complementary to long-baseline experiments to observe $\nu_\mu \to \nu_e$.

The appearance probability of ν_e in a ν_μ beam in vacuum is given, to leading order, by

$$P_{vac}(\nu_\mu \to \nu_e) = \sin^2\theta_{23} \sin^2 2\theta_{13} \sin^2\Delta_{atm} \quad (3),$$

where $\Delta_{atm} \approx 1.27\left(\frac{\Delta m^2_{32} L}{E}\right)$. If the experiment is performed at one of the peaks of this probability, that is, when $\Delta_{atm} = \frac{\pi}{2} + n\pi$, then

$$P_{vac}(\nu_\mu \to \nu_e) = \frac{1}{2}\sin^2 2\theta_{13} = 2.5\%\left(\frac{\sin^2 2\theta_{13}}{0.05}\right) \quad (4)$$

The first peak occurs at neutrino energy,

$$E = 1.7\ \text{GeV}\left(\frac{\Delta m^2_{32}}{2.5\times 10^{-3}\text{eV}^2}\right)\left(\frac{L}{820\ \text{km}}\right) \quad (5)$$

The constraint on $\sin^2(2\theta_{13})$ from the CHOOZ experiment varies from 0.14 to 0.18 depending on the atmospheric Δm^2_{32}, therefore the maximum appearance probability ranges from ~7 to 9%. To be effective any ν_e appearance experiment has to aim to exclude or convincingly see a signal at least an order of magnitude below this 7% limit.

3.3. Matter Effects

The neutrinos in the NuMI beam propagate through the Earth and matter induced contributions to the propagation amplitude are non-negligible. These matter effects have opposite sign for neutrinos and anti-neutrinos and for the normal versus inverted neutrino mass hierarchies. The matter effects can be thus used to distinguish the two possible three-neutrino mass hierarchies, see Fig. 3.1. If the experiment is performed at the first peak in the oscillation, as above, the matter effects are primarily a function of the energy of the neutrino beam and the transition probability in matter can be approximated by

$$P_{mat}(\nu_\mu \to \nu_e) \approx \left(1 \pm 2\frac{E}{E_R}\right) P_{vac}(\nu_\mu \to \nu_e) \quad (6),$$

where E_R is the matter resonance energy associated with the atmospheric Δm^2, that is

[1] In the 3+1 neutrino mass hierarchy the LSND result can be accommodated as a perturbation on the pure active 3 neutrino hierarchy. The 2+2 mass hierarchy would require major modifications.

$$E_R = \frac{\Delta m^2_{32}}{2\sqrt{2}G_F N_e} = 12\ \text{GeV}\left(\frac{\Delta m^2_{32}}{2.5\times10^{-3}\ \text{eV}^2}\right)\left(\frac{1.4\ \text{g cm}^{-3}}{\text{Y}_e\rho}\right) \quad (7),$$

where N_e is the electron number density in the earth, ρ is the matter density (2.8 g.cm^{-3}) and $Y_e = \frac{1}{2}$ is the electron fraction.

For the normal hierarchy, matter effects enhance (suppress) the transition probability for neutrinos (anti-neutrinos) and vice versa for the inverted hierarchy. For a 2 GeV neutrino energy, matter effects give a 30% enhancement or suppression in the transition probability.

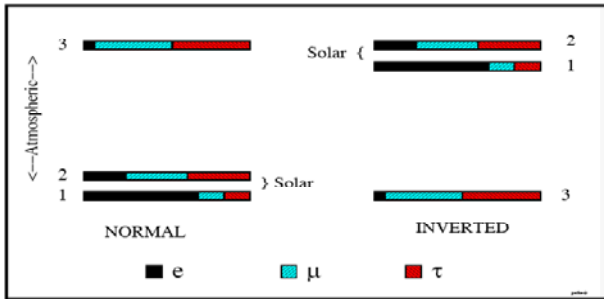

Fig. 3.1: The two allowed three-neutrino mass squared spectra that account for the oscillations of solar and atmospheric neutrinos. The normal spectrum has $\Delta m^2_{32} > 0$ and the inverted has $\Delta m^2_{32} < 0$. The ν_e fraction of each mass eigenstate is indicated by the black solid region, whereas the ν_μ (ν_τ) fraction is indicated by the blue-green right-leaning (red left-leaning) hatching. The ν_e fraction in the mass eigenstate labeled, 3, has been enhanced for clarity.

3.4. CP Violation

Now that the solution to the solar neutrino puzzle consistent with neutrino oscillations is the "Large Mixing Angle" (LMA) region the $\nu_\mu \to \nu_e$ transition probability is sensitive to sub-leading effects and in particular to the CP violating phase δ.

In vacuum the shift in the transition probability associated with the CP violating phase is given by

$$\Delta P_\delta(\nu_\mu \to \nu_e) \approx J_r \sin\Delta_{sol} \sin\Delta_{atm}\left(\cos\delta\cos\Delta_{atm} \mp \sin\delta\sin\Delta_{atm}\right) \quad (8),$$

where the minus (plus) sign is for neutrinos (anti-neutrinos),

$$J_r = \sin2\theta_{12}\sin2\theta_{23}\sin2\theta_{13}\cos\theta_{13}$$
$$J_r \approx 0.9\sin2\theta_{13} \quad (9)$$

$$\Delta_{sol} = 1.27\frac{\delta m^2_{21}L}{E} = \frac{\delta m^2_{21}}{\delta m^2_{32}}\Delta_{atm} \approx \frac{1}{36}\Delta_{atm}. \quad (10)$$

At the first oscillation maximum of the atmospheric Δm^2 scale, the shift in the transition probability dependent on δ is of order

$$\left|\Delta P_\delta\left(\nu_\mu \to \nu_e\right)\right| \sim 0.6\%\sqrt{\frac{\sin^2 2\theta_{13}}{0.05}} \quad (11)$$

Note that is shift is proportional to $\sqrt{\sin^2 2\theta_{13}}$, while the leading term is proportional to $\sin^2 2\theta_{13}$. Thus, the relative importance of the sub-leading terms grows as $\sin^2 2\theta_{13}$ gets smaller.

The full transition probability, in vacuum, is given by

$$P(\nu_\mu \to \nu_e) = \left|\sum_{j=1}^{3} U^*_{\mu j}U_{ej}e^{-i\left(m_j^2 L/2E\right)}\right|^2 \quad (12)$$
$$= \left|2U^*_{\mu3}U_{e3}e^{-i\Delta_{32}}\sin\Delta_{31} + 2U^*_{\mu2}U_{e2}\sin\Delta_{21}\right|^2$$

The second form of this probability is especially illuminating as the first term is the amplitude for $\nu_\mu \to \nu_e$ associated with the atmospheric Δm^2 and the second term the amplitude associated with the solar Δm^2. The interference between these two amplitudes differs for neutrinos and anti-neutrinos because for anti-neutrinos the U matrix is replaced with U^*. This difference in the interference term leads to the difference in the transition probability $\nu_\mu \to \nu_e$ between neutrino and anti-neutrinos. Such an effect is an example of CP violation.

Using the MNS mixing matrix given in Eq. 2,

$$2U^*_{\mu3}U_{e3} = e^{-i\delta}\sin2\theta_{13}\sin\theta_{23}$$
$$2U^*_{\mu2}U_{e2} = \sin2\theta_{12}\cos\theta_{23}\cos\theta_{13} + O\left(\sin\theta_{13}\right) \quad (13)$$

Since the $O\left(\sin\theta_{13}\right)$ term is multiplied by $\sin\left(\Delta_{21}\right)$ in the amplitude, it is quadratic in the small quantities sin θ$_{13}$ and the solar Δm^2 and therefore can be neglected.

$$P\left(\nu_\mu \to \nu_e\right) =$$
$$\left|e^{-i(\Delta_{32}+\delta)}\sin2\theta_{13}\sin\theta_{23}\sin\Delta_{31}\right. \quad (14)$$
$$\left. + \sin2\theta_{12}\cos\theta_{23}\cos\theta_{13}\sin\Delta_{21}\right|^2$$

$$P(\nu_\mu \to \nu_e) =$$
$$\sin^2\theta_{23}\sin^2 2\theta_{13}\sin^2\Delta_{31}$$
$$+\cos^2\theta_{13}\cos^2\theta_{23}\sin^2 2\theta_{12}\sin^2\Delta_{21} \quad (15)$$
$$+J_r \sin\Delta_{21}\sin\Delta_{31}$$
$$(\cos\Delta_{32}\cos\delta - \sin\Delta_{32}\sin\delta)$$

The first and second terms are the probability of $\nu_\mu \to \nu_e$ associated with the atmospheric and solar Δm^2 's respectively, whereas the third term is the interference between these two probabilities. The term proportional to sin δ is responsible for CP violation since it changes sign when going from neutrinos to anti-neutrinos[2].

To show the growing importance of the CP violating term as $\sin^2 2\theta_{13}$ gets smaller we have plotted the neutrino anti-neutrino asymmetry, $|P_\nu - P_{\bar\nu}|/(P_\nu + P_{\bar\nu})$ versus $\sin^2 2\theta_{13}$ in Fig. 3.2 at the first oscillation maximum assuming maximum CP violation, *i.e.* $\Delta_{31} = \pi/2$ and $\delta = \pi/2$. The asymmetry grows as $\sin^2 2\theta_{13}$ gets smaller until the amplitude for $\nu_\mu \to \nu_e$ from the atmospheric Δm^2 is equal in magnitude to the amplitude from the solar Δm^2. At this value of $\sin^2 2\theta_{13}$ there is maximum destructive (constructive) interference for neutrinos (anti-neutrinos) and therefore a maximum asymmetry of unity. The value of $\sin^2 2\theta_{13}$ at this peak asymmetry is given by

$$\sin^2 2\theta_{13}\,|_{peak} \approx \frac{\sin^2 2\theta_{12}}{\tan^2\theta_{23}}\left(\frac{\pi}{2}\frac{\Delta m^2_{21}}{\Delta m^2_{31}}\right)^2 \sim 0.002 \quad (16)$$

Even at the CHOOZ bound for $\sin^2 2\theta_{13}$ the asymmetry is greater than 20%. This asymmetry scales as sin δ for values of δ away from π/2.

[2] The inclusion of the $O(\sin\theta_{13})$ terms in $U^*_{\mu 2}U_{e2}$ gives the full expression for $P(\nu_\mu \to \nu_e)$ by multiplying the first term by $(1 - 2\sin^2\theta_{12}\sin\Delta_{12}\cos\Delta_{32}/\sin\Delta_{31})$ and the second term by $|1 - e^{-i\delta}\sin\theta_{13}\tan\theta_{12}\tan\theta_{23}|^2$, while the third term is unchanged. Both of these factors are very close to unity for any reasonable NuMI experimental setup. Equivalent expressions for $P(\nu_\mu \to \nu_e)$ can be found in [11].

3.5. Ambiguity Resolution

The effects of matter can easily be included in our expression for $P(\nu_\mu \to \nu_e)$ by replacing $\sin^n\Delta_{21}$ and $\sin^n\Delta_{31}$ for all n in all three terms using

$$\sin\Delta_{ij} \to \frac{\Delta_{ij}}{(\Delta_{ij} \mp aL)}\sin(\Delta_{ij} \mp aL) \quad (17)$$

where

$$a = \frac{G_F N_e}{\sqrt{2}} \approx (3700\ \text{km})^{-1}\left(\frac{\rho}{2.8\ \text{g cm}^{-3}}\right) \quad (18)$$

The minus (plus) sign is for neutrinos (anti-neutrinos). The factors $\sin\Delta_{32}$ and $\cos\Delta_{32}$ remain unchanged by matter effects. This algorithm comes from the invariance of the product $\Delta m^2_{ij}\sin 2\theta_{ij}$ evaluated in matter and in vacuum.

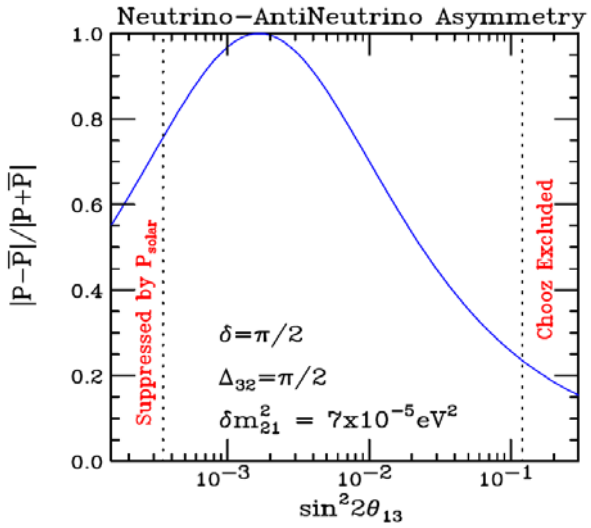

Fig. 3.2: The vacuum asymmetry $|P(\nu_\mu \to \nu_e) - P(\bar\nu_\mu \to \bar\nu_e)|/|P(\nu_\mu \to \nu_e) + P(\bar\nu_\mu \to \bar\nu_e)|$ versus $\sin^2 2\theta_{13}$ at oscillation maximum, Δ_{32} assuming that the CP violation is maximal, δ = π/2. At the peak of this asymmetry the amplitudes for $\nu_\mu \to \nu_e$ from the atmospheric and solar Δm^2's are equal in magnitude. Above (below) the peak the atmospheric (solar) amplitude dominates.

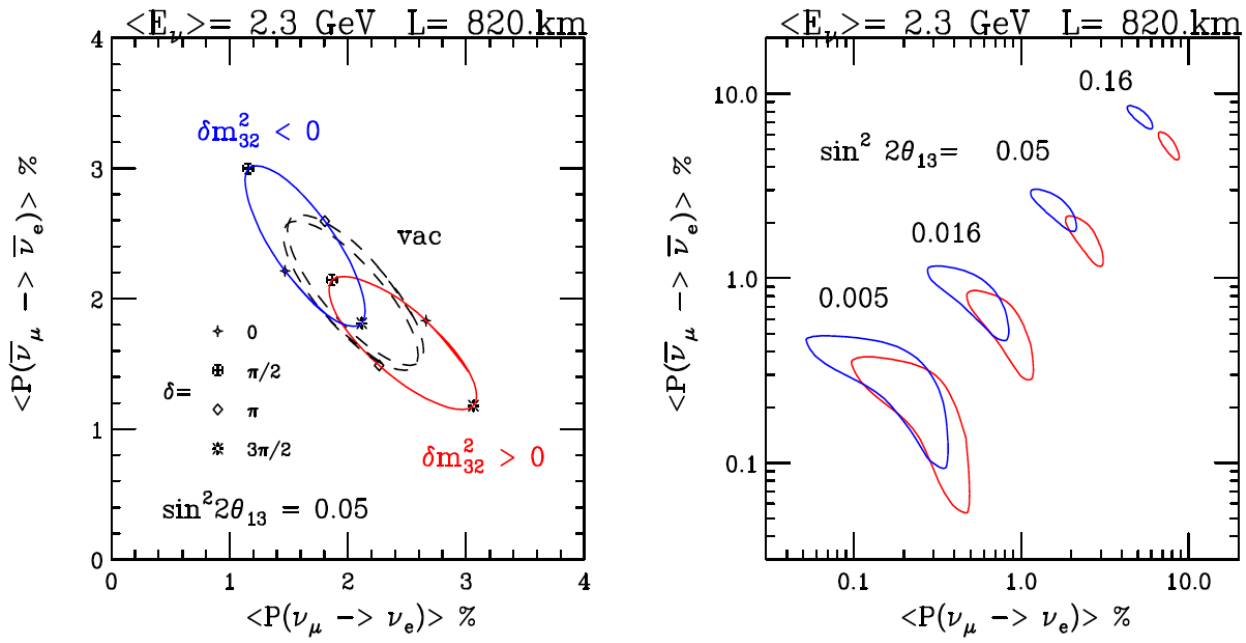

Fig. 3.3: The bi-probability plots $P\left(\nu_\mu \to \nu_e\right)$ versus $P\left(\bar{\nu}_\mu \to \bar{\nu}_e\right)$, assuming a constant matter density of ρ = 2.8 ~g. cm^{-3} at a distance of 820 km and an average energy of 2.3 GeV with a 20% Gaussian spread. The mixing parameters are fixed to be $\left|\Delta m^2_{31}\right| = 2.5\times10^{-3}$ eV^2, $\sin^2 2\theta_{23} = 1.0$, $\Delta m^2_{21} = +7\times10^{-5}$ eV^2, $\sin^2 2\theta_{12} = 0.8$ with the labeled values of $\sin^2 2\theta_{13}$ and δ.

A useful and instructive way to present the combined effects of matter and sub-leading terms is in the bi-probability plots of $P\left(\nu_\mu \to \nu_e\right)$ versus $P\left(\bar{\nu}_\mu \to \bar{\nu}_e\right)$, invented by Minakata and Nunokawa [13]. Fig. 3.3 shows an example of such a plot for a NuMI case.

At the larger values of $\sin^2 2\theta_{13}$, the ellipses associated with the two possible mass hierarchies separate in matter, whereas they are approximately degenerate in vacuum. There is also a significant sensitivity to the CP violating phase, δ. It is the sensitivity to the sign of Δm^2_{32} and the CP violating phase in these plots which allows for the determination of these parameters in a sufficiently accurate experiment. For a single experiment there can be a degeneracy in the determined parameters but this degeneracy can be broken by further experimentation.

In particular the normal and inverted hierarchies may also be able to be distinguished by a comparison of the probability of $\nu_\mu \to \nu_e$ between two different experiments at different baselines, e.g. NuMI and JPARC [12]. If both experiments operated at the first oscillation and both run neutrinos then

$$P^N_{mat}\left(\nu_\mu \to \nu_e\right) \cong \left(1 \pm 2\frac{E^N - E^J}{E_R}\right) P^J_{mat}\left(\nu_\mu \to \nu_e\right) \quad (19)$$

where (P^N, E^N) and (P^J, E^J) are the neutrino transition probabilities and energies for NuMI and JPARC respectively. E_R is the matter resonance energy associated with the atmospheric Δm^2, about 12 GeV, given by eqn. 7. The plus sign is for the normal hierarchy and the minus sign for the inverted hierarchy. For anti-neutrinos these signs are reversed. If either experiment is significantly away from oscillation maximum, the relationship between the two probabilities is more complicated, see [14].

3.6. Other NOνA Measurements

A high precision measurement of $\nu_\mu \to \nu_\mu$ can be used to determine the atmospheric Δm^2 to the 10^{-4} eV^2 level. Also $\sin^2 2\theta_{23}$ will be determined to 2%. Such a measurement can determine how much θ_{23} differs from maximal mixing, *i.e.,* π/4. This difference is a measure of the breaking of a $\nu_\mu \to \nu_\tau$ symmetry at some high energy scale. Since matter effects are suppressed in the channel

$\nu_\mu \to \nu_\mu$ compared to $\nu_\mu \to \nu_e$, a comparison of $\nu_\mu \to \nu_\mu$ to $\overline{\nu}_\mu \to \overline{\nu}_\mu$ is a sensitive test of CPT in the neutrino sector.

3.7. Neutrino Oscillations in 2010

While we have discussed the current status of neutrino oscillations, NOνA will not likely acquire data for a number of years. Thus, although speculative, it is likely worthwhile to attempt to predict the state of knowledge in 5 to 7 years time. There is considerable ongoing activity with respect to solar neutrino oscillations. Thus, by 2010, it is reasonable to expect that the solar Δm^2 and sin $2\theta_{12}$ will be known well enough that they will not be a major source of uncertainty in the interpretation of NOνA results. We also presume that MINOS will have made a 10% measurement of Δm^2_{32}. The JPARC to SuperKamiokande experiment has been delayed to 2008, so it may have only preliminary results by 2010. There has been considerable recent discussion of new reactor-based neutrino oscillation experiments, but the technical and regulatory difficulties of working near a nuclear power plant make prediction of a timescale for those experiments quite uncertain.

3.8. Summary

The important measurements that could be made by NOνA are

• Observation of $\nu_\mu \to \nu_e$ at an L/E in the range of 10^2 to 10^3 km/GeV, which would determine the ν_e role in atmospheric neutrino flavor transitions. In the neutrino oscillation scenario this is a measure of $\sin^2 2\theta_{13}$.

• Matter effects can be used to distinguish the two mass hierarchies and therefore determine the sign of Δm^2_{32}.

• For the Large Mixing Angle solution to the solar neutrino puzzle there is sensitivity to the CP violating phase in the channel $\nu_\mu \to \nu_e$.

• Precision measurements in $\nu_\mu \to \nu_\mu$ channel can measure how close θ_{23} is to $\pi/4$, that is maximal mixing. A comparison of $\nu_\mu \to \nu_\mu$ to $\overline{\nu}_\mu \to \overline{\nu}_\mu$ is a sensitive test of CPT violation since matter effects are suppressed in this channel.

Thus, there is a very rich neutrino physics program to be explored in a ν_e appearance experiment using the NuMI beam. Details of experimental and beam possibilities will be explored in subsequent chapters.

Chapter 3 References

[1] Kamiokande Collaboration, Y. Fukuda *et al.*, Phys. Lett. B **335** (1994) 237.
Super-Kamiokande Collaboration, Y. Fukuda *et al.*, Phys. Rev. Lett. **81** (1998) 1562; S. Fukuda *et al.*, *ibid.* **85** (2000) 3999.
[2] K2K Collaboration, M. H. Ahn *et al.*, Phys. Lett. B **511** (2001) 178; Phys. Rev. Lett. **90**, 041801 (2003).
[3] Soudan 2 Collaboration, M. Sanchez *et al.*, Phys. Rev. D **68**, 113004 (2003).
[4] CHOOZ collaboration, M. Apollonio *et al.*, Phys. Lett. B **466** 415.
[5] SNO Collaboration, Q. R. Ahmad *et al.*, Phys. Rev. Lett. **87** (2001) 071301;
S. N. Ahmed *et al.*
[6] S. Fukuda *et al.* [Super-Kamiokande Collaboration], Phys. Lett. B **539**, 179 (2002).
[7] K. Eguchi *et al.* [KamLAND Collaboration], Phys. Rev. Lett. **90**, 021802 (2003).
[8] A. Aguilar *et al.* [LSND Collaboration], Phys. Rev. D **64**, 112007 (2001).
[9] E. Church *et al.* [BooNe Collaboration], FNAL-PROPOSAL-0898.
[10] E. Ables *et al.* [MINOS Collaboration], FERMILAB-PROPOSAL-0875.
[11] V. D. Barger, S. Geer, R. Raja and K. Whisnant, Phys. Rev. D **63**, 113011 (2001), I. Mocioiu and R. Shrock, JHEP **0111**, 050 (2001).
[12] H. Minakata and H. Nunokawa, JHEP **0110** (2001) 001 [hep-ph/0108085].
[13] Y. Itow *et al.*, [The JHF-Kamioka neutrino project], arXiv:hep-ex/0106019.
[14] H. Minakata, H. Nunokawa and S. Parke, Phys. Rev. D **68**, 013010 (2003).

4. Experiment Overview

4.1. NuMI Beam

The NuMI neutrino beam is currently under construction at Fermilab [1]. The beamline begins with 120 GeV protons extracted from the Main Injector accelerator, which are transported downward at a 15.8% slope to the NuMI Target Hall. Before striking the production target the beam is bent upward to a 5.8% downward slope, so that it is aimed at the MINOS far detector in Minnesota. Two parabolic magnetic horns, each about 3 m long and pulsed at 200 kA, focus secondary pions and kaons emitted from the target. The secondary beam subsequently travels with the same downward slope of 5.8% through an evacuated decay pipe, which is 675 m in length and 2 m in diameter. The decay pipe ends in the Hadron Absorber Hall where residual protons and non-decayed secondary mesons are absorbed in the Al-Fe water-cooled beam stop. The muons resulting from pion and kaon decays are absorbed in 240 m of earth shielding, which separates the Absorber Hall from the Near Detector Hall. Three muon alcoves, located within this shielding downstream of the Absorber Hall, contain muon detectors to monitor the beam intensity and shape on a pulse-to-pulse basis. Fig 4.1 shows the plan and elevation views of the NuMI beamline.

A unique feature of the NuMI neutrino beam is the ability to change the focusing optics configuration and hence the neutrino energy band accepted. Specifically, one can change the relative positions of the target and the first horn and the separation between two horns. These configurations are illustrated in Fig. 4.2, together with the spectra for three possible beam element arrangements, referred to as low, medium, or high energy beam tunes. While the movement of the second horn is logistically complex and requires several weeks downtime, the target position can be varied remotely. Accordingly, one also has a method of readily changing the energy spectrum in a continuous fashion by moving just the target at a small sacrifice of the neutrino flux as compared to a fully optimized configuration [2].

Full optimization for a given energy also involves adjusting the target length. The initial beam for the MINOS experiment is the low energy tune, with the front end of the target located 0.34 m upstream of the first horn and a horn separation of 7 m. The target is 0.95 m long and is composed of 47 graphite sections, each 20 mm in length, with 0.3 mm air gaps between sections.

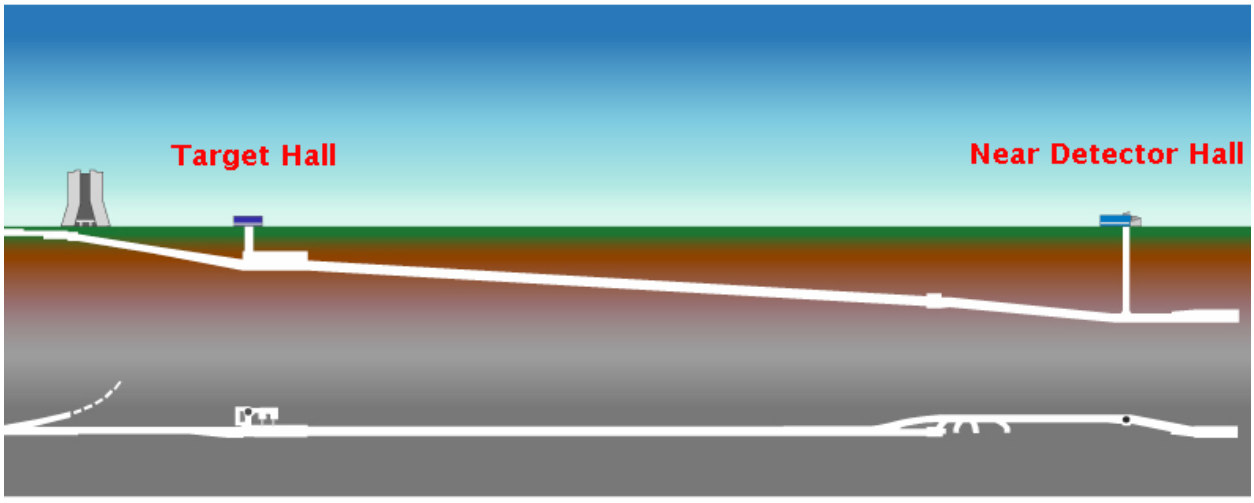

Fig. 4.1: Plan (bottom) and elevation (top) views of the NuMI beam line.

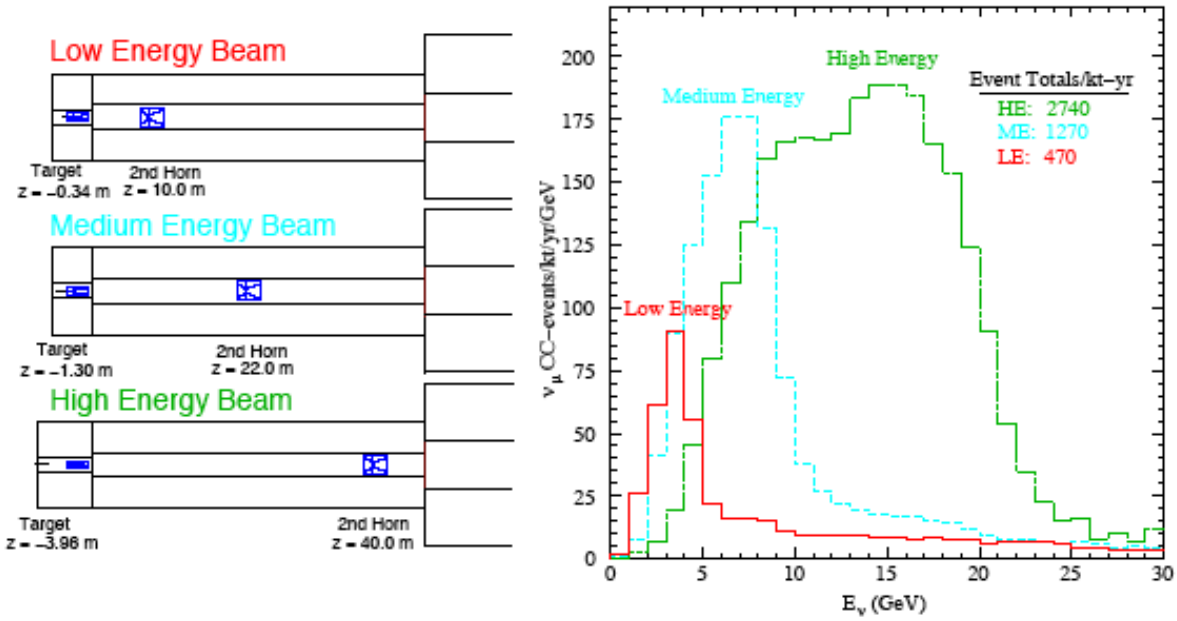

Fig. 4.2: Left: The locations of the target and second horn for the three NuMI beam configurations. Right: The expected neutrino interaction rates at the MINOS far detector site for each of the three beam tunes assuming 3.7 x 10^{20} protons on target per year.

The NuMI beam has been designed for a proton intensity of 4 x 10^{13} protons per pulse every 1.9 sec—roughly 0.4 MW of beam power. Based on previous operating experience of the proton source, this per pulse intensity should produce 3.7 x 10^{20} protons per year. It appears quite likely that the beam line itself, with minor modifications, could accept higher proton intensity.

The outfitting of the NuMI beam tunnels and the associated buildings was completed in October 2003 and installation in the Target Hall has started. Beneficial occupancy of the Near Detector Hall occurred on 10 March 2004 and the first beam on target is expected in early 2005.

4.2. Off-Axis Concept

Pions and kaons decay isotropically in their centers of mass resulting in a relatively broad neutrino beam energy spectrum. For small angles, the flux and energy of neutrinos produced from the decay $\pi \rightarrow \mu + \nu$ in flight and intercepted by a detector of area A and located at distance z are given in the lab frame by:

$$F = \left(\frac{2\gamma}{1+\gamma^2\theta^2} \right)^2 \frac{A}{4\pi z^2} \qquad (1)$$

$$E_\nu = \frac{0.43 E_\pi}{1+\gamma^2\theta^2}, \qquad (2)$$

where θ is the angle between the pion direction and the neutrino direction, E_π the energy of the parent pion, m_π the mass of the pion and $\gamma = E_\pi/m_\pi$. The expressions for the neutrinos from the corresponding charged K decays are identical except that 0.43 is replaced by 0.96 resulting in a more energetic and broader distribution for identical meson energies. The neutrino flux peaks in the forward direction for all meson energies, which is the reason that, in general, neutrino detectors are placed on axis. Furthermore, in the forward direction there is a linear relationship between neutrino and meson energies. As the neutrino direction deviates from the meson direction, however, the relationship between the pion energy and neutrino energy flattens. At some angles, a wide energy band of pions contributes to roughly the same energy neutrinos. Fig. 4.3 illustrates both features.

The angle-energy relationship illustrated in Fig. 4.3 can be utilized to construct a nearly monoenergetic neutrino beam by viewing the NuMI beam with a detector at a location off the beam axis. This concept was first proposed for the experiment E-889 at the Brookhaven National

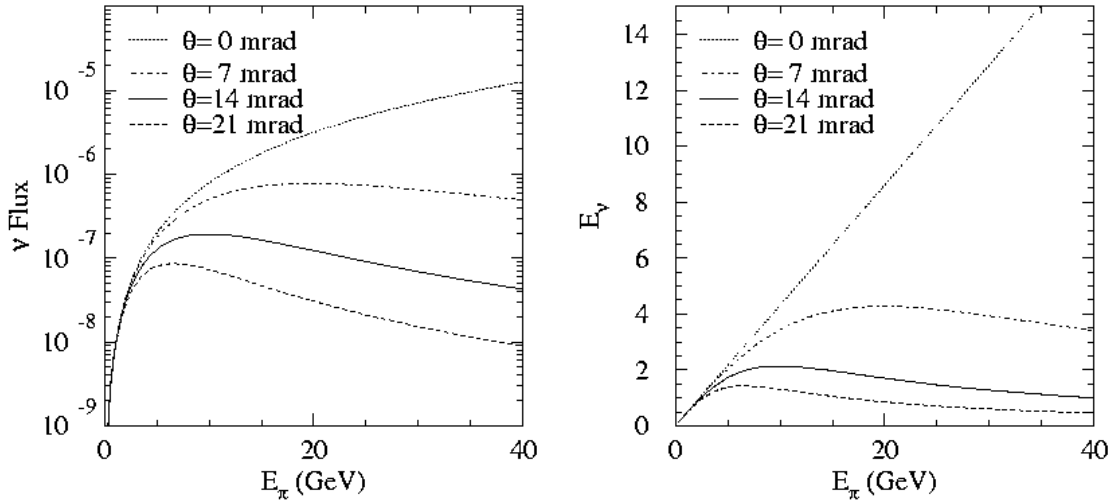

Fig. 4.3: Left: The neutrino flux from a pion of energy E_π as viewed from a site located at an angle θ from the beam axis. The flux has been normalized to a distance of 800 km. Right: The energy of the neutrinos produced at an angle θ relative to the pion direction as a function of the pion energy.

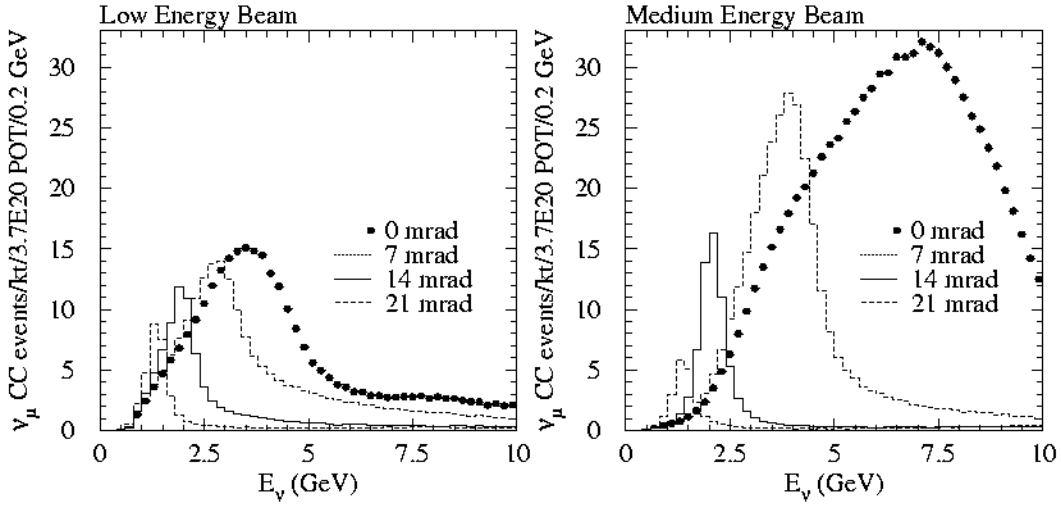

Fig. 4.4: CC ν_μ event rates expected under a no-oscillation hypothesis at a distance of 800 km from Fermilab and at various transverse locations for the NuMI low-energy beam configuration (left) and medium-energy beam configuration (right).

Laboratory [3]. Fig. 4.4 shows the implementation of this scheme at locations of 5, 10, and 20 km (corresponding to the angles of 7, 14, and 21 mr) off the NuMI beam axis at a distance of 800 km from the target.

The off-axis configuration has several important advantages for a $\nu_\mu \rightarrow \nu_e$ oscillation experiment. Among the most important ones are:

• The central energy of the beam can be tuned to the desired energy by selecting an appropriate angle with respect to the beam axis for the location of the detector.

• The spectrum in the peak is quite narrow which helps to reduce the backgrounds, which tend to have much broader energy distributions.

• The high energy tail is considerably reduced with respect to the on-axis beam, which reduces the NC and τ backgrounds

These features are quite apparent from Figs. 4.3 and 4.4.

Finally, we would like to make several additional observations about the properties of the off-axis configuration:

• The energy of the beam is determined primarily by the transverse location of the detector. The dependence on the focusing optics is relatively mild.

• The focusing optics configuration affects primarily the intensity of the beam.

• The main peak is composed almost exclusively of the neutrinos from pion decay; K decays give neutrinos at significantly wider angles. Thus, prediction of the spectrum is very insensitive to knowledge of the K/π production ratio.

For the current range of Δm_{13}^2 values and the three nominal NuMI beam configurations, the medium energy one gives the optimum spectrum for the $\nu_\mu \rightarrow \nu_e$ oscillation experiment. Additional fine tuning of the optics as well of the target geometry around the medium energy configuration should yield some additional optimization.

4.3. Detector Design Considerations

4.3.1. General Goals: The challenge for next generation neutrino experiments is to observe $\nu_\mu \rightarrow \nu_e$ oscillations in the atmospheric neutrino mass squared range down to the level of few parts per thousand. The CHOOZ experiment gives a limit on ν_e disappearance probability in that experiment of about 0.1 – 0.2 [4], the exact limit depending on the value of Δm_{23}^2. This translates into a limit on ν_e appearance probability of 0.05 – 0.1. MINOS is expected to improve this by a factor of 2-3. There are no clear reliable theoretical guidelines as to the most likely value of this parameter.

Charged current ν_e interactions can be identified by the presence of an electron in the final state. The experimental backgrounds to the $\nu_\mu \rightarrow \nu_e$ oscillation signals arise from two general sources. There are genuine events with electrons resulting from the intrinsic ν_e component in the beam and from τ decays produced in the charged current ν_τ interactions from $\nu_\mu \rightarrow \nu_\tau$ oscillations. The latter background is very small for NOνA since most of the ν_μ flux is below τ production threshold. In addition there are potentially misidentified NC events or high y ν_μ CC events where one or more π^0's in the final state masquerades as an electron or, less likely, that a hadron is misidentified as an electron.

The intrinsic ν_e's in the beam come from μ decays and Ke_3 decays (charged and neutral). They are of the order of 0.5-1.0% of ν_μ's, but can be reduced further by an appropriate energy cut. *K*e_3 contamination is typically of the order of 1/5 of the μ decay background in NOνA.

The experimental challenge has two parts:

• reducing these two backgrounds as much as possible (discussed below)

• measuring these backgrounds well enough that the principal ultimate uncertainty comes from the statistical fluctuations in the event sample of interest (discussed in Chapter 9).

4.3.2. Design Optimization Issues: The background from ν_e's can only be reduced by good energy resolution since the ν_e's from background sources have a broader energy spectrum than the potential signal, whose width is determined by the spectrum of ν_μ's convoluted with the oscillation probability (see Fig. 4.5). The NC and CC backgrounds can be reduced by a well-designed detector. The challenge is to suppress them to levels comparable or lower than the intrinsic ν_e background level with minimum impact on the signal detection efficiency.

The need to separate out the electromagnetic component in a hadronic jet from the remaining hadrons is common to many high energy experiments. In the calorimetric method, this is generally achieved by having a high Z electromagnetic calorimeter in front of the hadron section. Clearly that technique is not suitable for electron/π^0 separation. The latter has been traditionally done in open geometry experiments by using a Cherenkov counter. In the recent neutrino experiments: IMB, Kamiokande and SuperKamiokande, this general method was implemented by water Cherenkov detectors. The other technology of choice in those experiments (*e.g.* CHARM II and the BNL oscillation experiment) has been use of low Z calorimeters, which facilitate identification of the electron by tracking.

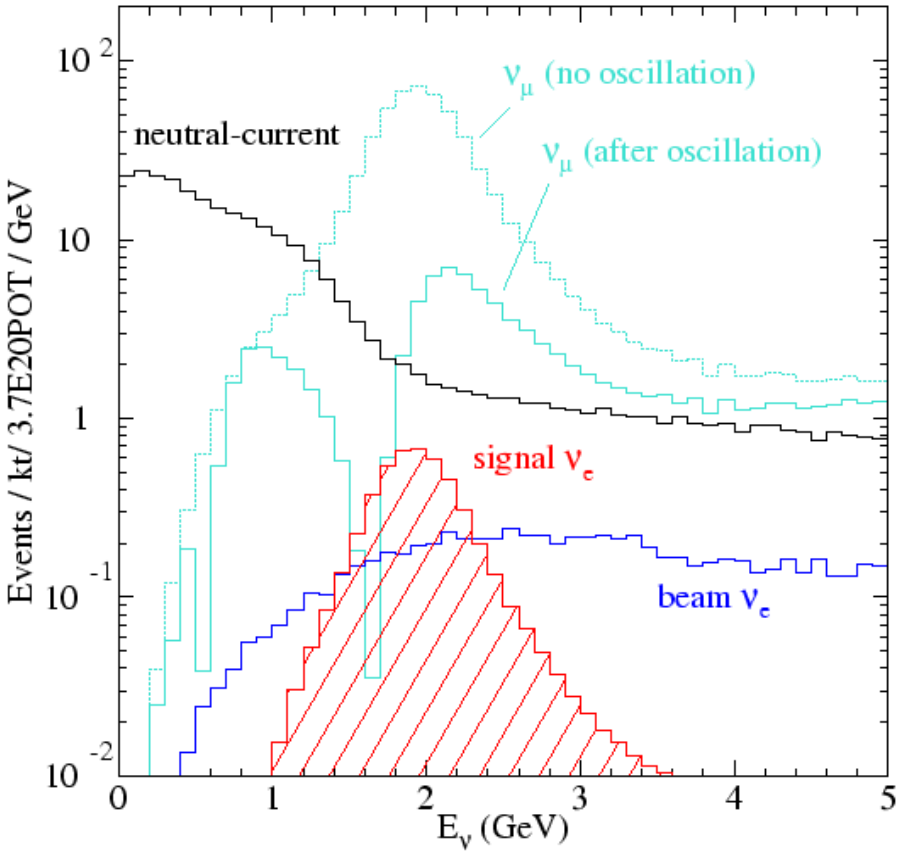

Fig. 4.5: Simulated energy distributions for the ν_e oscillation signal, intrinsic beam ν_e events, NC events and ν_μ CC events with and without oscillations. The simulation used $\Delta m_{23}^2 = 2.5 \times 10^{-3}$ eV^2, $\sin^2(2\theta_{23}) = 1.0$ and $|U_{e3}|^2 = 0.01$. An off-axis distance of 12 km at 810 km was assumed.

4.3.3. Tracking calorimeter design issues: In principle, at least, a highly segmented detector can separate electrons from π^0's by utilizing several experimental characteristics:

- finite separation between the vertex and conversion points of the γ's from the π^0 ,
- two electromagnetic showers (for π^0) *vs* one (for electrons),
- double pulse height right after a γ conversion.

Success of the separation based on these characteristics requires fine segmentation: longitudinally, smaller than a radiation length, X_0; transversely, finer than the typical spatial separation of the two gammas from the π^0 decay. The transverse segmentation also has to be such that individual tracks in the final state can be separated from each other.

Besides the need to distinguish electrons from π^0's, one must also distinguish electrons from hadrons and muons. This is harder in a low Z material and relies on absence of hadronic interactions for electrons and a generally broader pattern of hits along the track for electrons due to the electron shower.

The other important characteristic of a good ν_e detector for $\nu_\mu \rightarrow \nu_e$ oscillations is its energy resolution. One can reduce the intrinsic beam ν_e background utilizing the fact that the events from $\nu_\mu \rightarrow \nu_e$ oscillations will have a sharp energy spectrum at a predictable energy in contrast to the backgrounds that will exhibit a much broader spectrum. This is an important feature of an off-axis experiment, where the detector sees neutrinos in a narrow energy band. Electron-type neutrinos from μ decays will be in roughly the same energy range as the oscillated ν_e's but have a much broader distribution. Ke_3 decays will give higher energy neutrinos covering a broad energy range whereas the τ decay electrons will peak towards low energies. The shape and the level of

backgrounds as well of a possible signal are shown in Fig. 4.5.

4.4. Far Detector

The NOνA Far Detector will be located in a new surface laboratory approximately 810 km from Fermilab and displaced approximately 10 km from the central axis of the NuMI beam. The baseline design for the detector is a low density, low Z, 50,000 metric ton, tracking calorimeter, comprised of 42,000 tons of wood particle board as a passive absorber, 6,900 tons of mineral-oil based liquid scintillator as an active detector and 1,800 tons of polyvinyl chloride (PVC) loaded with 10-15% titanium dioxide extrusions to contain the liquid scintillator.

The liquid scintillator and the passive absorber will be arranged in 750 planes, oriented normal to the axis pointing towards Fermilab. Each plane will be 29.3 m wide by 14.6 m high by 0.229 m thick. The entire detector will therefore extend for a total length of 750 times 0.229 m or 171.5 m along the axis pointing to Fermilab. The liquid will be contained in the PVC extrusions, which will be 1.22 m by 0.029 m by 14.6 m long. Each extrusion will be divided into 30 cells, each cell having a cross-section of 3.96 cm by 2.56 cm, with a total length of 14.6 m. The scintillation light in each cell will be collected by a looped 0.8 mm diameter wavelength-shifting plastic fiber. Light from both ends of the fiber will be directed to a single pixel on an avalanche photodiode (APD). APDs are low cost photodetectors providing high quantum efficiency. Their main difficulties are low amplification and electronic noise. High gain preamplifiers, such as those developed for the LHC CMS detector, can provide the necessary signal output levels. Noise will be reduced to a feasible level by use of Peltier-effect coolers to reduce the operating temperature of the APDs to -15 C.

As described in Chapter 6, the liquid scintillator technology has been selected over several options that have received considerable study during the previous year for reasons of both better event reconstruction and lower cost. The designs that were not selected remain as alternatives, in case of unforeseen difficulties in implementing the baseline design on the required scale. These backups include plastic scintillator as the active detector medium, resistive plate chambers (RPCs) as the active detector and multichannel photomultipliers (PMTs) as high-gain photodetectors.

Chapter 7 describes the NOνA Far Detector in considerable detail and Chapters 5 and 8 discuss its physics capabilities. The Appendix includes information about the alternative RPC detector technology.

4.5. Backgrounds and the Near Detector

The purpose of the NOνA Near Detector is to increase the sensitivity of our search for $\nu_\mu \rightarrow \nu_e$ appearance by improving our knowledge of backgrounds, detector response and the off-axis neutrino beam energy spectrum. The 120-ton near detector would be located about 12 m off the NuMI beam axis, in the access tunnel upstream of the MINOS Near Detector Hall. This site provides a neutrino-beam energy spectrum that is quite similar to that at the far-detector.

Although a primary design requirement is that the near detector be as similar as possible to the far detector, of necessity it will have smaller transverse and longitudinal dimensions and its readout electronics must be able to cope with the high event rates during the 10 microsecond beam spill. We plan to measure the effects of such differences between the near and far detectors in a separate program of test beam measurements.

Chapter 8 describes the simulation and analysis of beam-related backgrounds. The near-detector determination of these backgrounds is described in Chapter 9, along with the test beam program to calibrate detector response. NOνA will also make use of information from the MIPP, MINERνA and MINOS experiments to improve knowledge of the neutrino-beam spectrum and ν_e component.

The beam-related backgrounds to our $\nu_\mu \rightarrow \nu_e$ oscillation search fall into three categories: intrinsic ν_e contamination in the beam, neutral current events, and charged current ν_μ interactions where the outgoing muon is not identified. The levels of the three backgrounds are different at near and far detectors because the beam spectra and compositions are different at the two locations (primarily because of oscillations). The NOνA near detector, along with information about the neutrino beam from the MIPP, MINERνA and MINOS experiments, will

measure these backgrounds and provide information to predict accurately the magnitude of each at the far detector.

We plan to conduct the NOνA test-beam program in two phases. During the first two years a number of small prototype detectors, instrumented with prototype near and far detector electronics, would be used to verify predicted responses. The second stage of the program would make use of larger "calibration detectors," small-scale versions of the near and far detectors, to determine absolute and relative energy calibrations. These data will also be used to tune Monte Carlo simulations and to develop particle identification algorithms. We hope to perform these measurements at a Fermilab test-beam facility.

4.6. Cosmic Ray Background

The atmosphere behaves as a 10-interaction length, 25-radiation length calorimeter for the incident primary cosmic rays. The results of interactions in the atmosphere are extensive air showers, some of whose components persist to the surface: penetrating muons with ~4 GeV average energy, showering electrons and photons with average energies in the range of tens of MeV, and some hadrons (primarily neutrons) with hundreds of MeV. Backgrounds from cosmic rays are substantially suppressed by the fast beam spill of the Main Injector, resulting in a detector live-time of only 100 seconds per year (10^7 spills per year, each 10 μs long). These backgrounds are also reduced by the orthogonality between the horizontal neutrino beam direction and the vertical cosmic ray flux.

In Chapter 10, we show that the detector can easily accommodate the flux of through-passing muons. In addition, we discuss the possibility of further background suppression from a 2-3 m overburden above the detector and also an active shield. We also emphasize that it will be important to measure a large number of cosmic ray induced interactions in the detector during the relatively long intervals between beam spills.

Chapter 10 also discusses the small component of hadrons that survives to ground level. Neutrons are the most significant; they have an interaction length of ~1.5 m in the absorber material and their interactions are therefore a potential source of background. We estimate that 1.0×10^5 neutrons with energies above 2 GeV will interact in the detector per year within the neutrino spill gate; they will be concentrated near the top of the detector.

We conclude in Chapter 10 that the neutron background will not prejudice the quality of our measurements. Although we presently believe that an overburden on the experiment is not needed, we think it is prudent to measure the neutron background with a prototype detector during the coming year.

In addition, the installation of an active shield around the upper portions of the detector appears prudent. Such a shield is significantly less expensive than the support structure required for passive shielding of sufficient thickness to have a significant effect.

4.7. NOνA Detector R&D Program

The conceptual designs of the NOνA Near and Far Detectors described in this proposal require a dedicated R&D program as the next step toward actual construction of the experiment. The goals of the R&D program will be to improve detector performance, optimize and validate choices of critical materials and components, perform engineering studies leading to more accurate cost estimates and, ultimately, to minimize costs. We plan to complete this R&D program over the next two years, culminating in the production of the NOνA Technical Design Report, Fermilab Stage 2 approval and a DOE Project Baseline review.

The last section of Chapter 7 describes the detector technology R&D topics we plan to investigate, including the overall design of the Far Detector and its electronics. This section describes a number of R&D studies that are common to the Near and Far Detectors, as well as some topics that are specific to the Far Detector. The final section of Chapter 9 describes the program of test beam measurements we plan to use to evaluate the performance of prototype detectors and, ultimately, to calibrate the energy responses of the NOνA Near and Far Detectors. The last section of Chapter 10 describes the measurements we plan to make to check the validity of our preliminary conclusion that an overburden is unnecessary to reduce cosmic-ray backgrounds in the far detector. Chapter 11 concludes with a list of engineering topics that need to be investigated to

optimize the design of the Far Detector building, support structure and infrastructure. The final section of the Appendix describes the RPC R&D program, which is focused on reducing the cost of this alternative detector technology for NOνA. Promising areas of study include separate optimization of the detector structure for modular (using commercial shipping containers) and monolithic architectures, investigation of double-gap RPCs, and simplified high-voltage and gas systems.

4.8 Collaboration Organization

At our February 7-8, 2004 collaboration meeting, we took the first steps toward providing governance for the collaboration. Peter Litchfield (Minnesota) was elected temporary Institutional Board chair and John Cooper (Fermilab) and Gary Feldman (Harvard) were elected temporary co-spokespersons. A temporary Executive Council was elected composed of the above officers plus Carl Bromberg (Michigan State), Ken Heller (Minnesota), Mark Messier (Indiana), Doug Michael (Caltech), Ron Ray (Fermilab), Alfons Weber (RAL and Oxford), and Stan Wojcicki (Stanford). These officers will serve approximately six months until the collaboration's August meeting. In the meantime, the Executive Council will appoint a Constitution Committee to draft collaboration bylaws. It is expected that this Committee will report to the August meeting, that a set of bylaws will be adopted at this meeting, and that a new set of officers will be elected in accordance with these bylaws.

Chapter 4 References

[1] The Fermilab NuMI Group, "NuMI Facility Technical Design Report," October 1998, Fermilab Report NuMI-346.
[2] M. Kostin *et al*., "Proposal for a continuously-variable beam energy," October 2001, Fermilab Report NuMI-783.
[3] The E889 Collaboration, "Long Baseline Neutrino Oscillation Experiment at the AGS," Brookhaven National Laboratory Report BNL No. 52459, April 1995.
[4] CHOOZ collaboration, M. Appollonio *et al*., Phys. Lett. B **466** 415.

5. Physics Potential of NOνA

5.1. Introduction

Assuming that sterile neutrinos either do not exist or do not mix with active neutrinos, there are currently three parameters of neutrino oscillations about which we have no information or only upper limits: $\sin^2(2\theta_{13})$, the sign of Δm_{31}^2 (i.e., whether the solar oscillation doublet has a higher or lower mass than the third state which mixes in the atmospheric oscillations), and the CP-violating phase δ. All three of these parameters significantly affect the rate of $\nu_\mu \rightarrow \nu_e$ oscillations at the atmospheric oscillation length. Thus, a single measurement, for example, an off-axis neutrino run at the first oscillation maximum, will be consistent with more than one set of values for these parameters. An additional measurement, for example an antineutrino run, may or may not be able to resolve all three parameters (in principle). This is illustrated in Fig. 5.1, which shows all of the values of the parameters consistent with a 2% $\nu_\mu \rightarrow \nu_e$ oscillation probability 10 km off-axis at an 820 km baseline. The values of $\sin^2(2\theta_{13})$, are shown on the vertical axis. The solid line represents the normal mass hierarchy (solar doublet low) and the dashed line represents the inverted hierarchy. The values of δ vary around the ellipses as indicated. The horizontal axis shows what the result of an antineutrino run would be.[1] As an example, a sufficiently accurate measurement of a 4% antineutrino oscillation probability would resolve all three parameters with a two-fold ambiguity in δ. However, a measurement of a 2% antineutrino oscillation probability would not be able to resolve the mass hierarchy, regardless of its precision; a third measurement would be required.

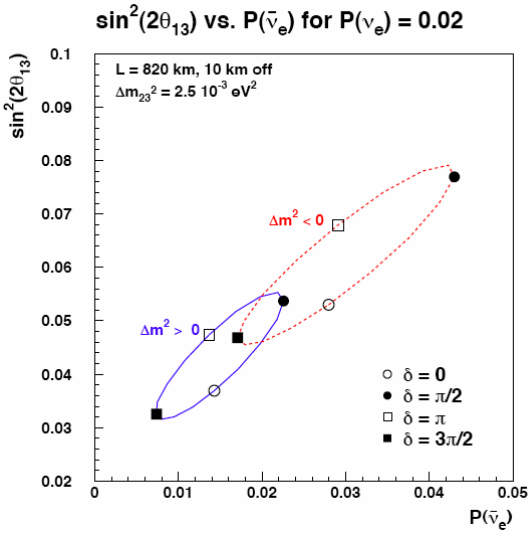

Fig. 5.1: Plot of the possible results of a measurement of a 2% oscillation probability. See text for explanation.

5.2. Primary NOνA Goal

The primary goals of the off-axis program will change with time. The first goal will be to measure $\nu_\mu \rightarrow \nu_e$ oscillations with a sensitivity approximately an order of magnitude greater than that of the MINOS experiment.[2] Figure 5.2 shows the calculated three standard deviation discovery limits for $\nu_\mu \rightarrow \nu_e$ oscillations in terms of the three unknown parameters, assuming $\Delta m_{32}^2 = 0.0025$ eV^2. The vertical axis represents the fraction of possible δ values for which a 3-σ discovery could be made. In other words, zero represents the limit for the most favorable value

[1] Figure 5.1 does not include any allowance for either measurement uncertainties or uncertainties in the atmospheric oscillation parameters Δm_{32}^2 and $\sin^2(2\theta_{23})$, and to a much lesser extent, the solar oscillation parameters Δm_{21}^2 and $\sin^2(2\theta_{12})$. The following discussion of sensitivities will include the measurement uncertainties, but not the parameter uncertainties. In this regard it should be mentioned that there is a particularly nasty ambiguity associated with $\sin^2(2\theta_{23})$ if it is not equal to unity. This is because $\nu_\mu \rightarrow \nu_e$ oscillations at the atmospheric mass scale are proportional to $\sin^2(\theta_{23})$. For example, if $\sin^2(2\theta_{23}) = 0.95$, then $\sin^2(\theta_{23}) = 0.39$ or 0.61, depending on whether θ_{23} is less than or greater than $\pi/4$.

[2] With a total of 16×10^{20} pot, MINOS expects to achieve an average three-σ sensitivity to $\sin^2(2\theta_{13})$ of 0.085, assuming a normal mass hierarchy and a typical value of δ. [1] The 90% confidence level upper limit from the CHOOZ experiment at $\Delta m_{32}^2 = 0.0025$ eV^2 is 0.14. [2]

of δ for a given $\sin^2(2\theta_{13})$, one represents the least favorable value of δ, and 0.5 represents a typical value. The lines represent the two possible values of the sign of Δm_{31}^2 and different assumptions on the number of protons on target (pot) that the experiment might see in a five year run. (If the figure is being viewed in gray scale, the line to the right for each number of protons represents the inverted mass hierarchy.) 20×10^{20} pot represents our estimate of what Fermilab might be able to deliver in a five-year run with incremental Booster and Main Injector improvements, while 100×10^{20} pot represents the expectation with the Booster replaced by a new Proton Driver. The three standard deviation sensitivity of the T2K (JPARC Phase 1) proposal [3] is also shown.

This and other calculations in this chapter are based on the baseline detector simulations discussed in Chapter 8.[3] A 5% systematic error on the background determination has been included in this and the other calculations presented in this chapter. However, the statistical errors on the backgrounds always dominate.

The off-axis distance chosen for these calculations is 10 km for $\Delta m_{32}^2 = 0.025$ eV^2. Although results are relatively insensitive to the off-axis transverse distance, there are some trade-offs that need to be considered. For a given set of parameters, the matter effects increase with increasing transverse distance, while the number of signal events tends to decrease. For the primary goal of seeing the $\nu_\mu \rightarrow \nu_e$ oscillations, a 10 km transverse distance is 10 to 20% more sensitive than a 12 km distance. For the resolution of the mass hierarchy, they are almost indistinguishable. We plan to delay the choice of a transverse distance as long as possible to be able to use the most reliable knowledge of the physics parameters and the physics questions of interest.

[3] The results presented here are somewhat less sensitive than those presented in the Progress Report submitted to Fermilab in December 2003[4]. This is due to the use of new beam and physics simulations, as well as a more realistic representation of the detector in the simulations. A major factor was the addition of coherent π^0 production in the backgrounds. A warning was included in the Progress Report stating that the calculations reported there were probably optimistic for the reasons given above.

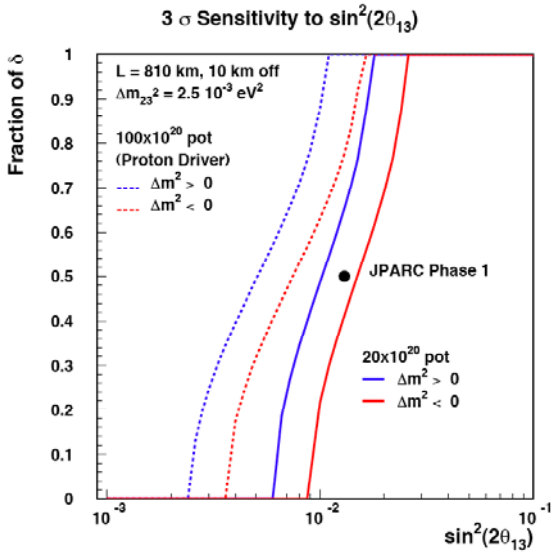

Fig. 5.2: Three standard deviation discovery limits for the observation of $\nu_\mu \rightarrow \nu_e$ oscillations. See text for more details.

5.3. Resolution of the Mass Hierarchy

The issue of the atmospheric mass hierarchy can only be resolved through the observation of matter effects due to the transit of electron-type neutrinos through the earth. As described in Chapter 3, to first order these effects increase linearly with the distance the neutrinos travel through the earth. Since the NuMI beamline provides the longest baseline of currently planned experiments, the resolution of matter effects becomes the primary goal of NOνA once a signal for $\nu_\mu \rightarrow \nu_e$ oscillations is established.

As discussed above, this can be done in some cases with an antineutrino run. Figure 5.3 shows the regions in which a two-standard deviation (i.e., 95% confidence level) resolution of the mass hierarchy is possible with a three-year neutrino run followed by a three-year antineutrino run. The explanations given for Fig. 5.2 apply here as well. The value of a proton driver to extend the reach of the experiment is quite evident.

If nature chooses the parameters such that they cannot be resolved by a single neutrino and a single antineutrino run, then a third measurement will be necessary.

Reactor experiments designed to measure $\sin^2(\theta_{13})$ are generally not useful in this regard. The reason can be seen by examining Fig. 5.1. A

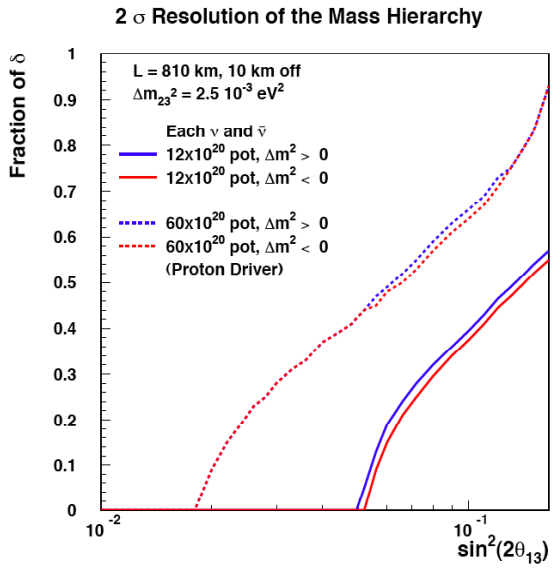

Fig. 5.3: Two standard deviation limits for the resolution of the mass hierarchy with a three-year neutrino and a three-year antineutrino run. See text for more details.

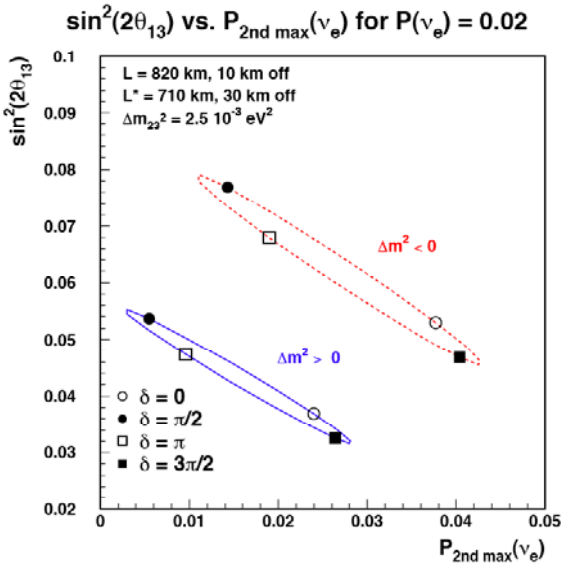

Fig 5.4: Plot of the possible results of a measurement of a 2% neutrino oscillation probability at the first maximum versus the oscillation probability at the second maximum. Compare with Fig. 5.1 to see the how ambiguities there are resolved.

reactor experiment would measure a horizontal band in this plot. Since the ellipses lie along the diagonal, cases for which antineutrino runs do not resolve the mass hierarchy are the same cases in which a reactor experiment does not resolve them. In addition, the θ_{23} ambiguity discussed in Footnote 1 obscures the comparison of the two experiments.

Another possibility for resolving the mass hierarchy is a comparison of NOνA results with T2K (JPARC Phase 1) results [3]. However, the modes in which these two experiments are planning to run combined with their limited statistics does not appreciably increase the parameter space for which the mass hierarchy is resolved.

In general the best way to resolve the mass hierarchy is to run at both the first and second oscillation maxima. The reason is that since the second maximum is at one-third the neutrino energy of the first maximum, matter effects there decrease by a factor of three while CP violating effects increase by a factor of three. (The CP violation comes from an interference term between the atmospheric and solar oscillations; the lower energy increases the solar oscillation part of the interference term.) This is illustrated in the probability plot of Fig. 5.4, which plots the result of a second maximum measurement along the horizontal axis. Points that were ambiguous in Fig. 5.1 are now clearly separated. For example, in Fig. 5.1, the ($\Delta m^2 > 0$, $\delta = \pi/2$) point was close to the ($\Delta m^2 < 0$, $\delta = 3\pi/2$) point. In Fig 5.4, they are separated by approximately an order of magnitude in the neutrino oscillation probability at the second maximum.

In the longer term, one could envision an off-axis measurement at the second maximum in the NuMI beam line. This would involve either moving the detector or building a new detector about 30 km off the center of the beamline, or building a new NuMI beam line to point about 25 mrad away from the present line. Unfortunately, the event rate is proportional to the third power of the energy (two powers from the flux and one from the cross section), so nominally the event rate will be about 27 times smaller. For this reason, the experiment is only possible with the proton intensity increase from a proton driver. Figure 5.5 shows the regions in which a two standard deviation resolution of the mass hierarchy is possible with a three-year neutrino and a three-year antineutrino run into two 50 kT

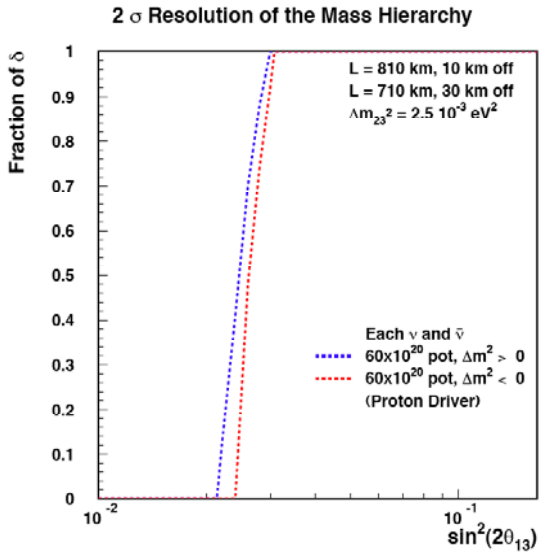

Fig. 5.5: Two standard deviation limits for the resolution of the mass hierarchy with a three-year neutrino and a three-year antineutrino run and two far detectors. See text for more details.

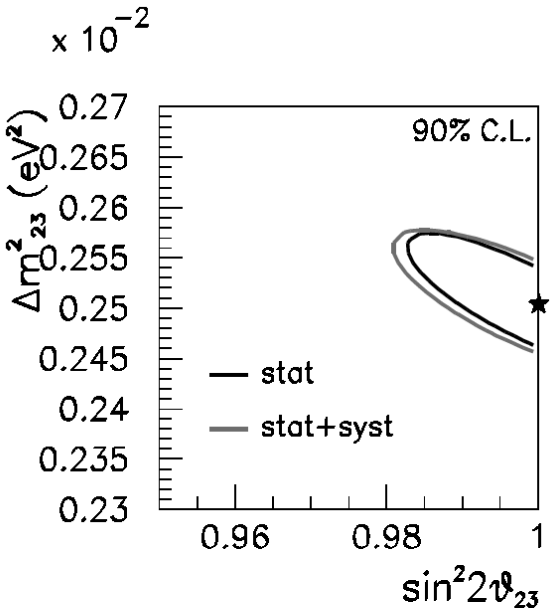

Fig. 5.6: Expected 90% confidence limit allowed region for Δm_{32}^2 and $\sin^2(2\theta_{23})$ for true values shown by the star. The black line represents the results with purely statistical errors; the gray line adds systematic errors.

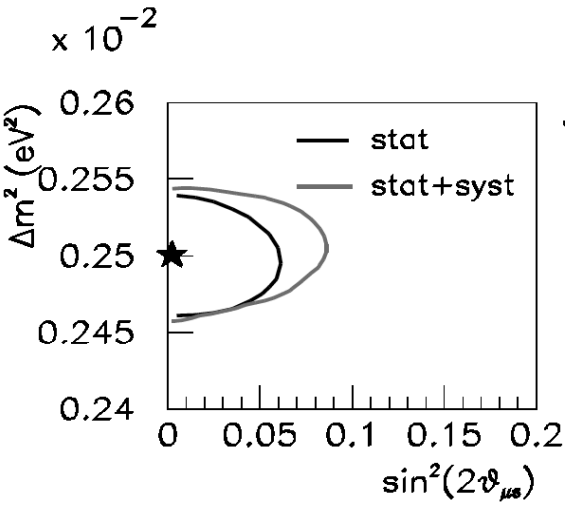

Fig. 5.7: Expected 90% confidence level allowed region for oscillation to a sterile neutrino at the atmospheric Δm^2. The black line represents the results with purely statistical errors; the gray line adds systematic errors.

detectors at different off-axis angles in the NuMI beamline.

An alternative to a second detector in the NuMI beamline would be to combine NOνA measurements taken with a proton driver with results from a high statistics, shorter baseline experiment such as the proposed JPARC phase 2 experiment [3] or proposed beta beams from the CERN SPL [5]. The difference in baselines between NOνA and either of these two proposed experiments could be exploited to provide a resolution of the mass hierarchy with similar sensitivity.

5.4. Other Physics

NOνA will also substantially improve MINOS measurements of oscillation parameters that do not involve ν_e appearance. We will just summarize the results here. Details of the simulation are presented in Chapter 8.

Figure 5.6 shows the expected results of a 20×10^{20} pot neutrino run with true parameters $\sin^2(\theta_{23}) = 1.0$ and $\Delta m_{32}^2 = 0.0025$ eV^2. The sensitivity to $\sin^2(\theta_{23})$ is approximately a factor of four greater than for MINOS with 16×10^{20} pot [1].

Figure 5.7 shows the expected results of a search for sterile neutrinos assuming no true signal.

Chapter 5 References

[1] "Proposal for a Five Year Run Plan for MINOS," Submission to the Fermilab, May 2003. NuMI note 530.
[2] CHOOZ Collaboration, M. Apollonio et al., *Phys. Lett. B* **466**, 415 (1999).
[3] T2K Letter of Intent, January, 2003. http://neutrino.kek.jp/jhfnu/.
[4] "Progress Report on the Proposal to Build an Off-Axis Detector in the NuMI Beamline," Submission to Fermilab, December 2003, Off-Axis note 31.
[5] M. Mezzetto, *J. Phys*. **G29**, 1781 (2003).

6. The Detector Design Process

6.1. Introduction

To reach the physics goals described in the previous chapters, we propose to build a 50,000 metric ton NOνA Far Detector. The size of this detector clearly makes its design and construction a substantial challenge, and the ability to construct a large fiducial mass at low unit cost is key. As described in Chapter 4, additional specific design challenges for the NOνA Far Detector are: (a) good ability to differentiate electrons from other particles, especially π^0 mesons, and (b) ability to measure electron energy as a discriminator between electrons from oscillated neutrinos and electrons from neutrinos initially present in the beam. In addition, since the detector will be operating in a relatively remote location, it should be rugged and robust and capable of operation under a range of environmental conditions with a relatively low level of upkeep and maintenance. In this chapter, we discuss the overall detector concept and the possible designs that continue to be of interest. Our baseline design choice now has liquid scintillator as the active element, and wood particleboard as the absorber. The reasons for these choices are presented here.

6.2. Calorimeter Absorber Choice

In Chapter 4 we discussed the general physics considerations that led us to the need for spatial pattern resolution and a low-Z tracking calorimeter design. After considering several possible materials, we have chosen manufactured wood sheets (particleboard), which is produced in large quantities from low-grade timber and used by the building industry in a variety of sheathing applications. The advantages of these wood board products include low cost (typically $250 - $300 per metric ton [1]) and good structural integrity, which eliminates the need for an extensive detector support design. Particleboard is composed of approximately equal parts of cellulose and urea formaldehyde with about 10% paraffin wax added. The product is therefore mostly carbon, oxygen, hydrogen and nitrogen. Particleboard has a density of about 0.7 g/cc, and we calculate that it will have radiation length of about 55 cm [2].

6.3. Calorimeter Sampling Frequency, Transverse Active Cell Size, and Energy Resolution

Given the choice of particleboard absorber, the specific features of a calorimeter using this material are set by its sampling frequency and by the transverse cell width of its active elements. Our studies [3] compared sampling fractions of 17.5% X_0, 30% X_0 and 60% X_0, concluding that the analysis cuts could be tuned for each case to give very similar signal ν_e event yields. The study aimed at maximizing a figure of merit given by the number of ν_e signal events divided by the square root of the number of background events. The background rejection was worse for 60% X_0, and about the same for 17.5 % X_0 and 30% X_0. Thus we concluded that the increased cost associated with sampling finer than about 30% X_0 was not warranted.

Similar studies [4] on the active detector cell width compared widths of 7 cm, 6 cm, 5 cm, 4 cm, 3 cm, and 2 cm, and tuned the analysis cuts for each individual case. The signal ν_e event yield declined linearly as the strip width was increased, losing about 30% of the oscillated ν_e events between 2 cm and 7 cm. The sum of the background events was minimized at 3 cm and grew larger relative to the signal as the strip width was increased beyond 3 cm. Thus we concluded that a cell size around 3 cm was appropriate and that a smaller cell size was not worth the additional cost.

We examined [5] the energy resolution of a particleboard absorber calorimeter with 30% X_0 sampling and 3 cm wide active cells and find a resolution of $\Delta E/E \sim 16\%$ for low y ν_e CC interactions in the relevant ν_e event energy range of 1 – 3 GeV. This is well matched to the inherent off-axis beam energy width of about 17% at 2 GeV (see Figure 4.5) for our signal ν_e events.

6.4. Calorimeter Active Detector Choice

For more than a year, we have focused on three possible active detector options: solid scintillator, such as the modules used in MINOS [6]; glass resistive plate chambers (RPCs), such as those used in BELLE [7]; and liquid scintillator, such as the

modules used in MACRO [8]. Each of these technologies has advantages and disadvantages.

6.4.1. Solid Scintillator versus Glass RPCs or Liquid Scintillator: Solid scintillator extrusions with multi-anode photomultiplier (PMT) readout represented a starting point for the detector design. Because it is the technology used in the MINOS detector, solid scintillator and phototubes are well understood and have an accurately known cost basis. However, this technology was significantly more expensive than the others that we considered for the detector. Major cost savings can be achieved by the replacement of PMTs with avalanche photodiodes (APDs). This option has the advantage of requiring only one substantial change from the MINOS design. However, its cost is still at the high end of the acceptable range.

Our cost estimates in Chapter 13 clearly demonstrate that a solid scintillator option with APDs is more expensive than either the liquid scintillator or the RPC design. For that reason, while solid scintillator with APD readout remains an option, we are not pursuing this design at this time.

6.4.2. Glass RPCs versus Liquid Scintillator: A major strength of RPCs is the ability to implement two-dimensional readout at each active plane. However, each RPC strip gives only digital information. A major strength of liquid scintillator is the ability to measure dE/dx in addition to position at each active plane. However, liquid scintillator only measures a one-dimensional position at each plane. Our detector simulations to date are described in Chapter 8 and suggest either parity or a slight advantage to liquid scintillator. Our cost estimates in Chapter 13 suggest that liquid scintillator with APD readout has a cost advantage over two-dimensional RPCs. On this basis, we have chosen liquid scintillator with APD readout as the baseline design and RPCs as a design alternate. Details of the liquid scintillator baseline design are described in Chapter 7. The Appendix describes the details of the RPC alternate design.

6.5. Next Steps

Detector simulation studies will continue to evaluate relative advantages of having dE/dx information over knowing two-dimensional coordinates at each plane, since our tracking algorithms and event analysis packages are still in their infancy. Studies on the costs of various detector designs are also continuing with an eye on savings in both the baseline and alternate designs. These studies will focus on liquid scintillator and glass RPCs. The solid scintillator design remains as a second alternate, but this technique is well established and does not require active development at this time, because of the experience gained from the construction and calibration of the MINOS Far Detector.

6.6. Summary

We have chosen a planar tracking calorimeter with alternate planes of manufactured wood particleboard absorber and active liquid scintillator detector elements. Our baseline design has the liquid scintillator contained in cells of PVC with light collected by wavelength-shifting fibers and read out by avalanche photodiodes. This design is different from the proven MINOS technology in three significant ways: use of particleboard rather than iron, use of liquid scintillator rather than solid and use of APDs rather than PMTs. Although we believe that these changes represent a reasonable risk, we will continue to develop the RPC alternative and explore modifications of both designs until the end of 2004, when we expect to choose the final technology for the NOνA Detector.

Chapter 6 References

[1] Off the shelf price at Home Depot™ in Geneva, Illinois, May 2003.

[2] Particle Data Group, Review of Particle Properties, Passage of Particles through Matter.

[3] Off-Axis Note 12, "A Study of Off-Axis Detector Performance as a Function of Sampling Frequency," August 2003.

[4] Off-Axis Note 21, "Resistive Plate Chambers detector for NuMI off-axis experiment," Chapter 2: Analysis and Physics Capabilities, 2003.

[5] "Letter of Intent to build an Off-axis Detector to study $\nu_\mu \rightarrow \nu_e$ oscillations with the NuMI Neutrino Beam," June 2002, page A-6. See also Chapter 8 of this proposal, Figure 8.5b.

[6] The MINOS Collaboration, "The MINOS Detectors Technical Design Report," Fermilab report NuMI-337 (1998).

[7] BELLE KLM detector group, NIM. A 449 (2000) 112-124, and NIM. A 456 (2001) 109-112.

[8] M. Ambrosio *et al*., Phys. Lett . **B434**, 451 (1998).

7. The Far Detector

7.1. Introduction

The principal physics goals of NOνA are (a) to achieve a significant measurement of θ_{13} for as broad a range of that parameter as possible, and (b) if $\sin^2 2\theta_{13}$ is sufficiently large, to begin a program of measurements of matter effects, mass hierarchy order and CP violation. The requirements placed on the Far Detector by these goals are (a) as large a fiducial mass as is practical and affordable, (b) sufficient instrumentation to distinguish electrons from π^0 background and (c) sufficient energy resolution to distinguish between oscillated ν_e's and ν_e's already present in the NuMI beam when it is produced at Fermilab.

The baseline design described here involves compromises and trade-offs because of the somewhat contradictory design criteria of high resolution and low cost. We have refined this design using the simulations described in Chapter 8. While we believe the baseline design is adequate, it may not yet be optimal. For that reason, we expect to continue to study the effects of changes in granularity, both longitudinal and transverse to the NuMI beam direction, as well as the construction methods for all of the detector components. Section 7.9 describes a research and development program to improve and refine this design, as well as to value-engineer each major system.

The baseline design for the NOνA Far Detector is a nominal 50,000 metric ton tracking calorimeter with alternate vertical planes of active liquid scintillator [1,2] and passive manufactured wood absorber. This design employs multiple repetitions of a few relatively simple elements in order to achieve large mass with low unit costs and high reliability. The detector planes are nearly normal to the NuMI beam direction. (The detector is built level and not along the 58-mrad dip angle of the beam.) The liquid scintillator planes have long, narrow cells that enable one-dimensional measurement of both position and pulse height on each plane using wavelength-shifting (WLS) fiber and avalanche photodiodes (APDs). Pairs of sequential scintillator planes provide *x* and *y* coordinates for events. The detector has a scintillator active shield on the top and sides to provide better rejection against cosmic ray background (see Chapter 10), although the short duty cycle of the neutrino beam provides the principal background rejection. The data acquisition system is triggered either by the beam spill, by a random trigger to study cosmic ray background or by optional trigger processors working off short term memories. The design has been initially optimized for efficient installation and for minimizing environmental health and safety (ES&H) costs and risks.

Table 7.1 summarizes the major design parameters for the Far Detector. Throughout this chapter, we use a mixture of US and metric units, reflecting the fact that we plan to purchase some major components as off-the-shelf items in standard US sizes. Some parameters in Table 7.1 have only nominal values because the actual mass, density and thickness of the wood absorber vary with temperature and relative humidity. The density of the mineral-oil-based liquid scintillator also varies with temperature. Details about each of the detector systems are provided in the following sections.

Mass (Nominal)	50,000 metric tons
Width	96 feet
Height	48 feet
Length (nominal)	562.5 feet
Number of Layers	750
Mass of Wood Particleboard (Nominal)	42,000 metric tons
Mass of Scintillator Extrusions	1,800 metric tons
Mass of Liquid Scintillator	6,900 metric tons

Table 7.1: Far Detector Parameters.

7.2. Design Advantages

The strengths of this liquid scintillator baseline design are the following:

7.2.1. Simplicity of Design: The NOνA Far Detector is a challenging project, mostly because of its size. The baseline design specifies many repetitions of a few, mostly low-technology and low-risk elements. The few higher technology elements, such as the wavelength-shifting fiber and the APDs have already received considerable design effort for other experiments.

7.2.2. Ease of construction: The liquid scintillator baseline design derives maximum value from the purchase of large parts of the detector from external vendors with smaller values added by interme-

diate assembly or final installation. The assembly process is mostly gluing together vendor-supplied components.

7.2.3. Reliability: This design facilitates testing of individual components both before and after assembly. Before assembly, WLS fibers will be tested for light transmission. After assembly, a device that connects to the optical connector on a module will provide a final check for fiber continuity. Pressure tests will verify the integrity of the seals at both ends of each PVC module both before shipping and after delivery to the Far Detector Laboratory. APDs will be tested as necessary prior to installation.

7.2.4. Ease of shipping and installation: Extruded PVC liquid scintillator modules will be shipped empty to the detector laboratory, reducing shipping costs because of the low weights of empty modules. The modules will be inserted empty into the particleboard absorber stacks, which are then installed in the detector. The liquid scintillator will be pumped into modules after they are placed in their final positions.

7.2.5. Passive Absorber: Particleboard is a low density, low Z and low cost material. It serves as both a neutrino target and as a structural element. Because this material is commercially manufactured in large quantities in multiple factories, several of which are in the region of the Far Detector Laboratory, shipping costs for the heaviest element of the detector are minimized.

7.2.6. Avalanche Photodiodes: Avalanche photodiodes (APDs) provide photodetectors with both low cost and high quantum efficiency. The need for cooling to minimize noise is a logistical problem, but the advantages of APDs outweigh this disadvantage. We will use development work done for CMS and silicon strip detectors to minimize both cost and risk for these detectors.

7.3. Passive Absorber

7.3.1. Overview: The proposed absorber for the NOνA Detector is wood in the form of sheets of a manufactured wood product, either particleboard or Oriented Strand Board (OSB). Particleboard is manufactured from wood particles ("sawdust"). OSB is manufactured from wood chips. The relative prices of these two materials fluctuate in accordance with supply and demand. The choice between these two products will be based on delivered price at the time of construction.

Density	650 kg/m^3
Plane	12 stacks
Stack Length	48 feet
Stack Width	8 feet
Stack Thickness (nominal)	9 inches
Passive Absorber Mass per Stack (Nominal)	4,650 kg
Particleboard Basic Unit for Stack Construction	24 feet by 8 feet by 1.125 inches thick
Particleboard Basic Unit Mass (Nominal)	330 kg
Number of Basic Units per Stack	14 units + scintillator modules in 8 layers

Table 7.2: Passive Absorber Parameters

Both of these wood products have sufficient structural strength to provide much of the required detector support structure. Quick-set, high-strength adhesives and cartridge-loaded screw guns will be used to assemble the particleboard structure. We expect to coat the exposed surfaces of the assembled blocks with a fire-retardant, to improve the overall safety of the detector.

We will fabricate the passive absorber modules at the laboratory site. The particleboard will be shipped directly from the factory to the Far Detector Laboratory. Sufficient inventory of particleboard will be maintained at the Far Detector site to insure efficient use of available installation labor.

7.3.2. Passive Absorber Details: The basic unit for the passive absorber is a sheet of particleboard 24 feet long by 8 feet wide by 1.125 inches thick. This sheet has a nominal mass of ~330 kg. In addition to the basic unit, the design uses short half units (12 feet long by 8 feet wide by 1.125 inches thick) and narrow half units (24 feet long by 4 feet wide by 1.125 inches thick). All three of these sheets are stock commercial sizes. Using three types of particleboard sheets permits assembly of the absorber without placing butt joints on top of each other.

The next level unit in the passive absorber is the "stack." A stack is 48 feet long by 8 feet wide by a nominal 9 inches thick. It consists of 8 layers—6 layers of particleboard and two layers that are half particleboard and half scintillator module. Fig. 7.1 shows the arrangement of the layers in a stack.

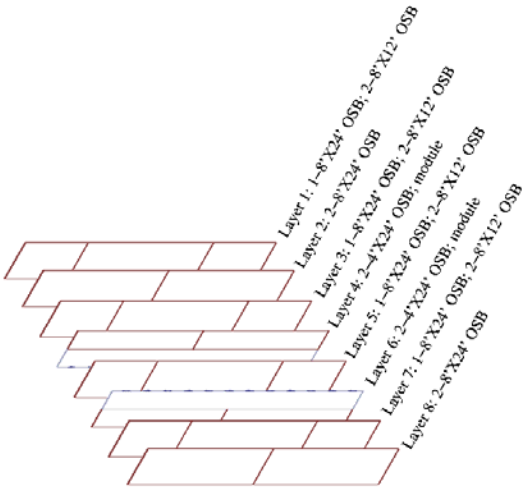

Fig. 7.1: The arrangement of layers in the "stack." (The terms "OSB" and "particleboard" are used interchangeably.)

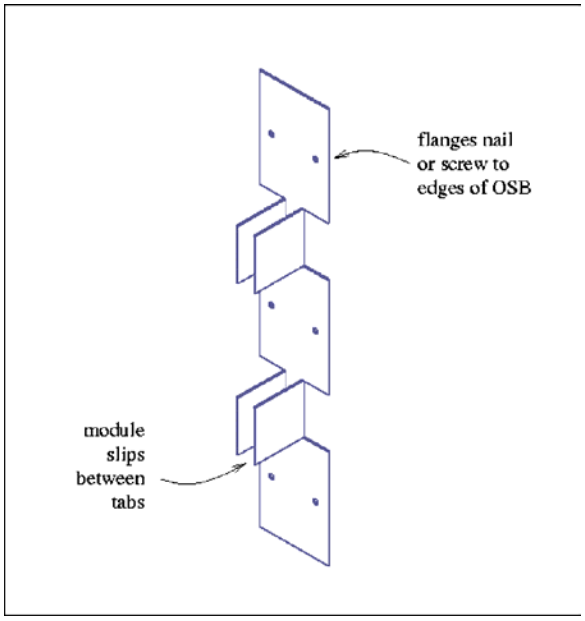

Fig. 7.2: Stack edge bracket.

There are two features built into the stack to facilitate efficient installation and structural stability. The edge bracket positively positions and holds the active detector module and provides structural stability to the stack. A design for this bracket is shown in Fig. 7.2. The other feature is that the outer panels of wood are offset so that their long edges stick out from the stack by 6 inches in opposite directions. This arrangement produces "flanges" that allow for easy installation without exposing the active modules to possible damage.

These flanges can be seen in Fig. 7.3, along with the edge brackets.

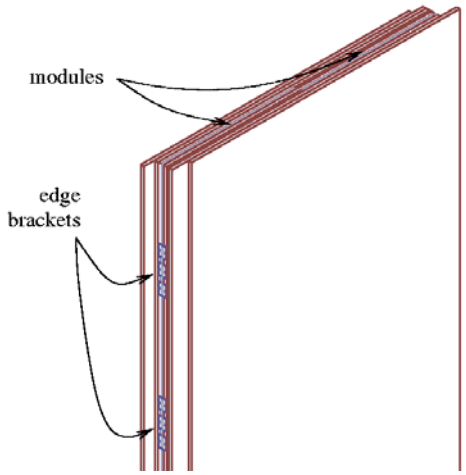

Fig. 7.3 Stack schematic. The "flanges" of particleboard (back left and front right sides) are used to attach each stack to its neighbors.

The highest level unit in the Far Detector design is the plane. As shown in Fig. 7.4, each plane consists of 12 stacks. In the odd-numbered planes, the 12 stacks are arranged side-by-side, providing a readout of the *x* (horizontal) coordinate. In the even-numbered planes, six stacks are arranged one over another, on both the east and west sides, providing a readout of the *y* (vertical) coordinate.

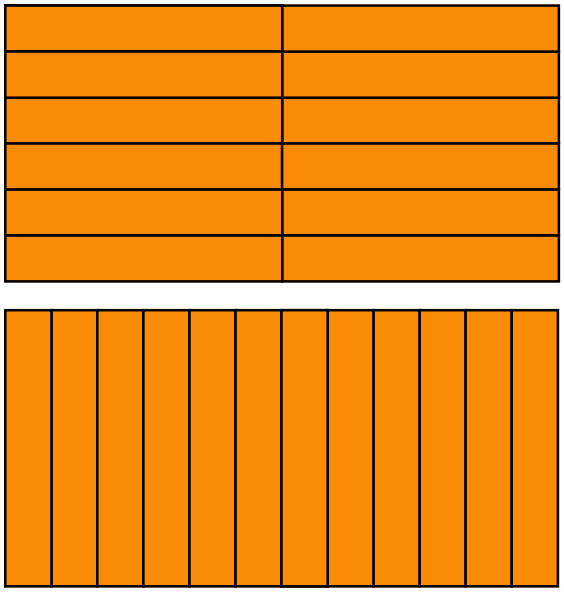

Fig. 7.4: Layout of stacks showing arrangement of alternating layers. Even numbered planes are at the top. Odd numbered planes are at the bottom. Each stack contains two scintillator modules.

7.3.3. Mechanical Integrity: We have evaluated the structural properties of this design. The most recent study used an ANSYS FEA model to determine the structural strength of individual stacks. The model of a stack is shown in Fig. 7.5. To understand the limits of the structure, the strength of the units was tested with point supports in a horizontal orientation. The results (Fig. 7.6) indicate that an extreme case of supporting the units at only the far ends would lead to buckling. However, adding a single additional point in the center of the stack would lead to small enough deflections and stresses to be within the allowed limits for the materials. Thus, due to the low pressures imposed (~15-20 psi) by self-loading, there are no buckling issues associated with the structural elements.

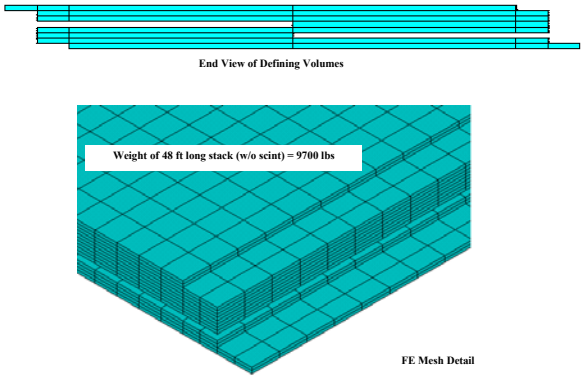

Fig. 7.5: Stack layout and sample of the FEA mesh definition.

7.3.4. Longitudinal Design: The longitudinal design needs to accommodate expansion of the particleboard, due to changes in temperature and relative humidity. We expect to develop a design using intermediate supports between groups of planes to address this requirement. These supports would allow for expansion and contraction of groups of planes. Within a plane group, we will install shims during the installation process to insure that each plane is vertical and thus to minimize any horizontal stress components in the detector.

7.4. Active Detector Elements

7.4.1. Overview: The active elements for the NOvA Far Detector consist of extruded PVC (polyvinyl chloride) cells filled with liquid scintillator and read out by a looped wavelength shifting (WLS) fiber and an avalanche photodiode (APD). The parameters of the active elements are listed in Table 7.3. The APDs are described in Section 7.5.

7.4.2. PVC Modules: The multi-cell PVC modules will be purchased as units from commercial extruders. Extruded panels with nearly the same cell dimensions as those we propose to use for NOvA are off-the-shelf items used to build walls for agricultural buildings. The extruders will ship the modules directly to several assembly sites, likely located at collaborating institutions.

The first step in the assembly process is the insertion of the WLS fiber into each cell of the extrusion. Each fiber will be "looped" at the far end of its cell, providing light collection from two fibers along the full length of the cell. In the next step, the end of the extrusion with the WLS fiber loops will be sealed with a molded plastic end cap glued to the end of the extrusion. The end cap will permit the passage of liquid from one cell to another, in order to facilitate the filling of the cells with liquid scintillator after the extrusions are installed into the detector.

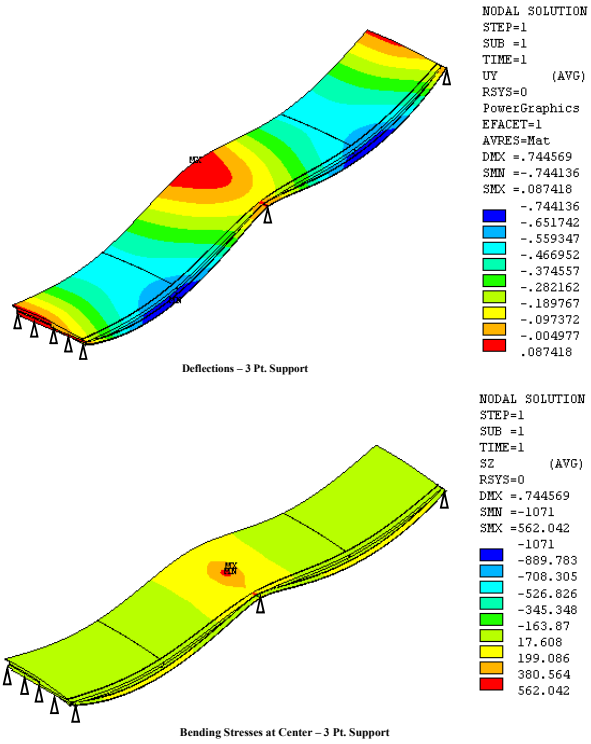

Fig. 7.6: ANSYS calculation of deflections (top; maximum is 0.75 in) and stresses (bottom; maximum is 562 psi) in a horizontal stack with only three support points under self loading.

Extrusions	Polyvinyl Chloride (PVC) with 10%-15% TiO_2 for reflectivity
Extrusion Length	48 feet
Extrusion Width	4 feet
Extrusion Thickness	1.125 inches
Cells per Extrusion	30
Extrusion Outer Wall Thickness	1.5 mm
Extrusion Inter-Cell Wall Thickness	1 mm
Density of PVC	1,400 kg/m^3
Extrusion Mass (Empty)	100 kg
Cell Width (inside dimension)	3.96 cm
Cell Thickness (inside dimension)	2.56 cm
Cell Volume	0.0148 m^3
Extrusions in the Detector	18,000
PVC Mass in the Detector	1,800 metric tons
Liquid Scintillator	Bicron BC517L
Density of Liquid Scintillator	860 kg/m^3
Liquid Scintillator Mass (per cell)	12.7 kg
Liquid Scintillator Mass (per extrusion)	380 kg
Extrusion Mass (Full)	480 kg
Cells Per Plane	720
Number of Cells in the Detector	540,000
Liquid Scintillator Mass in the Detector	6,900 metric tons
Wavelength Shifting Fiber (WLS)	Kuraray
WLS Diameter	0.8 mm
WLS Length Per Cell	32 m
WLS Length for the Detector	17,280 km
WLS Volume in the Detector	8.7 m^3
WLS Mass in the Detector	9 metric tons

Table 7.3: Active Detector Element Parameters

The extrusion assembly is completed by routing the fiber ends through a manifold that both seals the second end of the extrusion and directs the fibers in a specific order to an optical connector. See Fig. 7.7 for a conceptual diagram. The manifold is also glued to the PVC extrusion. In addition to the optical connector, located at the end of the "fiber guide tube", the manifold also provides a filling hole for the liquid scintillator, an air hole for venting the extrusion as the liquid scintillator is filled and a volume for thermal expansion of the liquid scintillator as the ambient temperature changes.

The PVC in the extrusions will be loaded with titanium dioxide for reflectivity. We have tested samples of PVC loaded with various concentrations of TiO_2 and measured their reflectivity at several wavelengths. These measurements indicate that a loading of 10 to 15% TiO_2 will yield a reflectivity greater than 96% at 425 nm. TiO_2 is the additive that gives commercial PVC its white color. Off-the-shelf samples have reflectivities of ~94%. We will monitor the reflectivity of the extrusions as they are manufactured. Fig. 7.8 shows the results of a measurement made on one of the PVC samples that we tested.

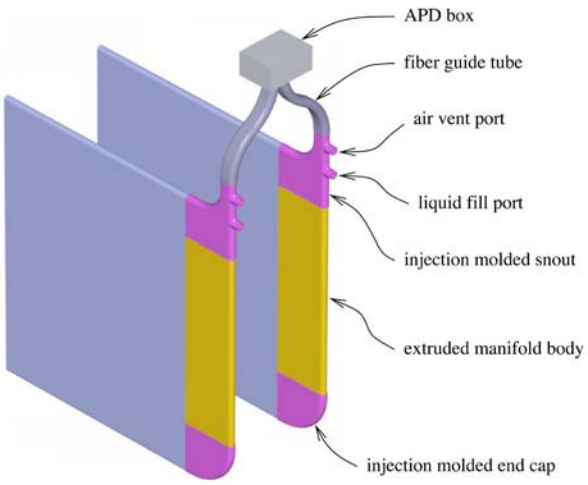

Fig. 7.7: A conceptual diagram of the manifold to lead fibers from the scintillator modules. The ends of 2 horizontal liquid scintillator modules are shown extending off to the left.

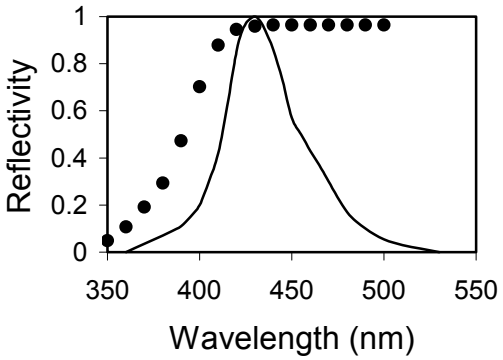

Fig. 7.8: Reflectivity of PVC sample (black circles); the solid line is the emission spectrum of BC517L.

An important aspect of this design is to assure the long-term stability and reliability of the assembled liquid scintillator modules. We have already made a number of both static tests and accelerated lifetime tests for integrity of glue joints, burst resistance, puncture resistance, mechanical "creep" and possible chemical

interactions among glues, PVC, WLS fibers and liquid scintillator. Accelerated lifetime tests involved placing samples in ovens for long-term storage at elevated temperatures. None of these tests has shown significant problems. However, qualification of specific materials and performance of static and accelerated lifetime tests, for both materials and assembled modules, are included in our R&D plan, described in Sec. 7.9.

7.4.3. Wavelength-Shifting (WLS) Fiber: WLS fiber provides an efficient method for collecting light from the long narrow cells used in this detector. The WLS shifts light from shorter wavelengths to green (~550 nm). The use of WLS fiber makes the light output relatively independent of the optical transmission of the liquid scintillator itself. The MINOS Far Detector provides considerable experience on the construction and operation of this light collection design. We expect to purchase multiclad WLS fiber from Kuraray, the same type of fiber and the same vendor used for MINOS.

Essentially the only adjustable design parameter of the fiber is the diameter. Diameters greater than ~1.2 mm are difficult to spool and ship. For fiber diameters around 1 mm, the light collection efficiency depends mostly on the diameter of the fiber while the cost of the fiber depends on the cross-sectional area (volume). Thus, in terms of photons per dollar, two thinner fibers are more efficient than one thicker fiber. Also, the looped fiber design provides a factor of two more light from the far end of each cell, where light output is most important, than two individual fibers with nonreflecting far ends. Using the looped design, as described in Section 7.4.2, we collect ~42 photons for a 1-mip particle from the 48-foot length of the liquid scintillator cell using 0.8 mm diameter fiber. The two ends of the looped fiber will be brought together in the optical connector and presented to one 1.6 mm by 1.6 mm pixel of the APD.

The following figures illustrate some of the characteristics of multiclad WLS fibers. Fig. 7.9 shows that relative light yield, for fiber diameters around 1 mm, is approximately a linear function of diameter.

Fig. 7.10 demonstrates the light collection advantage of a looped fiber design. Note that the ratio of light output for a looped fiber to a single fiber is largest for light from the far end of the liquid scintillator cell.

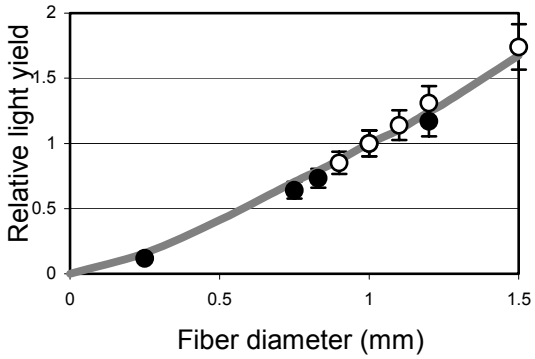

Figure 7.9: Relative light yield as a function of WLS fiber diameter. Open circles - from measurements made for MINOS Detector; closed circles - recent measurements; solid line - Monte Carlo simulation. (Data are normalized to unity at 1 mm diameter.)

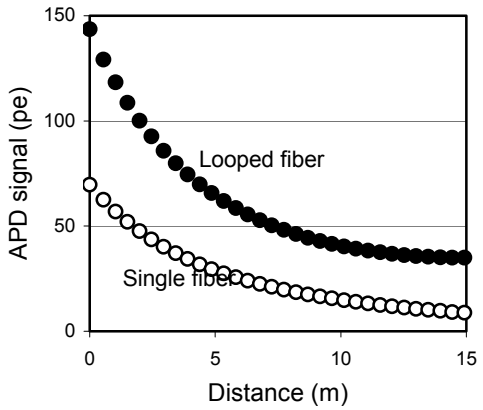

Figure 7.10: Predicted APD signal for looped and single 0.8 mm diameter fibers.

Fig. 7.11 shows our calculation of light output as a function of the location of a single, unmirrored WLS fiber within a liquid scintillator cell. The light output is quite constant over most of the cross-section of the cell but decreases significantly when the fiber is actually touching a cell wall. Our simulations assume realistic fiber locations, with most of the length of a fiber at or near an extrusion cell wall. As part of our R&D program, we intend to explore ways to control the fiber location and to insure that the loop in the fiber is located at the far end.

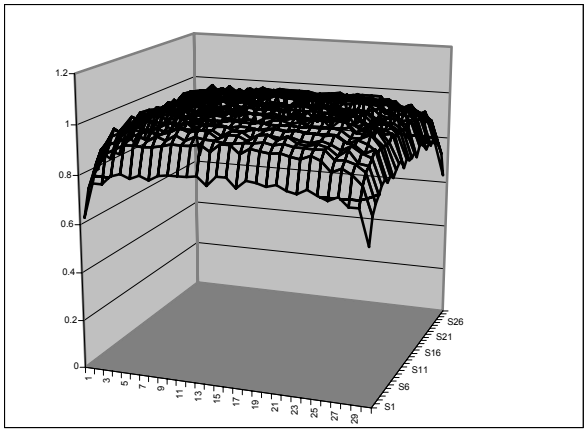

Fig. 7.11: Relative light yield for a single, unmirrored fiber as a function of location within a scintillator cell.

We have performed a number of tests to indicate the validity of a multiplicative light output model, with essentially no correlation among the multiplicative factors. That is, light output is the product of the intrinsic scintillator output times a factor for extrusion reflectivity times a factor for the diameter of the WLS fiber times a factor for the length of the WLS times a factor for the placement of the WLS times a factor for efficiency of the coupling to the photodetector times a factor for the quantum efficiency of the photodetector. The independence of the factors in this model means that tests can be performed for each factor separately, with only occasional end-to-end tests to continue to confirm the accuracy of this approach.

Fig. 7.12 shows a pulse height spectrum of the type we have measured to check the accuracy of our model. This particular spectrum actually results from cosmic ray muons crossing 7.5 m from the readout end of an "off the shelf" extrusion with a 2.1 cm by 2.8 cm channel. The extrusion walls had a 94% reflectivity. The measurements used a hybrid photodiode detector with a quantum efficiency of 12%. The average pulse height is 3.2 photoelectrons. Using our model, and adjusting for differences in detector parameters, we find an expected light yield of 42 photons at the APD face, for a minimum ionizing particle crossing the far end of a scintillator tube.

7.4.4. Liquid Scintillator: The scintillator we propose to use is Bicron BC517L [2] (also sold as Eljen EJ321L), essentially pseudocumene in a mineral oil base. BC517L has a moderate light output, 39% of anthracene, when fresh, and 27% of anthracene, when fully oxygenated. The advantages of BC517L include stability, low cost, availability in large quantities, low toxicity, high flashpoint and low potential as an environmental hazard. Generally, higher light output formulations are less stable and more difficult to use, especially in large quantities.

The oxygenation of BC517L generally proceeds to a stable light output within a few months. Fig. 7.13 shows the results of measurements we have made of pulse-height spectra from solid scintillator, fresh liquid scintillator and oxygenated liquid scintillator. Our simulations use the light yield from fully oxygenated scintillator.

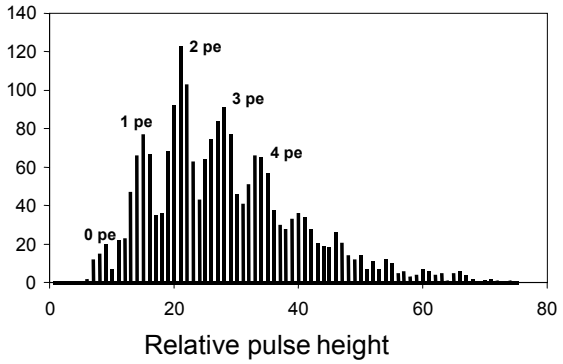

Fig. 7.12: Pulse height spectrum of cosmic ray muons at 7.5 m distance; 2.1 cm x 2.8 cm cell; 1.0 mm WLS fiber; HPD photodetector.

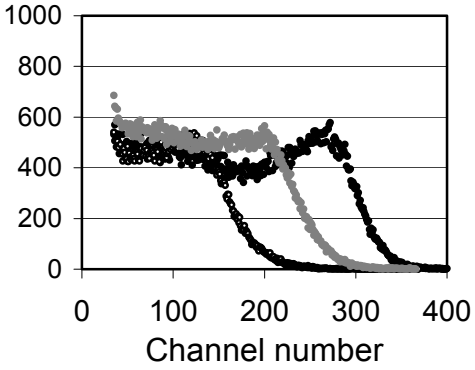

Fig. 7.13: Pulse-height spectra for scintillators showing Compton edge of ^{137}Cs gammas. Black squares (right): MINOS scintillator; gray squares (middle): fresh BC517L; open squares (left): 5-year old BC517L.

The total mass of liquid scintillator in the NOνA Far Detector is 6,900 metric tons or 8.1 million liters or ~2 million gallons. An installation rate of one plane per shift requires a pumping rate of

~300 gallons per hour, about the same rate at which the MACRO detector was filled.

We expect to mix the liquid scintillator in an on-site mixing plant by combining the concentrated fluors shipped from the vendor with the separately purchased mineral oil base. Once mixed, the liquid scintillator would be stored in a holding tank until it is tested for light yield and qualified for use in the detector. A piping system will transfer mixed and tested scintillator from the mixing location to the detector area and then along one of the long sides of the detector to a flexible hose, whose attachment to the fixed piping system would be moved as the detector filling progresses.

Our installation plan assumes on-site storage of mineral oil in five 15,000-gallon tanks and 5500 gallons of storage for scintillator fluors and wave-shifter concentrate. Two 15,000-gallon tanks are used for mixing the mineral oil and concentrate.

7.5. Avalanche Photodiodes (APDs)

7.5.1. Overview: The proposed light detectors for the baseline design are avalanche photodiodes (APDs) [3] manufactured by Hamamatsu and similar to the 5 mm × 5 mm APDs developed for use in the Compact Muon Solenoid (CMS) Detector at the LHC [4]. Table 7.4 summarizes the key parameters of the NOνA APDs.

Manufacturer	Hamamatsu
Pixel Size	1.6 mm by 1.6 mm
Pixel Pitch	2.3 mm
Array Size	16 pixels
Package Size	2 arrays
Quantum Efficiency (>525 nm)	85%
Pixel Capacitance	10 pF
Bulk Dark Current (I_B) at 25 C	10 pA
Bulk Dark Current (I_B) at -15 C	0.15 pA
Peak Sensitivity	600 nm
Operating Voltage	400 ± 50 volts
Gain at Operating Voltage	~100
Operating Temperature (with Peltier Cooler)	-15 C
Expected Signal-to-Noise Ratio (Muon at Far End of Cell)	10:1
APD channels per plane	720
APD pixels per plane (including unused pixels)	768
APD arrays per plane	48
APD channels total	540,000
APD pixels total	576,000

Table 7.4 Avalanche photodiode parameters.

APDs [5] have two substantial advantages over other photodetectors—high quantum efficiency and low cost. The high APD quantum efficiency enables the use of very long scintillator modules, thus significantly reducing the electronics channel count. An operational characteristic of APDs is their high thermal noise, which can be reduced by lowering their operating temperature. For the NOνA Far Detector, we propose to operate the APDs at -15 C, using thermo-electric (Peltier-effect) on-board coolers.

Fig. 7.14 compares the quantum efficiency of a Hamamatsu APD to that of the PMT used in the MINOS Far Detector. In the wavelength region relevant to the output of the WLS fibers, that is 500 to 550 nm, the APD quantum efficiency is 85% *vs.* 10% for the PMT. The figure also shows emission spectra measured at the ends of different lengths of WLS fiber. The quantum efficiency advantage of the APD increases with wavelength. Thus, the APD is even more advantageous for long propagation distances in the WLS fiber, exactly where quantum efficiency is most important because of low light levels. This wavelength dependence leads to a longer effective attenuation length for light in the fiber, as shown in Fig. 7.15, where the attenuation data were obtained using a Hamamatsu APD and a PMT with a bialkali photocathode.

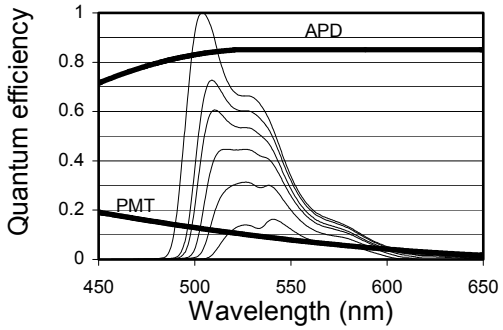

Fig. 7.14: Quantum efficiencies of APD and PMT (bialkali photocathode) as a function of wavelength. The figure also shows WLS fiber emission spectra measured at lengths of 0.5, 1, 2, 4, 8, 16 m, respectively and illustrates the shift of the average detected wavelength as attenuation (fiber length) increases.

The current commercially-available Hamamatsu APD has a pixel size of 1.6 mm by 1.6 mm. A photograph of the 32 pixel APD package is shown in Figure 7.16. We propose to purchase 16-pixel

arrays in the bare die form and mount the chip, cooler, electronics and optical coupler on a single printed circuit board.

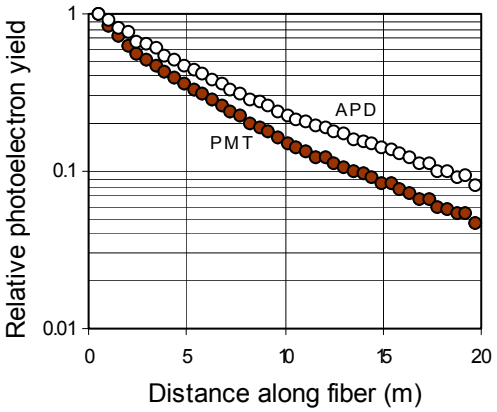

Fig. 7.15: Relative photoelectron yield from 1.2 mm diameter WLS fiber, for APD and PMT. The data have been normalized at 0.5 m to illustrate the effect of the longer wavelength response of the APD.

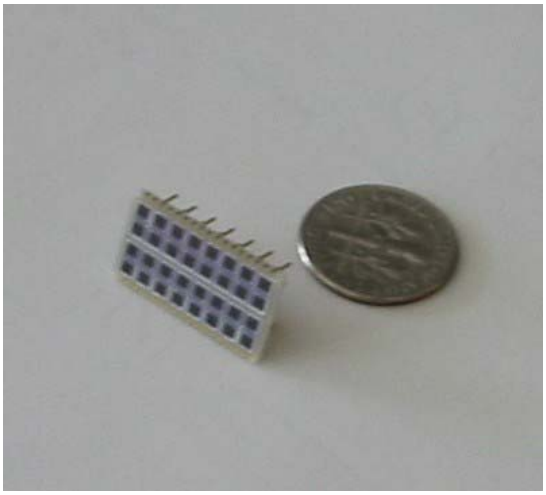

Fig. 7.16: A Hamamatsu APD package shown with a dime. Two 16 pixel arrays are packaged together.

7.5.2. Photodetector Requirements: Photodetectors for the NOνA Far Detector must be able to efficiently detect single minimum ionizing particles traversing the far ends of scintillator strips, ~17 m (of fiber length) away. Each photodetector pixel should be large enough to collect the light from both ends of a 0.8 mm diameter looped fiber.

As described in Sec. 7.4.3, we estimate that a single minimum ionizing particle, normally incident at the far end of a liquid scintillator tube, will produce ~42 photons at the face of the APD. The quantum efficiency for an APD in the region of the spectrum where the light is emitted is 85%, giving a signal for such a particle of ~35 photoelectrons. This signal must be distinguishable from the electronic noise with high efficiency.

7.5.3. Fundamentals of APD operation: The general structure of an APD is shown in Figure 7.17. Light is absorbed in the collection region, electron-hole pairs are generated and, under the influence of the applied electric field, electrons propagate to the *p-n* junction. At the junction, the electric field is sufficiently high that avalanche multiplication of the electrons occurs. The multiplication (M) of the current is determined by the electric field at the junction, and by the mean-free-path of electrons between ionizing collisions, which depends on both the accelerating field and on the temperature. The temperature dependence occurs because of the probability of electron-phonon scattering increases with temperature.

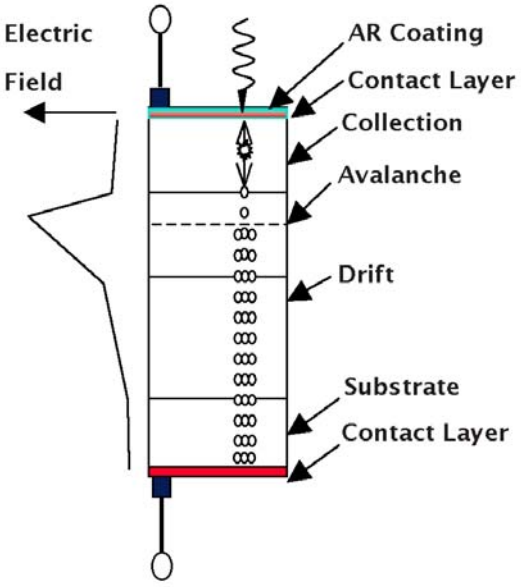

Fig. 7.17: The basic structure of a blue/green sensitive APD. Light crosses the anti-reflection coating at the surface and is absorbed in the collection region. Photoelectrons drift in the electric field to the junction where they undergo avalanche multiplication.

APDs produce intrinsic noise [5] from electron-hole pairs generated thermally in the collection region of the diode. These electrons pass through the junction and are not distinguishable from those

that are photon induced. The thermally generated current of electrons through the junction is called the bulk current (I_B). Other factors such as non-uniformities and other manufacturing imperfections lead to increases in the noise output of the diode.

After APDs have been sorted at the factory, their gains are easily determined by their bias voltages and their operating temperatures. In this detector, we will maintain the operating bias to a precision of ~ 0.2 Volts and control temperature to ~0.5 C. The choice of the -15 C operating temperature for the NOνA Detector application is determined by the need to suppress the bulk-dark current I_B. Roughly, there is a decrease in I_B of a factor of two for every 7 C drop in temperature. Values for I_B of 4.5 pA/mm^2 of sensitive area are typical for the CMS APDs at room temperature.

7.5.4. Experience with the CMS APDs: The CMS experiment will use 124,000 Hamamatsu APDs, with 5 mm × 5 mm pixels, to read out the lead-tungstate calorimeter. To date, more than 100,000 devices have been received from the manufacturer and tested. The quantum efficiency for these devices is consistently at 85% at 550 nm as can be seen in the Fig. 7.18.

7.5.5. APDs for the NOνA Far Detector: We purchased commercially available 32-channel APD arrays from Hamamatsu for possible use in the NOνA Far Detector. The measured dark current, pixel gain and pixel separation for one of the sample arrays are shown in Figs. 7.19, 7.20 and 7.21. The dark current is consistent with expectations from CMS APD measurements. The gain is uniform from pixel to pixel on the same chip. The gain over the sensitive area of an individual pixel is also uniform. The fall-off on the pixel edges in Fig. 7.21 mostly reflects the finite spot size used to illuminate the APD pixels.

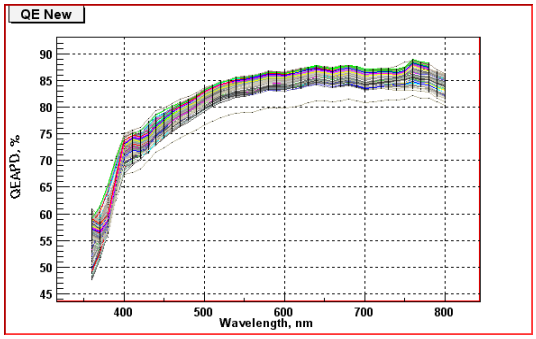

Fig. 7.18: Quantum efficiency of several hundred CMS APDs.

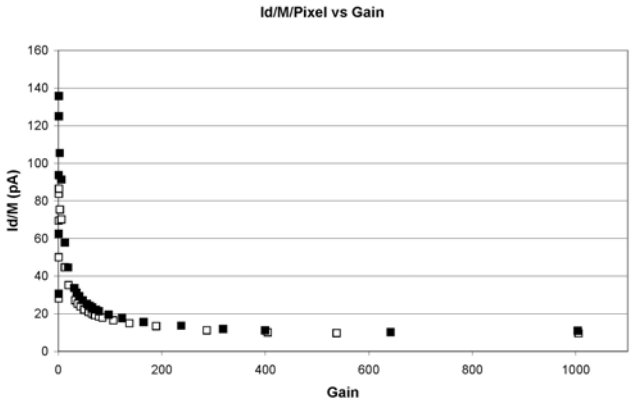

Fig. 7.19: Dark current I_d divided by gain *vs.* gain in a typical NOνA APD at 25 C. The asymptotic value of the current is I_B , which is 10 pA for this sample.

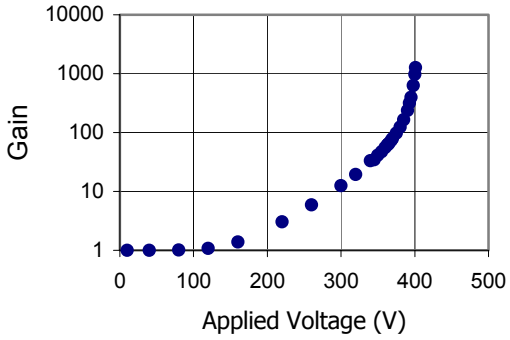

Fig. 7.20: Gain *vs*. applied voltage at 25 C.

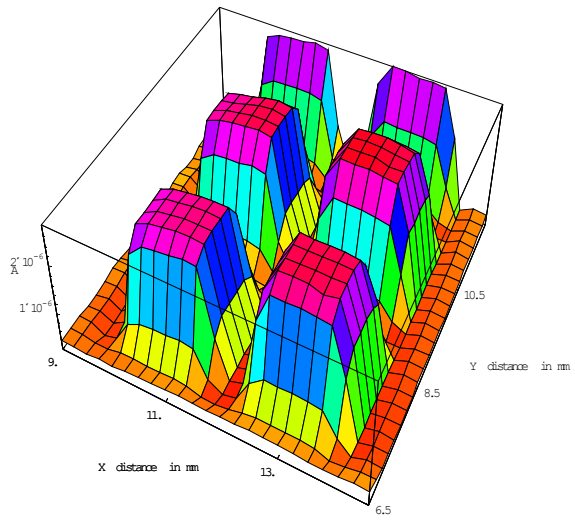

Fig. 7.21: Fine point scan across part of the APD array.

7.5.6. Electronic Readout: Readout of the APDs requires a preamplifier that can sample the signal throughout a 10 μs spill gate. The proposed architecture is based on the Fermilab MASDA (Multi-Element Amorphous Silicon Detector Array) chip [6,7,8] and the SVX4 (a multi-channel amplifying and digitizing chip developed for CDF and D0). In this design, the signal will be amplified by a high gain integrating amplifier with an RC time constant of ~350 ns. The amplifier output will be stored in a switched capacitor array every 500 ns. At the end of beam spill, the signals in each capacitor will be routed via an analog multiplexer to a 40 MHz 10-bit ADC, with one ADC for every 32 APD channels.

7.5.7. Noise: Based on our work with the MASDA chip, we expect a noise level of ~350 electrons is achievable without matching of the input capacitance of the chip to the capacitance of an APD pixel. This should be viewed as an upper limit on the noise level achievable with a practical mass-produced device. We expect to operate the APD at a gain of 100, which reduces the effective equivalent noise charge (ENC) to 3.5 photoelectrons at the photodetector input.

For two 16-pixel APD arrays we measured the average bulk dark current (I_B) per pixel as 10 pA at 23 C. This is consistent with the bulk dark current of the CMS APD: 5 pA/mm^2, corresponding to 12 pA/pixel. A current of 10 pA corresponds to a current of 10 electrons every microsecond. At our operating temperature of -15 C, the APD background rate is ~1 thermally-generated electron in our 1 μs sampling time.

The requirement for the readout is then to detect a signal with an average value of ~35 photoelectrons spread over the short time interval determined by the WLS fluor decay time, with a background rate of 1 thermally-generated electron per microsecond using an amplifier with an effective ENC of 3.5 electrons. Fig 7.22 shows the estimated signals from one and two minimum ionizing particles, considering all noise factors, compared with the thermally generated noise pedestal. The graph shows good discrimination between zero, one and two normally incident muons crossing the far end of the scintillator strip.

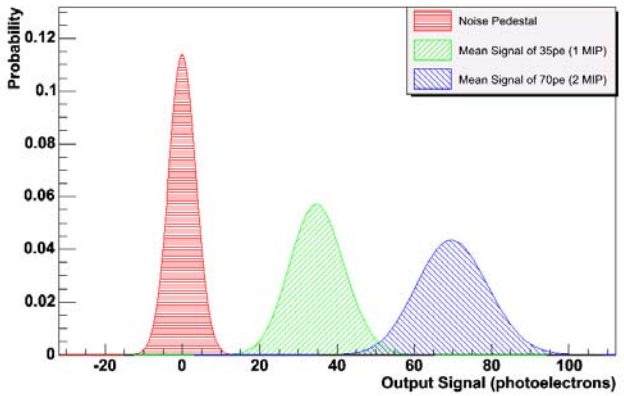

Fig. 7.22: Expected APD signals from noise, 1 and 2 minimum ionizing particles. The calculation uses a total noise of 350 electrons and signal levels of 35 and 70 pe.

7.5.8. Digitizing and Readout Architecture: The proposed digitizing architecture is based on the SVX-4 structure. This configuration consists of an integrating amplifier for each APD pixel, whose output is coupled to an on-board switched capacitor array (SCA). During a 10 μs spill gate, the output of the amplifier is stored on the capacitors in the SCA ASIC at 500 ns intervals.

After the data acquisition interval, the signal on pairs of capacitors will be compared. That is, if the capacitors are labeled C_1, C_2, C_3 etc., then the charge on C_3 is compared with that on C_1 and the difference coupled through an analog multiplexer to a 10-bit ADC where it is digitized and stored. When all the voltage differences for that pixel have been digitized the process is repeated for the SCA associated with the next pixel. A single on-board 40 MHz ADC will be able to digitize the

signals from the 30 pixels that are used to readout a module in ~15 ms.

Adjacent modules will be read out in pairs by a single readout box located between them. We will use four APD arrays with a total of 64 pixels to read out the 60 strips in two modules. The voltage (400 ± 50 V) to bias the four APD arrays (selected to have the same operating voltage) will be supplied from an on-board Cockroft-Walton voltage generator. Each board will have a 64-channel ASIC. Signals are digitized by a pair of 40 MHz 10-bit ADCs. The APD will be cooled with a single-stage thermo-electric (Peltier) cooler. The thermal power generated in the four APD arrays is ~25 μW, so the most significant thermal load will be from local conduction along the fibers and through the electrical interconnects. Temperature monitoring and control, clock regeneration and I/O functions will be controlled with a low-power FPGA. In the design of the readout box the APDs will be mounted on the opposite side of the board from the other electronic components to minimize the thermal load.

7.5.9. APD Housing: The box housing the APDs and their associated electronics must fulfill several functions: (a) match the fibers to the APDs, (b) provide a light tight connection to the scintillator module, (c) house the APDs and the associated electronics, (d) remove heat from the electronics and the Peltier-cooled APDs, (e) protect the cold surfaces from humid air to prevent condensation and (f) provide structural strength. The manifolds are designed such that two scintillator modules can connect into a single APD box. Schematic diagrams of an APD box are shown in Figs. 7.23 and 7.24.

The APD arrays, the PCB, the heat sink, and the electronics are housed in an aluminum sheet-metal box that serves as a Faraday cage. The box also contains connectors that supply the electronics with low voltage, clock signals and electronics readout. The APD box will be designed to be serviceable and light tight.

7.6. Data Acquisition

7.6.1. Data Acquisition Modes: The primary task for the readout and data acquisition system is to concentrate the data from the large number of APD channels into a single stream, which can be analyzed and archived. The complexity of the

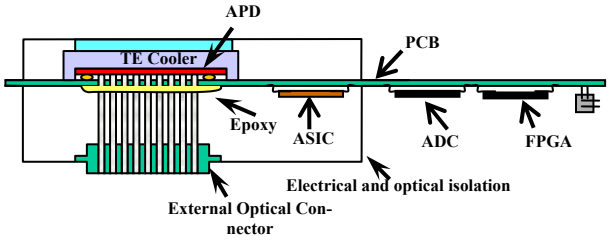

Fig. 7.23: Side view of the components in an APD electronics box. The box receives the signals from two scintillator modules through optical connectors. Peltier-elements (TE cooler) are thermally bonded to the APDs on the PCB and are in thermal contact with the heat sink to remove the heat from the box.

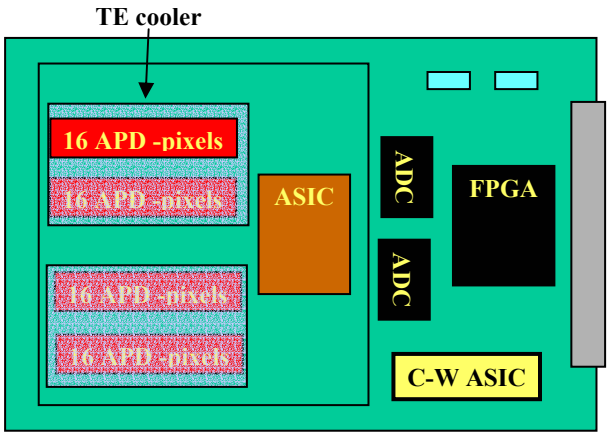

Fig. 7.24: Top view of the component layout in an APD electronics box.

DAQ electronics is dependent on whether the system is externally triggered or self-triggered. An externally triggered system would be "live" for only a short period of time, for example, ~10 μs surrounding the neutrino beam spill. The system could also be randomly triggered at other times in order to measure cosmic ray background. A self-triggered system would be continuously sensitive and would use trigger processors to analyze the data stream looking for hit clusters that might indicate an interesting event. The externally triggered DAQ is clearly easier and cheaper to build and is the system proposed here. We have designed the system so that a continuous readout mode capability could be added at a later time. The parameters of the DAQ system are listed in Table 7.5.

APD boxes per plane	12
APD channels per box	60
APD pixels per box (including un-used pixels)	64
Digitization	10 bits every 0.5 μsec
Noise rate per channel	$<10^3$ Hz
Bytes per hit (channel ID, TDC, ADC, status)	≤8

Table 7.5: Specifications for DAQ system.

The data rate per APD box is ~0.5 MB/s, so that an average of 10 bytes is produced per APD box per 20 μs readout, yielding approximately 100 kB per readout for the entire detector. If the readout is triggered at ~100 Hz to measure cosmic ray background, the total data rate is ~10 MB/s. In comparison, the total data rate for the entire detector with a continuous readout mode could be up to 5 GB/s.

The DAQ threshold is set to satisfy two requirements: efficient detection of a minimum ionizing particle and a low noise rate such that the DAQ system is not overwhelmed by spurious hits. Since the system will digitize everything in a spill gate, the threshold can be adjusted to meet these goals. For example, let us assume an electronics noise level of 350 electrons, an APD gain of 100 and a mean signal from a minimum ionizing particle of 35 photoelectrons, or 3500 electrons after the APD. If we set a threshold of 2000 electrons, we expect greater than 99% efficiency for a minimum ionizing particle with a probability for a noise hit of less than 3×10^{-8} in 1 microsecond.

7.6.2. System Architecture: The overall concept of the readout and DAQ system is similar to that of other experiments. Data from each APD is directed to a front-end ASIC, which integrates, pipelines and converts the APD signals to digital values. A Field-Programmable Gate Array (FPGA) receives the data from the front-end ASIC, applies zero suppression and timestamps, and then buffers the digitized values before serialization and transmission to the DAQ. The FPGA can also provide control and monitoring of the APD box. The APD-box FPGA provides an external interface using standard Ethernet protocols. The baseline design specifies less expensive electronic Ethernet interconnections using standard Cat5 cabling. Optical interconnections have the advantages of higher bandwidth and no ground loops at somewhat higher system cost. The final choice will require value engineering.

The overall organization of the DAQ system will be as a collection of local rings readout through Readout Concentrator Nodes (RCN) as shown in Fig. 7.25. The advantage of the ring architecture is that loss of any single ring member disables only that element and not the entire ring. For design simplicity and to reduce requirements for spares, each APD box will have a switchable capability to act as either a ring master or a ring slave. The baseline design is to connect 96 APD boxes from 8 successive planes into each local ring. This gives 750/8 = 94 rings. Since the total detector data rate is 10 MB/s, the rate per ring is ~100kB/s.

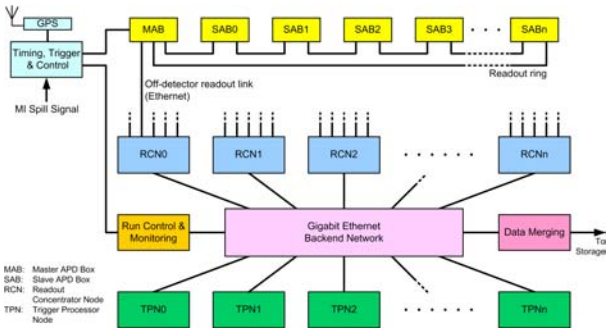

Fig. 7.25: Overview of the entire DAQ system: The data from a number of APD boxes (SAB) will be collected and transmitted by a Master APD Box (MAB) via Ethernet. Data from a number of MAB will be funneled via Ethernet into a Readout Concentrator Node (RCN). The RCNs will transmit this data via Ethernet to trigger processor nodes (TPNs). The TPNs will run trigger algorithms on this data to decide which data to write to the data storage. A timing system will distribute clock signals (locked to the GPS time) to all MAB. These signals would be redistributed by the MABs to the SABs. The timing system also receives the Main Injector spill signal for redistribution.

We expect to use ~10 Readout Concentrator Nodes (RCNs) to collect data from the APD box Ethernet rings. The RCNs will be PC's with multiple Ethernet cards. Each ringmaster APD box will be connected to a dedicated Ethernet interface card on a RCN. The RCNs will direct all data from a specific trigger to one of several Trigger Processor Nodes (TPNs). The TPN that receives all the data from one particular trigger will then determine whether and how the data from that trigger should be archived for later off-line analysis.

Control information will follow an inverse path via the same network. Detector Control System (DCS) computers will send data to the RCNs, which will then distribute control signals to the master APD boxes which will then pass control information around the readout rings.

7.6.3. Timing System: The synchronous readout of data from the detector in the system proposed here requires distribution to the APD boxes of (a) 2 MHz clock, (b) a 1 pulse per second (PPS) signal to reset the hit timestamp counter and (c) a readout trigger ("spill") signal.

These signals are easily modulated onto a 10 MHz carrier frequency, so only a single pair of cables is needed to distribute them. The timing signals are centrally generated and fanned out to the master APD boxes. These boxes distribute the timing signals to all other APD boxes in the ring.

The clock and PPS signals would be locked to a GPS receiver, providing a stable, high-quality absolute time reference for the detector. In order to trigger a readout in time with a beam spill, the spill signal generated at the Main Injection must arrive at the central timing unit around 1 ms before the neutrinos arrive at the detector. A well-defined route for this signal is therefore necessary; either via a reliable, low-latency network connection from FNAL, or possibly via a dedicated radio link.

7.7. Environmental Safety and Health

7.7.1. Introduction: The NOνA Far Detector is an extremely large and massive device. The safe construction and installation of the detector will require a well-planned, well-executed and intensive program of safety, including training, equipment and monitoring. Because of the size of the Detector, the most significant hazards are likely falls and falling objects. We expect that an on-site Environmental Safety and Health (ES&H) staff will be required to insure the necessary level of precautions during the assembly of the detector. The following sections discuss some ES&H considerations for the major detector elements.

7.7.2. PVC: While polyvinyl chloride (PVC) will burn when exposed to an ignition source, it is not particularly flammable. Safety experts at both Fermilab and Argonne have indicated no special problems with our proposed use of PVC. Similarly, the Minnesota Department of Natural Resources believes that our proposed PVC use is in compliance with both OSHA and MSHA regulations, although we believe that only OSHA regulations are actually controlling. Of course, we expect to take suitable precautions to prevent an ignition source coming into contact with the PVC modules. We also expect to install both a smoke detection system and a fire suppression (sprinkler) system. We expect to work with local fire companies to develop and rehearse plans for both personnel rescue and fire suppression in the case of fire.

7.7.3. Scintillator: The material safety data sheet for BC517L (Bicron, 1984) indicates a flashpoint of 102°C and shows that none of the components (mineral oil, pseudocumene ~10%, small amounts of PPO) are highly toxic. Normal precautions with ignition sources will be taken. For example, liquid scintillator or containers used for liquid scintillator, even if empty, will not be exposed to ignition sources. Personnel working with the scintillator or its components will be provided with appropriate personnel protection equipment, since overexposure to BC517L can cause irritation of the eyes. Eating and drinking will not be permitted while working with the liquid scintillator since excessive inhalation or swallowing of material can be dangerous. We will design and install secondary and tertiary containment to limit dispersal of the liquid scintillator in the event of leaks or spillage. Such backup containment measures may include interior walls within the detector and mixing buildings and exterior impermeable berms.

We have investigated the flammability of scintillator-filled extrusions. Test modules have been subjected to temperatures sufficiently high to initiate burning of the PVC. A propane torch required 0.75 to 1.0 minutes to ignite a PVC extrusion. When the flame from the torch was removed, the extrusions self-extinguished within 5 seconds. Modules filled with scintillator were even more difficult to ignite, because of the considerably higher heat capacity. The scintillator-filled PVC modules also self-extinguished when the propane torch was removed.

7.7.4. Absorber: The particleboard absorber is also environmentally benign. The major ES&H concern regarding the absorber is again flammability. We expect to study the utility of coating the exposed absorber surfaces with a fire-retardant. As with the other components, smoke detection and a fire suppression system will address some of these concerns. The detector construction scheme, in which the absorber and the PVC extrusions are

fastened together into a monolithic block reduces the exposure of both the absorber and the PVC extrusions to oxygen, thus reducing the severity of the flammability hazard.

7.8. Installation

The Far Detector installation goal is to achieve a rate of 12 detector stacks or one detector plane installed per day or 4 planes per week (two 10 hour shifts per day for a 4 day week). Including ramp up, the entire installation process will take 4 years to complete, proceeding in parallel with module fabrication. We believe this rate is achievable because (a) there are few different types of parts, (b) the assembly methods require few special skills and (c) the task is large enough to afford some investment in optimal lifting and moving apparatus and fixtures.

To meet this proposed installation rate, an average of 9-10 truckloads of particleboard and two truckloads of scintillator modules must be delivered to the detector site each workweek. We assume that these materials will be delivered to either an attached or separate receiving and preassembly building located at grade on the detector site. A total area of ~700 m^2 will be required for the Far Detector assembly, in addition to the ~7,000 m^2 for the detector and its utilities.

A possible installation plan is as follows: The particleboard arrives by truck pre-cut to size. The scintillator modules arrive in reusable shipping containers. Both of these loads are removed from the truck via Cady-lifting fixture using the bridge crane. Two crewmembers are used to receive materials. A buffer of materials to cover at least 2 weeks of installation work will be stored on site. To minimize construction time the stacks of wood closest to the stack jig will be re-stocked so single sheets are moved less distance.

The stack jig and material storage is as close to the completed detector face as is reasonable. This allows usage of the large building area and minimizes the distance a completed stack is moved. After the stacks are constructed, they are lifted onto the detector face and screwed into place. The completed detector stacks are rigged with a strongback-lifting fixture that has been designed to lift both horizontal and vertical stacks. It uses a vacuum system to hold the stack to the strongback. It then uses a Hillman roller system similar to the MINOS strongback to lift the fixture. Only one fixture is needed for this task.

After the stack is picked up, it is rigged into place with a crane. Once in place, two people (who run tag lines for rigging the stack) use two scissor lifts to move the length of the stack, securing it to the adjacent stack and the previous plane using construction screws delivered by screw driving systems. At the same time, the other member of the team is surveying the unit from one of the scissor lifts. After securing the stack, the crew returns to the location of the next stack. Along the way they will use the surveys from the previous plane to correct it to vertical by attaching wood shims with screws. This operation is repeated 12 times each day to install a plane.

After a plane is installed, some time will elapse before the next steps on that plane, in order to minimize the number of people working in the same physical space. The final installation steps involve two crews of two technicians each. One crew will fill the PVC extrusions with liquid scintillator. The second crew will install the photodetectors and electronics, and cable up the units. Shift physicists then commission the planes.

The construction manpower required for installation (both shifts summed):

2	Receiving team
16	Stack builders (4 crews of 4)
8	Stack installers (2 crews of 4)
4	QA / cablers
4	Scintillator handlers
34	Total installation crew

In addition to the installation staff, an additional 7 support staff (supervision, safety, administration, network, telecommunications and janitorial) are required. Thus, we expect a total staff of 41 full-time people is needed on site for construction of this detector, in addition to the visiting physicists and students, who will do software and systems checkout tasks.

7.9. R&D for the Baseline Design

7.9.1. Overview: The research and development program for the liquid scintillator baseline design is directed towards improving performance, establishing a more precise knowledge of the detector costs and reducing those costs. This plan includes value engineering and prototype testing, in conjunction with an interactive program of simulations. Special attention will given to those ele-

ments of the detector that appear to be cost drivers. We will also seek to identify possible failure modes that cannot easily be remedied. The program will take approximately one year and culminate with the testing of a full scale slice of the detector.

7.9.2: Overall design: As indicated in Section 7.1, we expect to continue to work to optimize the baseline design both in the transverse dimension, that is, the scintillator strip width, and the longitudinal dimension, that is, the amount of passive absorber between active scintillator planes.

As part of this effort, we are investigating an asymptotic longitudinal design with no passive absorber, which we call the Totally Active Scintillator Detector (TASD). Such a detector should have significantly higher efficiency for signal events and better background rejection than the baseline detector. For a cost roughly equal to that of the baseline design, we could build a fully active detector with a total mass of ~25,000 metric tons, that is, half the size of the baseline detector. The two most important research and development questions associated with this design are (a) whether such a detector would better achieve the physics goals of this experiment and (b) how the absence of absorber would affect the mechanical stability of the detector structure. We expect to continue work on both these topics.

7.9.3. Test beam: As described in Chapter 9*,* we plan to study a very small version of the final detector in a test beam, to experimentally determine its response to GeV electrons and pions. This information will be used to check detector Monte Carlo simulations.

7.9.4. Detector Structure: Full size and part size stacks consisting of wood and plastic scintillator modules will be assembled and tested. Individual stacks will be tested for strength, stability and behavior within the expected ranges of temperatures and humidity. Time and motion studies will determine optimal assembly techniques for each stack. Several stacks will be joined to make a partial plane to investigate the effectiveness of the assembly procedure. Time and motion studies of these partial planes will determine a more precise cost estimate for detector assembly. Also addressed by these studies will be the light tightness of the stacks when assembled, their needs for external support, and removal strategies for the end of the lifetime of the experiment. Safety questions of stability, flammability, and liquid containment will also be addressed with prototypes.

7.9.5. Scintillator mixing and delivery: Functional pieces of the liquid scintillator delivery, mixing, and filling system will be tested and refined. Special attention will be paid to the design necessary to eliminate potential leaks and containment if a leak does occur. We will develop and prototype QA apparatus for determining mineral oil and scintillator quality before filling.

7.9.6. Scintillator modules: Time and motion studies of scintillator module assembly will determine the needs for assembly machines and fixtures and provide the basis for more precise cost estimates. Assembled modules will be tested for structural strength and potential mechanical failure modes including liquid and light leaks. Techniques of filling and emptying the modules will be tested to determine their effectiveness. We will also develop techniques for controlling fiber location within tubes to determine if they are a cost-effective way of improving light yield. WLS fiber positioning and light yield will be determined with modules filled with liquid scintillator. Safety tests will help assess potential flammability or liquid containment issues. In addition, accelerated aging tests will check potential interactions of any of the module components with liquid scintillator or with each other. Modified component designs will be produced as needed to minimize costs. Prototype tests will give more accurate light yield parameters that can be used to determine optimal absorber thickness and scintillator cell size.

7.9.7. Photonics: APDs are low gain devices so that attention to their noise characteristics must be an important part of the detector design. Multipixel APDs marketed by Hamamatsu have the gain and noise characteristics that are needed for the detector. To reduce the cost of the photodetector, we plan to use unpackaged APDs for the experiment. The APD must be cooled by an electronic cooling chip (Peltier) that is coupled directly to the rear of the APD. We will work with Hamamatsu to build prototypes of bare multichannel APDs bonded to the cooling chip and mounted on a circuit board that connects the APD to the amplifier and other electronics. Care must also be taken in the design of the fiber/APD interface that may also be fabricated by Hamamatsu or at one of the collaborating institutions.

Since wavelength shifting fiber is a cost driver for this detector, the cost of the detector is a sensitive function of fiber diameter. The entire photon production chain will be examined to determine if we can reliably increase the photon yield into the APD or decrease the electronics noise. Either modification will allow cost reduction by decreasing the fiber diameter.

7.9.8. APD box and WLS system design: The design of the ~9,000 APD boxes that provide the interface between the fibers, the APD, and the electronics is one of the most complex parts of the detector. Careful design and prototyping is essential to containing detector costs. The box design must be light tight, efficiently remove heat from the Peltier coolers and protect cold surfaces from moist air. Other elements for mechanical design are insertion methods for the WLS fiber, the manifold that aggregates the WLS fibers en route to the APD box, the WLS fiber to APD box optical connector and the APD printed circuit board mounting.

7.9.9. Electronics: The low gain of the APD puts a premium on low noise electronics. We will produce and test modifications of the existing MASDA design to establish a baseline on which to base a custom designed ASIC. Prototypes of the entire circuit board with all components will be tested to optimize layout for the lowest noise. Several noise reduction circuits using multiple sampling will be prototyped and compared.

Chapter 7 References

[1] P. Border, *et al., "*A large liquid scintillator detector for a long baseline neutrino oscillation experiment," Nucl. Instrum. Meth. A 463 (2001) 194-204; L. Benussi, *et al.*, "Large liquid-scintillator trackers for neutrino experiments," Nucl. Inst. Meth. A 488 (2002) 503-516.

[2] BC517L Material Safety Data Sheet (MSDS), www.bicron.com.

[3] M. Doucet, *et al*., "Light yield measurements in a liquid scintillator detector with wavelength shifting fibre readout," Nucl. Instrum. Meth. A 459 (2001) 459-468; M. Moszynski, *et al*., "Avalanche photodiodes in scintillation detection," Nucl. Instrum. Meth. A 497 (2003) 226-233; D. Renker, *et al*., "Properties of avalanche photodiodes for applications in high energy physics, astrophysics and medical imaging," Nucl. Instrum. Meth. A 486 (2002) 164-169.

[4] K. Deiters, *et al.,* Nucl. Instrum. Meth. A 461 (2001) 574-576; Nucl. Instrum. Meth. A 453 (2000) 223-226; Nucl. Instrum Meth. A442 (2000) 193-197.

[5] A good summary of APD theory, including noise, is given in the CMS ECAL TDR, CERN report CERN/LHCC 97-33.

[6] M. Maolinbay, *et al*., "Design and performance of a low noise, 128 channel ASIC preamplifier for readout of active matrix flat panel imaging arrays," NIM A 485 (2002) 661-675.

[7] T. Zimmerman, "The MASDA-X chip – a new multi-channel ASIC for readout of pixilated amorphous silicon arrays," Fermilab technical note FERMILAB-TM-2063 (1998).

[8] R. Yarema, *et al*., "A programmable, low-noise, multi-channel ASIC for readout of pixelated amorphous silicon arrays," presented at the 8th European Symposium of Radiation Detectors, Sloss Elmau, Germany, June 14-17, 1998 (submitted to NIM).

8. Simulations

8.1. Introduction

This chapter describes the simulation methods that have been used to design and verify the performance of the proposed liquid scintillator detector. The main simulation described is for a far detector site 10 km off axis with a beam length of 810 km. This off-axis location is optimal for this beam length and $\Delta m_{32}^2 = 0.0025$ eV^2. However, the performance of the experiment is not strongly dependent on the off-axis position and other considerations may suggest alternative off-axis distances. The simulation assumes $\nu_\mu \rightarrow \nu_e$ oscillations at $\sin^2 2\theta_{13} = 0.1$, somewhat below the CHOOZ limit of $\sin^2 2\theta_{13} = 0.14$ at $\Delta m_{32}^2 = 0.0025$ eV^2.

The code is based on the tested simulation software of the MINOS experiment (GMINOS) using GEANT3 and the NEUGEN3 neutrino interaction generator. This allows the efficient use of some of the tools that have been developed for implementing and analyzing a scintillator detector.

The detailed methodology of the event generation and reconstruction is described below. ν_e events are separated from background by a succession of cuts and by a likelihood analysis. Finally, a figure of merit (FOM1) equal to the number of signal events divided by the square root of the number of background events is calculated.

8.2. Detector Definition

8.2.1. Detector geometry: The simulated detector consisted mainly of passive absorber, modeled as Lucite with a density of 0.7. The active elements were scintillator strips with the dimensions given in Table 7.3. The external and internal walls of the scintillator modules were fully simulated. Half the strips were oriented along the *x*-axis, and half along the *y*-axis. The horizontal *x*-strips were two separate strips with readout at the sides of the detector; the vertical *y*-strips were single strips with readout at the top. The constraints of the GMINOS system required some minor deviations from the exact form of the detector but the overall outcome was very close to that described in Chapter 7. More details of the geometrical layout actually simulated are given in Reference [1].

8.2.2. Readout simulation: The light collection and transmission in the fiber was simulated using the code for the MINOS light collection. The looped fiber was approximated by assuming MINOS style single-ended readout with an average of 35 photoelectrons collected from a minimum ionizing particle crossing the far end. The attenuation measured for the looped configuration, described in Chapter 7, was used. A WLS fiber tail of length 1 m between the end of the scintillator extrusion and the photodetector was assumed. The photodetector was modeled as an APD with a quantum efficiency of 85%. The parameters of the APD gain and noise given in Chapter 7 were used to smear the APD output. The generated pulse height distribution for minimum ionizing, normally incident, particles as a function of distance along the strip is shown in Fig. 8.1 and the pulse height distribution as a function of the number of particles crossing the strip in Fig. 8.2. A threshold of 20 photoelectrons was imposed in the subsequent analysis.

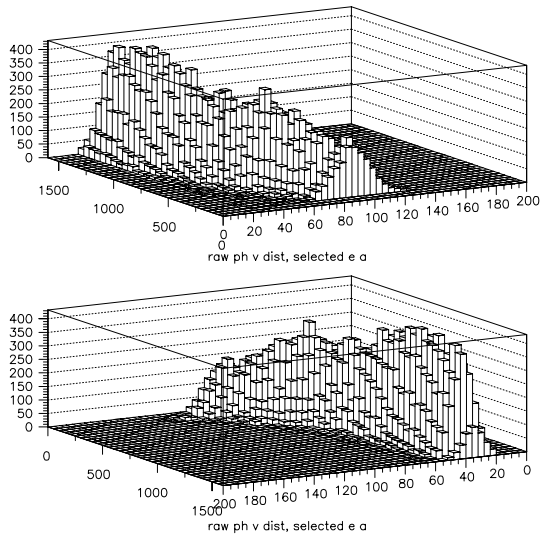

Fig. 8.1: Pulse height as a function of distance along a strip for hits that correspond to the energy deposit of a normally incident minimum ionizing particle, viewed from the APD end (top) and far end (bottom).

8.3. Event Generation

Interactions were simulated spanning the range of energies, neutrino types and interactions. The neutrino interactions were chosen with a 1/E

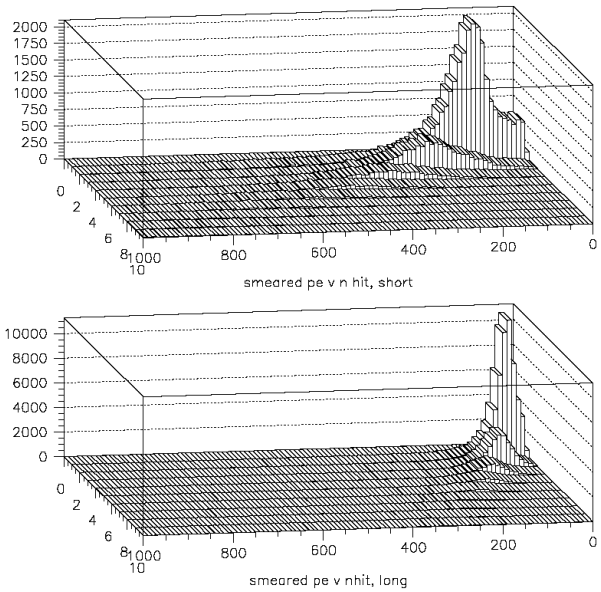

Fig. 8.2: Pulse height distributions as a function of number of particles crossing a strip at the APD end (top) and the far end (bottom). These distributions are for all hits generated by ν_e charged current events.

neutrino energy distribution so that the interacted neutrino spectrum is approximately flat. Initial tests showed that selected ν_μ and ν_e charged current events had incident neutrino energies below 6 GeV. Neutral current events had contributions from beam energies up to 20 GeV. Neutral current events were generated separately from the charged current events to give the required statistics on the predominant background. Two samples of events were generated, one as a training sample for the event cuts and one as a test sample. Approximately 300,000 ν_μ charged current, 100,000 ν_e charged current and 500,000 neutral current events were generated for each sample.

8.4. Event Reconstruction

A loose clustering algorithm was applied to the events, which grouped together hits in each view that occur within a distance of 2 m of each other. Clusters in the two views were matched by the correspondence of their start and end positions in z (along the beam). The matched cluster with the largest number of hits was selected as the event. The large majority of events only produced one matched cluster. Events with no matched clusters were rejected. In addition the event was required to have a minimum of three hits in each view. The clustering removed outlying hits from events and rejected low energy (chiefly neutral current) events.

Events with more than two hits outside the fiducial volume of the detector (closer to an outside face than 50 cm in x or y, or 2 m in z) were rejected at this stage, 86% of reconstructed ν_e events (77% of total events) passed this fiducial requirement.

A straight line was fit to the cluster in each view. The measured pulse height was corrected for attenuation using the information on the position along the strip given by the fit. The hit and pulse height residuals to the straight line and the rms of the hit and pulse height distributions in the beam direction were calculated in each view. These and the other quantities used in the following analyses were summed over both views to apply to the full event.

The event cluster was then passed through a filter, which used the Hough Transform to select the most significant track-like segment of the event. This filter is an iterative procedure where the 2-dimensional hits (x_i,y_i) in each view belonging to the cluster are transformed into trajectories in the parameter space (θ,d) where the relation $x_i \cos\theta + y_i \sin\theta - d = 0$ is asserted. The parameters of the most significant track-like segment of the event were taken to be those where the peak in (θ,d) space occurs, and the hits belonging to the track were those whose trajectories passed within a preset minimum distance to this peak. The procedure was repeated with finer binning in (θ,d) space and more stringent cuts on the minimum distance to the peak. Fig. 8.3 illustrates the effect of the filter for sample ν_μ CC, NC and ν_e CC events. In this implementation, electron showers tend to be sufficiently narrow that most of the shower hits were included in the track-like object, whereas fewer hits were tagged as track-like for NC showers, which are generally more diffuse. A straight line was fit to the hits assigned to the Hough track in each view and again the transverse residual and longitudinal rms calculated. A set of ntuples was produced which was used in the following analysis to select ν_e events.

8.5. Event Weighting

As described above, the events were generated flat in energy. In order to represent the expected event distributions in the detector they were weighted by the following factors:

- The beam neutrino energy distributions for a location 10 km off axis and 810 km from Fermilab, using the medium energy NuMI beam configuration.
- The oscillation probability, for $\nu_\mu \rightarrow \nu_\mu$ with $\sin^2 2\theta_{23} = 1.0$ and $\Delta m_{32}^2 = 2.5 \times 10^{-3}$ (eV/c)^2, and for $\nu_\mu \rightarrow \nu_e$ with $\sin^2 2\theta_{13} = 0.1$.
- For the NC events, the NC/CC ratio as a function of energy.

This calculation does not include any matter effects, which depend on the unknown mass hierarchy, nor any CP violation which depends on the unknown phase parameter, δ. The potential effects of these parameters are discussed in Chapters 3 and 5.

The events were finally normalized to the expected rate of ν_μ CC events in a 5-year exposure of a 50-kiloton detector with 4 x 10^{20} protons on target per year. The numbers of events in the four classes, ν_μ CC, NC, ν_e CC from the beam and ν_e CC oscillated from ν_μ are given in Table 8.1 and shown in Fig. 8.4

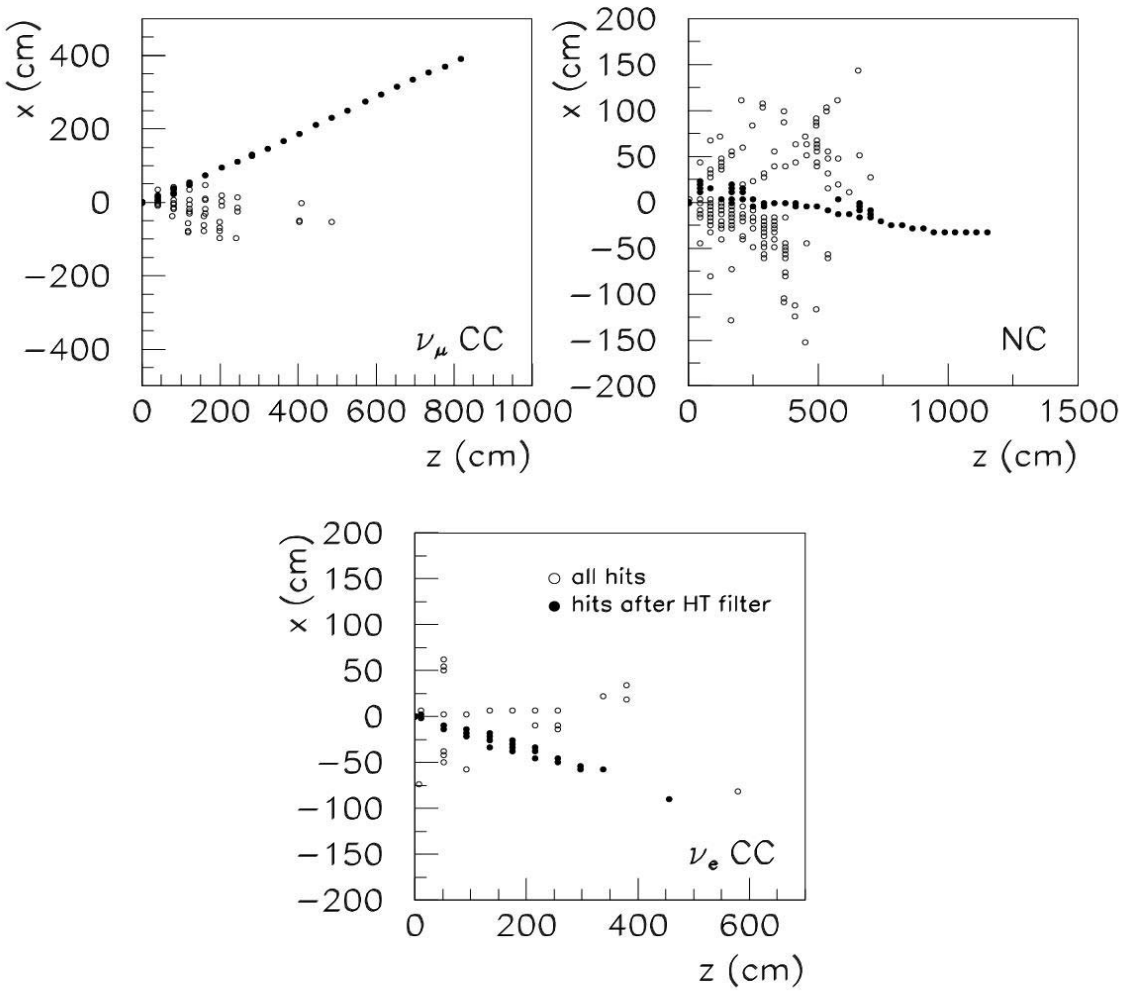

Fig. 8.3: Use of the Hough Transform filter on three example events. The open circles show all the hits in the event and the filled circles show the hits that remain after the filter is applied.

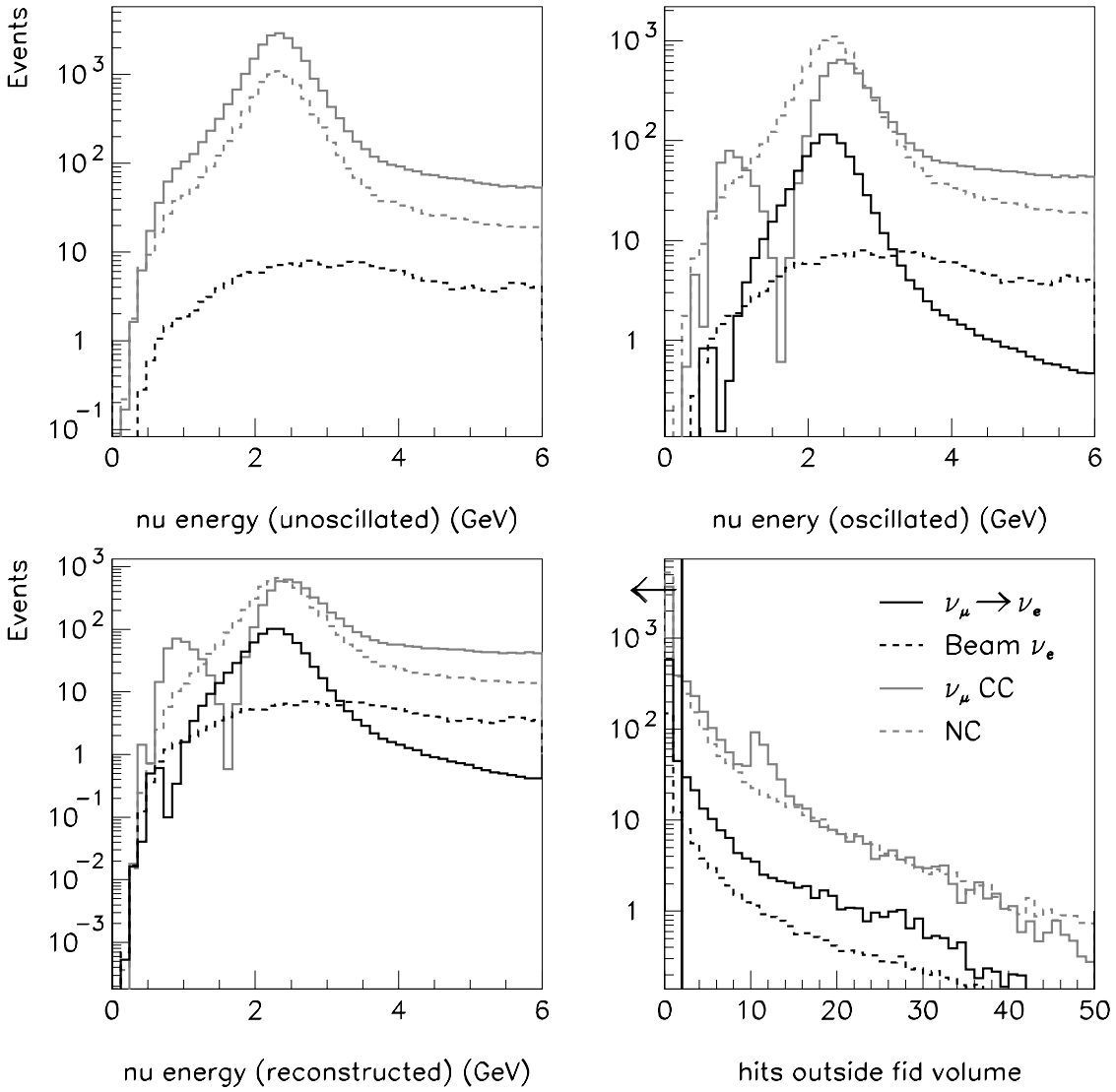

Fig. 8.4: Event samples used in this analysis. Top left: unoscillated true neutrino beam energy distributions for events that leave hits in the detector. Top right: energy distributions after oscillations. Bottom left: energy distributions for events that form a valid cluster. Bottom right: distributions of numbers of hits outside the fiducial volume of the detector. Events with more than 2 hits outside the fiducial volume are rejected.

8.6. Selection of ν_e CC Events

The selection process was in two stages. Firstly a set of cuts was applied which rejected background events with as small as possible effect on the ν_e CC events. The background events remaining after these cuts have a strong overlap with the desired sample. Further separation was obtained by forming a likelihood ratio using a number of variables and cutting on this ratio.

The initial cuts are applied consecutively on the variables shown in Figs. 8.5 and 8.6 and are:

- 200 cm < event length < 800 cm (rejects long muon tracks and short NC events)
- 8000 pe < total pulse height < 18000 pe (rejects low-y NC and high energy ν_e CC events)

- Number of hits in the track found by the Hough transform analysis > 3 (ensures that a Hough track was found)
- fraction of event hits in the Hough track > 0.75 (preferentially selects low-y ν_e CC events)
- hits/plane on the Hough track > 1.5 (selects showering events)
- cosine of the angle between the Hough track and the beam > 0.80 (rejects poorly reconstructed and high-q^2 events)

The weighted number of events remaining after each cut is shown in Table 8.1.

Cut	ν_μ CC	NC	Beam ν_e	$\nu_\mu \rightarrow \nu_e$ Signal
Beam unoscillated	22858	10594	229	
Beam oscillated	5758	10593	229	853
Reconstructed	5501	6681	202	757
Fiducial cut	4410	5950	170	653
Event length	1755	4343	143	593
Pulse height	1226	1327	67.0	508
Hough planes	1120	1043	62.0	474
Hough fraction	150	76.8	27.4	229
Hough hits/plane	20.1	56.0	26.7	223
Beam angle	11.4	50.6	26.0	218
Likelihood cut	3.6	15.4	19.1	175
Efficiency	$6.3\ 10^{-4}$	$1.5\ 10^{-3}$	$8.3\ 10^{-2}$	0.21

Table 8.1: Breakdown of the weighted number of events remaining after the successive cuts.

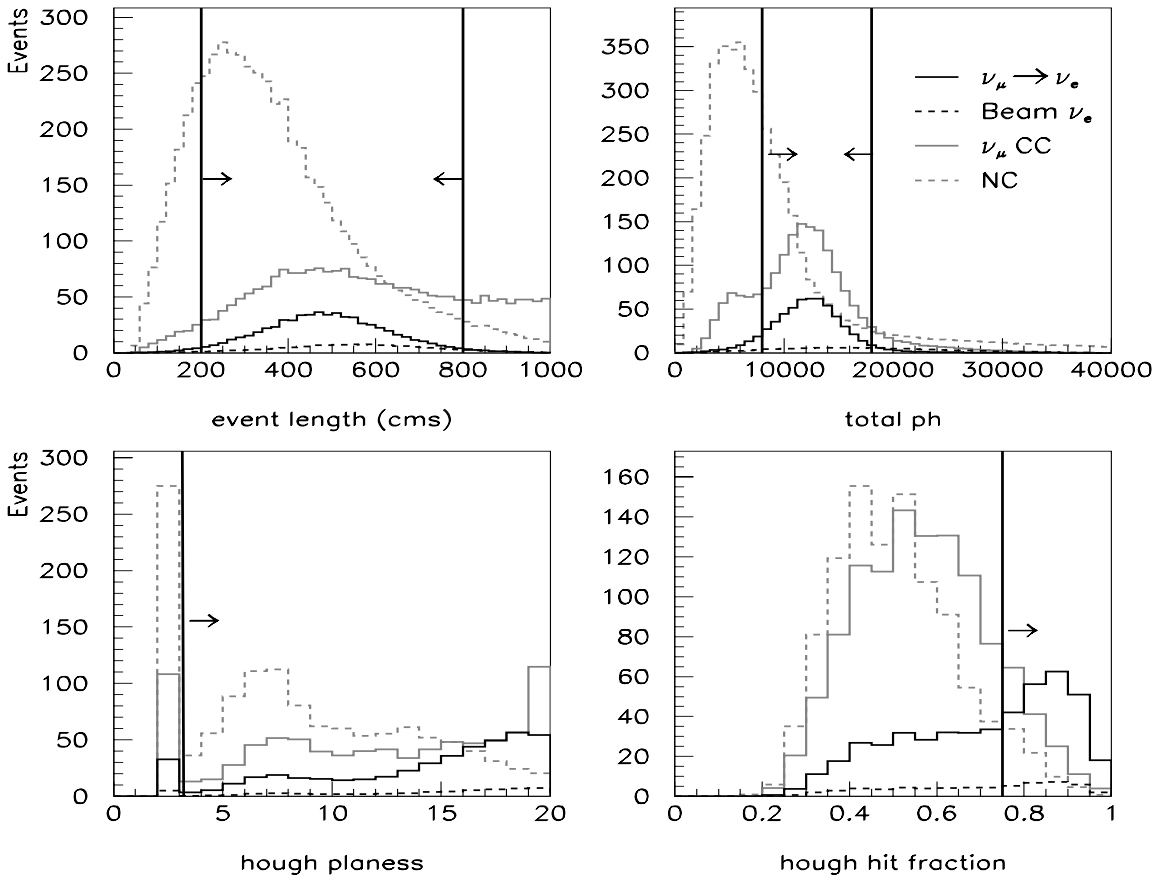

Fig. 8.5: Event distributions used for the cuts. The vertical lines define the cuts The cuts are performed sequentially in the following order. Top left; event length. Top right; summed pulse height. Bottom left; the number of planes in the Hough Transform track. Bottom right; the fraction of hits in the Hough Transform track.

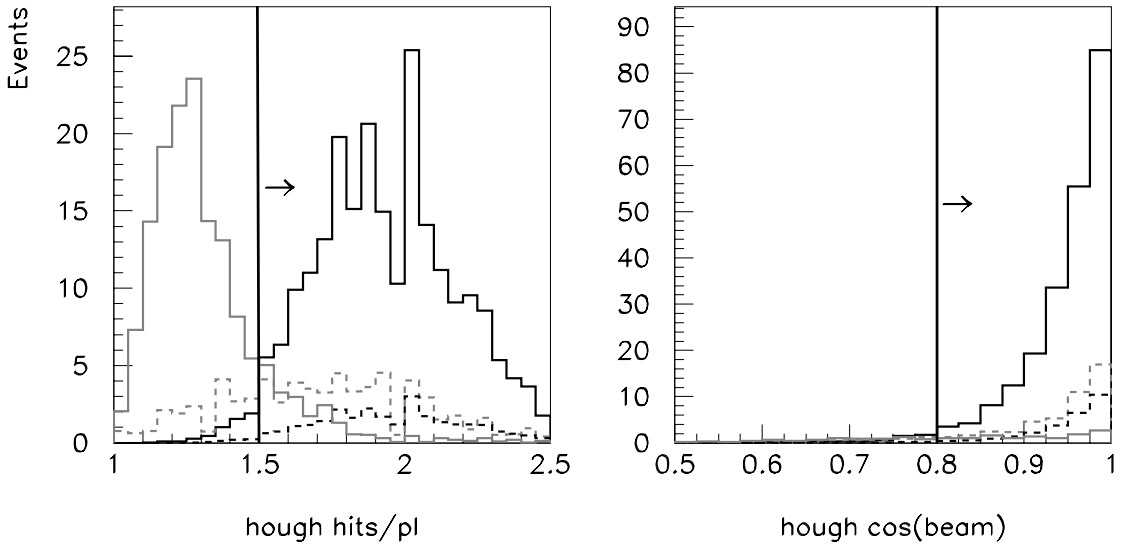

Fig. 8.6: Left; the number of hits per plane in the Hough Transform track. Right; the cosine of the angle between the Hough track direction and the z-axis.

A likelihood analysis was then performed on the remaining events. One or two-dimensional histograms of the variables in the following list were constructed for each of the event types and normalized to a total of 1.0. This then served to define a probability for any given event that it came from any of the samples. A total likelihood for any sample was found by multiplying all of the probabilities. Three log likelihood ratios between the oscillated ν_e hypothesis and the other three hypotheses were formed and plotted. Finally cuts were applied to these ratios to define the final ν_e sample.

The following one dimensional and two dimensional probabilities were used in the likelihood analysis:

- the event length
- the maximum gap (i.e. contiguous planes with no hits) in the event
- the number of detector planes in the event
- the transverse pulse height residual
- the Hough track hit fraction
- the Hough track hits per plane
- the Hough track pulse height
- the cosine of the angle between the Hough track and the beam
- the transverse pulse height weighted residual versus the pulse height in the Hough track
- total pulse height versus pulse height weighted transverse residual
- cosine of the angle between the Hough track and the beam versus total pulse height
- longitudinal rms of the pulse height versus total pulse height

For those parameters that have already been used for the cuts, the events remaining after the cuts were used to define the likelihood function. The log likelihood ratios are shown in Fig. 8.7.

There is quite good discrimination between ν_e signal events and neutral current and charged-current backgrounds. There is less separation between ν_e signal events and beam ν_e background; here the only discrimination is that the beam ν_e events tend to be of higher energy than the $\nu_\mu \rightarrow \nu_e$ signal.

The following cuts on the likelihood ratios define the sample of ν_e events in this analysis:
$\log L_{e/\mu} > -2$,
$\log L_{e/NC} > -2$,
$\log L_{e/ebeam} > -5$

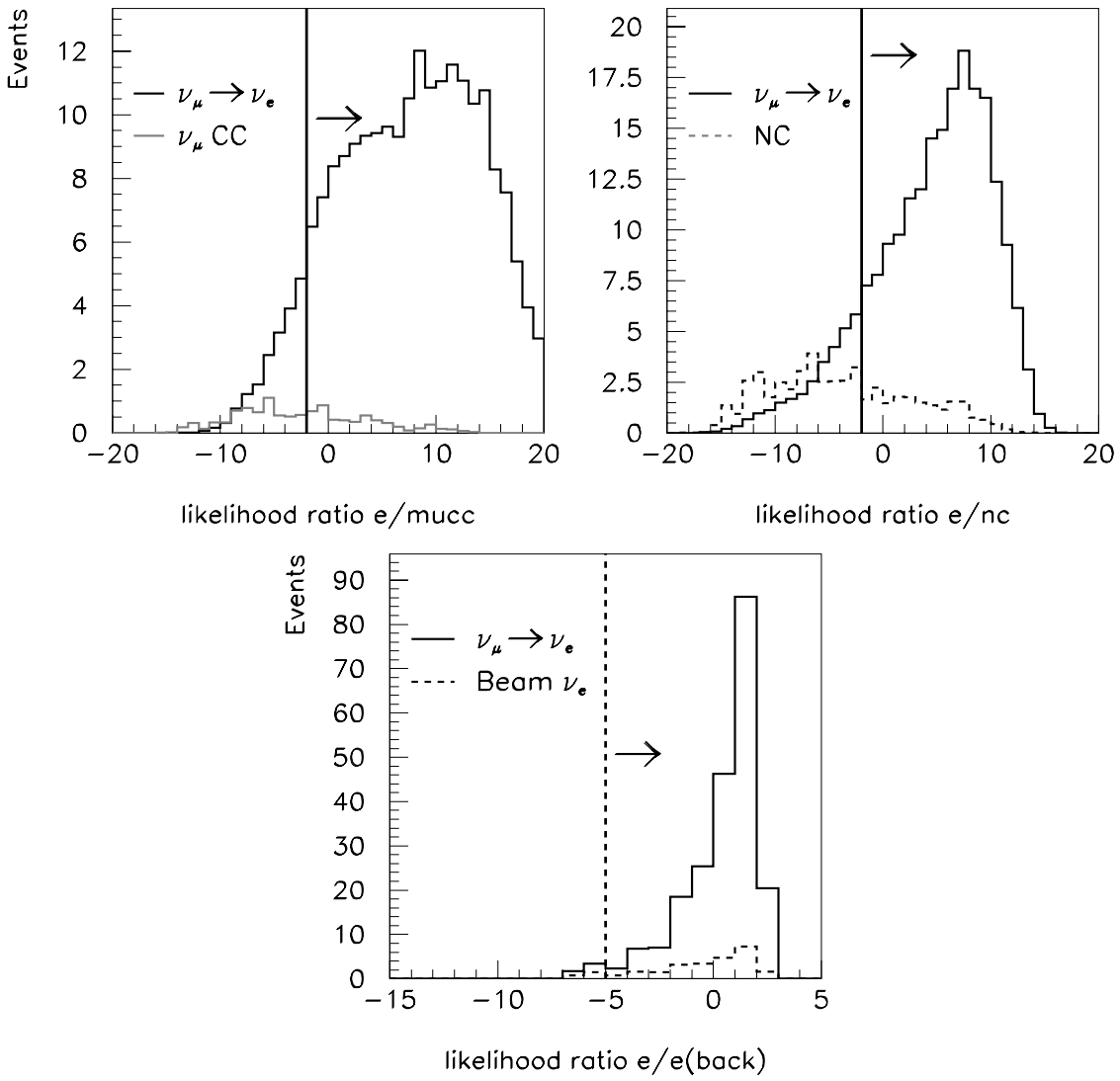

Fig. 8.7: Top left: log of the ratio of the probabilities of the ν_e CC to oscillated ν_μ CC hypotheses. Top right; log of the ratio of the oscillated ν_e CC to the NC likelihood. Bottom; log of the ratio of the oscillated ν_e CC to the beam ν_e CC likelihood.

All the cuts were optimized using the first of the two event samples, and were selected in order to maximize the Figure of Merit (FOM1). The numbers given below and in Table 8.1, show the result of applying the selection cuts to the second, independent, sample of events.

Defining the figure of merit as the number of $\nu_\mu \rightarrow \nu_e$ signal events divided by the square root of the total number of background (ν_μCC, NC and beam ν_e) events, the following results are obtained:

- signal = 175.2±1.8 events
- background = 38.1±1.5 events
- figure of merit = 28.4±0.6
- oscillated ν_e efficiency = 20.5%
- ν_μ CC rejection = 6.3×10^{-4}
- NC rejection = 1.5×10^{-3}
- beam ν_e CC rejection = 8.3×10^{-2}

The quoted errors are the errors on the numbers due to the finite statistics of the Monte Carlo, not the expected errors from any given experiment.

Using these cuts, the background due to misidentified ν_μCC and NC events is reduced to the same level as the intrinsic beam ν_e background. More stringent cuts can further reduce this background at the expense of signal. However it is difficult to reduce the beam background much further, since the only difference between beam ν_e and signal $\nu_\mu \rightarrow \nu_e$ events is the energy distribution, and this is already taken into account by including the total pulse height distributions in the cuts and likelihood analysis. The FOM1 thus does not significantly improve with harder cuts.

We have investigated a large number of alternative cuts and compositions of the likelihood function in attempts to improve the figure of merit. Adding further quantities and combinations of quantities gave little improvement, in fact frequently gave a small reduction, in the FOM1. The cuts were changed to remove more background before the likelihood analysis but after optimization of the likelihood very similar FOM1 were obtained. The changes mostly spread out the likelihood function but do not alter the fraction of background that lies under the signal. Further small reductions in the background with an enhanced signal efficiency may be obtainable by more sophisticated pattern recognition, in particular by identifying more individual tracks in the event. However, it is not expected that this will raise the figure of merit by large amounts.

To first order the effect of the analysis is to select quasi-elastic or low-*y* ν_e charged current events, which consist mainly of a single showering track. The selection efficiency of such events is high. Scanning the selected background events showed that they closely resembled this topology, either because of the presence of a high-energy gamma or because the superposition of charged and showering tracks resembled a single showering track.

8.7. Other Simulations

8.7.1. Alternative Figure of Merit: The Figure of Merit (FOM1) is quite insensitive to the cuts over a fairly wide range. Harder cuts give fewer events and less background, softer cuts the reverse. Analyses searching for a signal require the maximum value of FOM1. However other analyses, for example those measuring parameter values, may be more sensitive with more events and more background. The relevant function is then an alternative Figure of Merit (FOM2), which is the ratio of the signal to the square root of the signal plus background. In general this has a maximum for softer cuts with larger signal and more background. However, at the maximum of FOM2 the value of FOM1 is only about 1.0 below its maximum value. The above analysis is maximized for a search experiment using FOM1.

8.7.2. Other off-axis positions: The analysis has been repeated for other off-axis positions using the same primary beam. The results are given in Table 8.2. As one goes further from the beam axis the beam flux and the peak energy decrease. The convolution of beam and oscillation function increases and thus the signal increases with decreasing off-axis distance. However the background also increases at smaller distances because of the increase in the higher energy flux and the decrease in the suppression of charged current events by oscillation. 10 km off-axis is an optimum position under the conditions of this simulation but larger off-axis positions could be preferable for the observation of the matter and CP violating effects described in Chapter 3.

Position/Type	Signal	Background	FOM1
8km, ν	228	68	27.5
10km, ν	175	38	28.4
12km, ν	123	24	25.0
14km, ν	89	21	19.5
10km, ν, matter	208	39	33.4
10km, anti-ν	66	22	14.1
10km,ν,Δm^2=0.002	134	42	20.8
10km, ν, RPC	132	27	25.4

Table 8.2: The signal, background and FOM1 of simulations under various different conditions. The first 4 rows are for the main simulation described in this section for different off-axis positions. The fifth row includes matter effects for the normal hierarchy. The sixth row is the simulation for the anti-neutrino beam. The seventh row has a lower value of Δm_{32}^2=0.002 eV^2 and the eighth row is for the RPC simulation. The event selection parameters have been reoptimized for each condition.

8.7.3. Matter effects: Matter effects are significant at these distances and energies and the discussion of this experiment's scientific potential in Chapter 5 includes matter effects and CP violation. If matter effects with a positive Δm_{32}^2 (normal hierarchy) are included in the simulation at 10 km off-axis, the signal rises to 208 events while the background stays essentially constant. This results in a figure of merit (FOM1) of 33.4.

8.7.4. Anti-neutrino beam: A similar analysis has been carried out for the anti-neutrino beam. In this case the contamination of neutrinos in the beam is significant and has been included. The anti-neutrino flux is lower than the neutrino flux but the event selection efficiency is somewhat higher due to the different y distributions of the events. The results for a 250 kT-year exposure, the same as for the neutrino beam, are given in table 8.2

8.7.5. Lower Δm^2: The allowed value of Δm_{32}^2 from the SuperKamiokande analyses still covers a wide range. In general the sensitivity of this experiment decreases as Δm_{32}^2 moves lower, because the peak in the oscillated spectrum moves to lower energies where the beam flux is falling off. To calibrate the changes expected if Δm^2 changes, the simulation has been run for a Δm_{32}^2 of 0.002 eV^2. The results are given in table 8.2. It can be seen that the background remains approximately constant but the signal is reduced by 23%.

8.7.6. Light level: In order to test the sensitivity to the light level a simulation with 25% less light was carried out. The event selection is not expected to be very critical on the light level since the assumed 35 pe collected at the far end of a strip is well above the threshold of 20 pe. Also the event selection is not strongly dependent on the presence or absence of individual hits. In fact the simulation with 25% less light gave no statistically significant change in the signal efficiency, background rejection or figure of merit after reoptimization of the cuts.

8.7.7. RPC simulation: A similar analysis has been carried out for the RPC based detector. A realistic simulation of the 2-dimensional readout detector described in the Appendix has been produced. A similar cut and likelihood analysis to that described in section 8.6 was performed. The results at 10 km off-axis are given in Table 8.2. An RPC detector has the advantage that two-dimensional readout is available in each sensitive gap compared to the one-dimensional readout of the scintillator detector. On the other hand the scintillator detector measures pulse height and is sensitive to the number of particles crossing the sensitive region and their deposited energy, whereas the RPC readout is digital. It is an important goal of the simulations to quantify the relative gain of each case. To do this the simulations must be comparable in all respects other than the ones to be tested. This has not yet been demonstrated with the present simulations but will be done on the time scale of the final technology decision.

8.8. Other Physics

The events generated for the $\nu_\mu \rightarrow \nu_e$ analysis have been used to test this experiment's sensitivity to the quantities, Δm_{32}^2, $\sin^2 2\theta_{23}$ and the possible fraction of sterile neutrinos. The analysis has been carried out at off-axis locations of 12 km and 10 km. The results are better at 12 km off-axis because the oscillation dip is more centered in the beam peak. It is these that are quoted here. The 10 km off-axis results are given in Reference [2]. A likelihood analysis using similar quantities to those of the ν_e analysis was carried out to separate CC and NC events. Figure 8.8 shows the CC/NC likelihood ratio. CC-like and NC-like event samples were selected as shown in the figure. The CC-like sample had a selection efficiency of 82% for true CC events and a 7% contamination of NC events. The NC-like sample had a selection efficiency of 58% and a contamination of 42%.

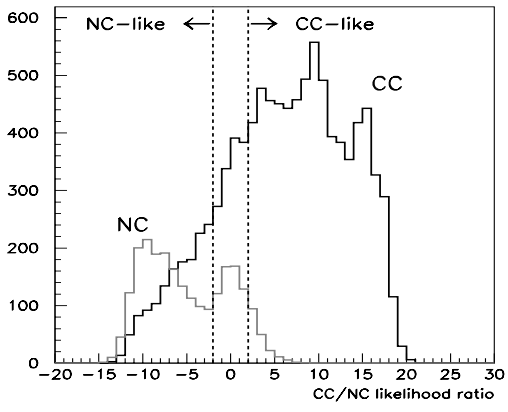

Fig. 8.8: Likelihood ratio distributions for true CC and NC events. The cuts used to define CC-like and NC-like samples are indicated by the two dashed lines.

8.8.1. Measurement of oscillation parameters: The resultant measured energy distribution of CC-like events for oscillation parameters, Δm_{32}^2=0.0025 eV^2 and $\sin^2 2\theta_{23}$=0.95, was fitted to determine the best measured values of the parameters. The same five year exposure as for the ν_e appearance experiment was assumed and systematic errors on the neutrino energy scale, overall flux normalization and the NC cross-section were included. The left hand plot in Figure 8.9 shows the 90% confidence level contour with and without systematic errors and the right hand plot the one dimensional $\Delta\chi^2$ contour for $\sin^2 2\theta_{23}$. It can be seen that if these were the oscillation parameters, it would be possible to exclude maximal mixing ($\sin^2 2\theta_{23}$=1.0) at greater than 99% confidence level and significantly improve the determination of $\sin^2 2\theta_{23}$.

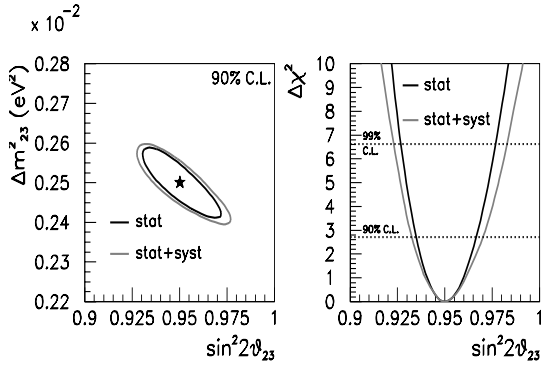

Fig. 8.9: Errors from this analysis on the parameters Δm_{32}^2 and $\sin^2 2\theta_{23}$. The input values are given by the star.

8.8.2. Limits on sterile neutrinos: The signal for $\nu_\mu \rightarrow \nu_s$ oscillations is a depletion in the number of observed neutral current events compared with the expectation if the neutral current events are unaffected by oscillations. A simultaneous fit was performed to the CC-like and NC-like energy distributions with the normal parameters Δm^2 and $\sin^2 2\theta_{23}$ augmented with an additional parameter $\sin^2 2\theta_{\mu s}$, the amplitude for $\nu_\mu \rightarrow \nu_s$ oscillations. It was assumed that the sum of active and sterile oscillations was unity and that the active and sterile neutrinos oscillated with the same value of Δm^2. Figure 8.10 shows the results of a fit assuming Δm^2=0.0025 eV^2 and $\sin^2 2\theta_{\mu s}$=0.0. The left hand plot shows the two-dimensional contours assuming just statistical errors and statistical plus systematic errors. The right hand plot shows the $\Delta\chi^2$ curve for $\sin^2 2\theta_{\mu s}$.

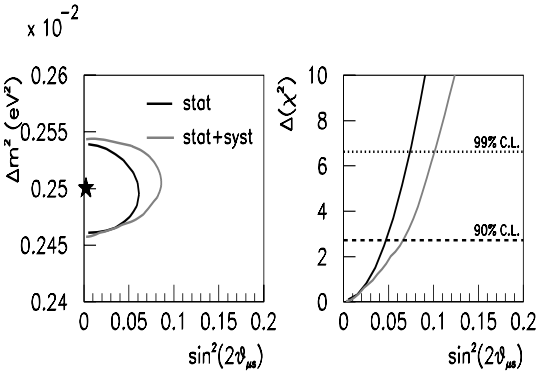

Fig. 8.10: 90% confidence allowed region in the Δm_{32}^2,$\sin^2 2\theta_{\mu s}$ plane. The input values are shown by the star. The right hand plot shows the one dimensional projection of the $\Delta\chi^2$ surface.

It can be seen that 90% confidence limits of 0.07 can be set on the fraction of sterile neutrinos, including both statistical and systematic errors. More details of these analyses can be found in Reference [2].

Chapter 8 References

[1] Peter Litchfield, Leon Mualem, David Petyt, "Simulation of a Solid Scintillator Off-axis Detector," Off-axis-Note-SIM-23 (2003). The liquid scintillator layout was the same apart from the active element dimensions.

[2] David Petyt, "Other oscillation measurements in the off-axis detector," Off-axis-Note-SIM-32 (2004).

9. Neutrino Beam Backgrounds, Systematic Studies and the Near Detector

9.1. Introduction

In this chapter, we discuss the systematic uncertainties related to the NuMI neutrino beam and to detector response. We plan to make use of measurements in the NOνA Near Detector and in test-beam studies with a Calibration Detector to calculate corrections for these systematic effects. We will also use measurements made by the MIPP, MINOS and MINERνA experiments to reduce systematic uncertainties and improve our sensitivity to electron-neutrino appearance. At the end of this chapter, we propose a program of test-beam measurements to determine the absolute and relative responses and energy calibrations of the NOνA Near and Far Detectors.

There are two general categories of backgrounds in NOνA: those that originate from the neutrino beam itself and those that originate from cosmic-ray events that occur within the neutrino-beam time window. Chapter 8 has already described the simulation and analysis of beam-related backgrounds. The current chapter discusses how their levels in the far detector can be determined using measurements in one or more near detectors and what this implies for the near-detector design. Chapter 10 describes the cosmic-ray background sources and their expected magnitudes, which must be well below the beam-induced backgrounds to achieve the best physics sensitivity.

9.2. Near Detector Requirements

The primary near-detector design requirement is that it should be as similar as possible to the far detector in material and segmentation. This requirement ensures that the efficiencies for signal and background events are nearly identical. To predict the backgrounds at the far detector we also need to consider the differences between the neutrino beam spectra at the near and far locations. Differences in background levels will result from the different energy dependence of different neutrino interaction processes. Therefore, errors on the background prediction will come primarily from flux and exclusive-channel cross section uncertainties. If there were only one kind of background, if all neutrino scattering processes had the same cross section as a function of energy, and if their differential distributions did not change with energy, then the far to near ratio for the background would be robust and uncertainties in the absolute flux and cross section would completely cancel. However, this is clearly not the case, although some uncertainties will cancel in the ratios of near and far measurements. To keep the background uncertainties low it is important to optimize both the location and design of the near detector and also to take advantage of measurements by other experiments running in the NuMI beamline.

9.3. Near Detector Location and Design

In this section we compare the neutrino beam spectra at several possible near detector locations with those at the far detector "baseline" site. As described in Chapter 11, this site is assumed to be at Ash River, Minnesota, 810 km from Fermilab and 10 km off the NuMI beam axis. Given the forthcoming hadron production measurements of the MIPP experiment using the NuMI target, the uncertainties on the ratios of the fluxes between the near and far detectors are expected to be at the few percent level. The largest remaining uncertainties will be due to the uncertainties in the total and differential cross sections of channels that produce background events. We consider these processes and the resulting uncertainties on the far detector prediction for different near detector locations.

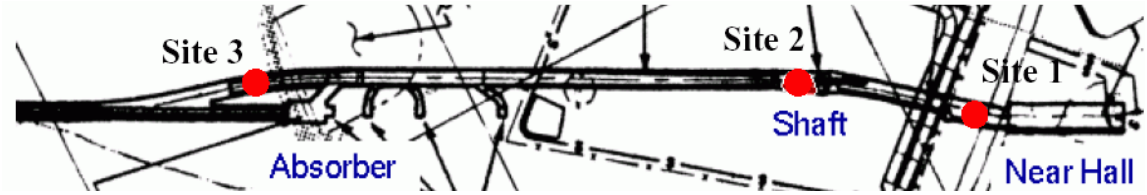

Fig. 9.1: The NuMI access tunnel upstream of the MINOS near detector hall. The beam direction is from left to right. The off-axis angles are: Site 1 - 4 mrad; Site 2 - 21 mrad; Site 3 - 16 mrad. Off-axis angles are measured from the average pion decay location, 200 m downstream of Horn 1.

9.3.1. Possible NOvA Near Detector Sites: The NuMI tunnels have several sites that could accommodate a near detector of similar construction to the far detector. Fig. 9.1 shows the layout of the MINOS near-detector hall access tunnel. Starting at the Absorber Hall, on the left side of the figure, the tunnel makes a sharp turn to the west just downstream of the absorber. It continues parallel to the neutrino beam direction at a distance of ~14 meters from the beam axis for a distance of ~250 meters. Then it bends back east to enter the MINOS near detector hall, which is on the beam axis. This access tunnel geometry makes a wide range of off-axis angles accessible for an off-axis near detector. Fig. 9.1 indicates three possible locations for a near detector: just upstream of the MINOS near detector (Site 1), just upstream of the NuMI access shaft (Site 2), and a third location just down stream of the NuMI hadron absorber (Site 3). The transverse dimensions of the NuMI tunnels in all these locations are similar to those of Site 2, shown in Fig. 9.2. Each location provides ~3.5 meters of useable width (allowing ~1 meter for a walkway), and ~5.0 meters of usable height.

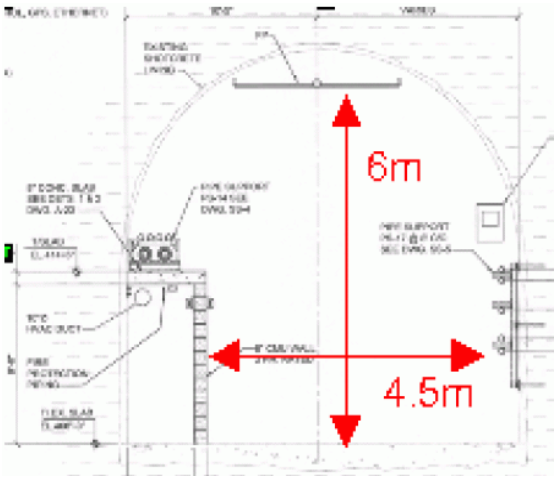

Fig. 9.2: A cross-section view of the access tunnel near Site 2 (see Fig. 9.1).

Downstream locations have the advantage of minimizing the neutron and rock-muon rates. The larger off-axis angles of upstream locations, because of the reduced rates there, minimize the event overlap problem. Given the range of sites available, one can attempt to optimize the near detector location to minimize differences in the neutrino flux at the near and far detector locations.

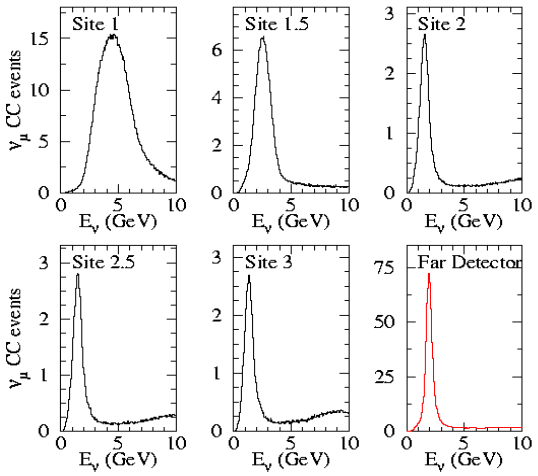

Fig. 9.3: Muon-neutrino event spectra at several different near detector locations (see Fig. 9.1).

Fig. 9.3 shows the muon neutrino event rates for several locations in the NuMI halls, where the sites labeled "1.5" and "2.5" are located midway between the Sites 1, 2, and 3 as shown in Fig. 9.1. There are two main differences between the spectra at these sites and the spectrum at the far detector. The peak is broader at the near site than at the far site, and the "high energy tail" is a larger fraction of the total event sample in the near detector. The energy spectrum is widened at the near detector because there is a broad range of decay positions of the parent pions, so there is no single "off axis angle" that one detector sees. At the far detector, the hundred-meter range of decay locations has a negligible effect on the off-axis angle. At the near detector, the high-energy tail is fractionally higher because these events come from the high-energy pions that decay farthest downstream in the decay pipe. Those decays are significantly closer to the near detector than the decays of the pions that give events in the peak of the distribution. At the far detector these differences are negligible.

Based on this comparison alone, the best near detector location would be midway between the sites labeled "1" and "2," roughly half way between the location of the NuMI shaft and the entrance to the MINOS near detector hall. This site gives electron and total neutrino spectra that are reasonably similar to those at the far-detector site. One cannot optimize for both the electron and total neutrino fluxes at the same time. The electron neutrinos come predominantly from the muon decays farther downstream in the decay pipe while the muon neutrinos, which make up 99% of the total flux, originate from somewhat farther upstream. Although the ν_μ flux is expected to be quite different because of $\nu_\mu \rightarrow \nu_\tau$ oscillations, the total neutrino flux, which gives rise to the neutral current backgrounds, is worth trying to match. At Site 1.5, the expected event rate is 17 events per 4×10^{13} pot/kT (one proton spill at design NuMI intensity per kT). A more detailed comparison between the neutrino fluxes expected at this site and those expected at the far site is shown in Fig. 9.4.

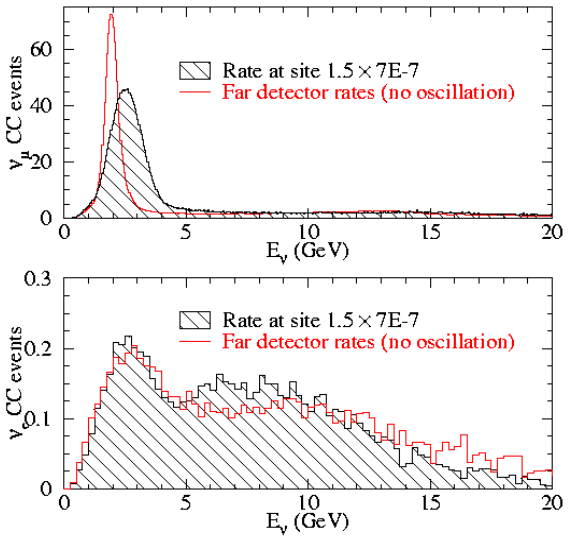

Fig. 9.4: The muon- and electron-neutrino event rates in a detector located at site "1.5."

9.3.2: Near Detector Design: We have designed the NOνA Near Detector to be as similar to the far detector as possible and to fit into the space available at site 1.5 in the access tunnel to the MINOS near detector hall. This detector would be 3.7 m wide by 4.9 m high by 10 m long. With the same transverse (~4 cm) and longitudinal (~23 cm) segmentation as the far detector, it would have 22 planes containing 2,640 horizontal liquid scintillator tubes and 22 planes containing 1,980 vertical tubes. The total number of tubes would then be 4,620, which is also the number of electronics channels. The detector would have a mass of about 120 metric tons.

The 10-m length of the detector provides a 3-m long fiducial region, preceded by a 1-m long upstream "veto" region and followed by a 6-m long downstream region that provides efficient identifi-

cation of muon-neutrino charged current events. The ~1-ton fiducial region is defined by the requirement that neutrino event vertices should be at least 1.5 m from the edges of the detector. A clean sample of ν_μ charged current events is required for the study of ν_e backgrounds arising from this process, described later in this chapter. For reference, overall 10 m depth of the detector is sufficient to range out a 1.5 GeV muon that traverses its entire length.

Approximately two neutrino interactions will occur in the near detector during each 8-microsec beam spill of 4×10^{13} protons on target. The slow response of the high-gain APD electronics used on the far detector will likely prove unsatisfactory for this environment. We expect that the off-axis near detector will be instrumented with photomultiplier tubes and fast electronics similar to that used in the MINOS near detector. Other differences in near and far detector response will result from the shorter tube and WLS fiber lengths. Corrections for these differences will be determined from measurements made with the NOνA Calibration Detector, as described in Section 9.8 below.

Finally, the detector assembly and installation procedures for the near detector will also be different from those used for the far detector. Access shaft limitations may require the particleboard absorber planes and the PVC extrusions for the near detector to be moved underground separately and assembled at the detector site.

Although design optimization for the NOνA near detector is still at an early stage, we believe that the space available in the access tunnel to the MINOS near detector hall will prove adequate for our needs and that additional excavation will not be necessary.

9.4. Cross Section Uncertainties

As was described in Chapter 8, the beam-related backgrounds to a $\nu_\mu \rightarrow \nu_e$ oscillation search fall into three categories: intrinsic ν_e contamination in the beam, neutral current events, and charged current ν_μ events where the outgoing muon is not identified. The challenge is to measure not only the sum of these backgrounds in the near detector, but to predict accurately the total contribution at a far detector.

Assuming the near and far detectors have the same background rejection capabilities, one can also consider these different fluxes to determine the far over near ratio for the three different backgrounds, as a function of near detector off axis angle. Fig. 9.5 shows the far to near ratio for the three different backgrounds, as a function of near detector off axis angle, assuming the far detector is 12 km off axis, 820 km from Fermilab. The simulation assumed a detector of RPCs and particleboard, with 4 cm transverse segmentation and a third of a radiation length longitudinal segmentation. The conclusions would be similar for other choices of readout technology, optimized for the figure of merit (the signal over the square root of the predicted background).

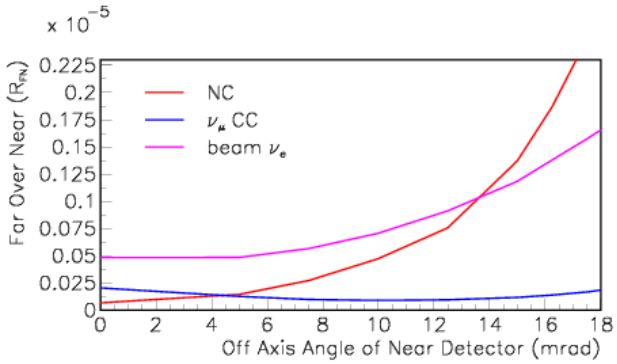

Fig. 9.5: Far-over-near ratios for the three different backgrounds as functions of off-axis angle of a Near Detector. We assume the far detector is 12 km off axis at 820 km from Fermilab (14 mrad), and that $\Delta m^2_{32} = 2.5\text{x}10^{-3}\text{eV}^2$ and $\sin^2 2\theta_{23} = 1$.

As an example of what uncertainties would be for the far detector background prediction assuming an identical near detector, consider the effects due to our current imprecise knowledge of cross sections. Neutrino interactions in this energy regime can be classified as four different kinds of processes: (quasi-) elastic, resonance, coherent, and deep inelastic scattering (DIS), where each of these processes can be either neutral current (Z-exchange) or charged current (W-exchange).

In the (quasi-) elastic process, the proton is knocked out of the nucleus and the final state lepton is a (muon) neutrino. In resonant processes a Δ resonance is created, which then decays to a proton or neutron, and a pion. Figure 9.6 shows the current set of measurements of this process in the charged current channel [1]. The neutral current processes are even more poorly constrained.

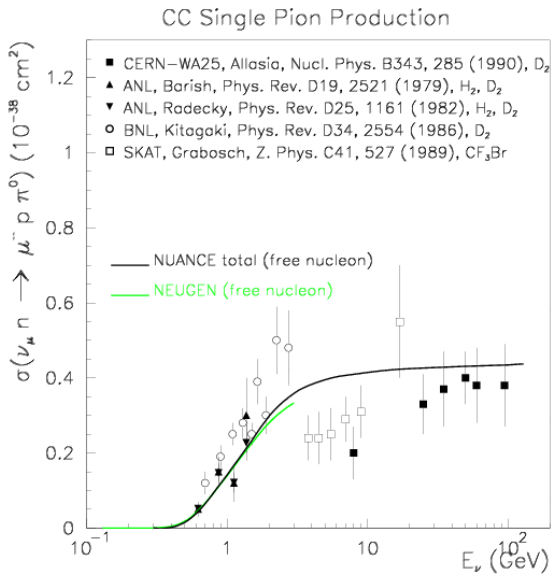

Figure 9.6: Compilation of charged current single pion production cross-section measurements [1].

Coherent processes are where the neutrino scatters off the nucleus as a whole, and the only final state particle produced (besides the lepton) is a single pion—a charged pion for the charged current process, a neutral pion for the neutral current process. Coherent neutral current interactions, while rare, are a significant fraction of the neutral current backgrounds. In these events, most of the final state energy is in an electromagnetic particle. The only ways the detector can distinguish this from the signal is (1) by identifying two incident particles, i.e., two decay photons instead of a single electron, and (2) because the final observed energy is often significantly less than the incoming neutrino energy. Coherent charged current interactions, on the other hand, will not play a significant role and are not included in the simulations. Fig. 9.7 shows a compilation of both charged and neutral current coherent pion production cross-section measurements.

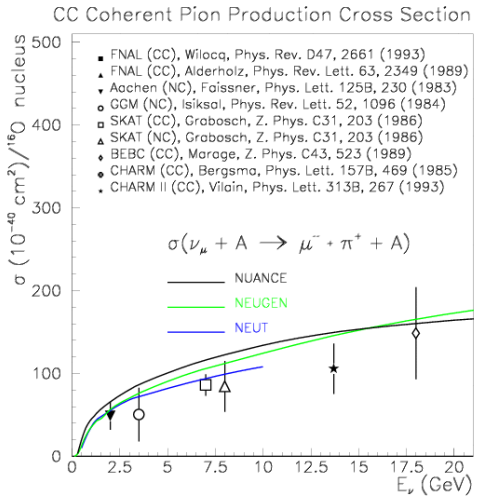

Figure 9.7: Compilation of coherent pion production cross-section measurements. Both charged and neutral pion production are shown [1].

Process	Quasi-elastic	$\Delta \rightarrow \pi^0 X$	$\nu A \rightarrow \nu A \pi^0$	DIS
$\delta(\sigma)/\sigma$	20%	40%	100%	20%
Signal ν_e	55%	35%	N/I	10%
NC	0%	50%	20%	30%
ν_μ CC	0%	65%	N/I	35%
Beam ν_e	50%	40%	N/I	10%

Table 9.1: Neutrino scattering processes that contribute as either signal or background, the uncertainties on those processes at low energies, and the fraction of each process for each background (±5%). N/I means not included.

Table 9.1 shows the processes, estimates of their associated uncertainties (at the relevant neutrino energy) and their contributions to the background. To evaluate the systematic error in the far detector background prediction due to these uncertainties, we use the simulation to determine by how much the far-to-near ratio would change for shifts of each cross section by its uncertainty. Fig. 9.8 shows how shifts in each of these cross sections would change the total far to near ratio and therefore produce a systematic uncertainty in the background prediction.

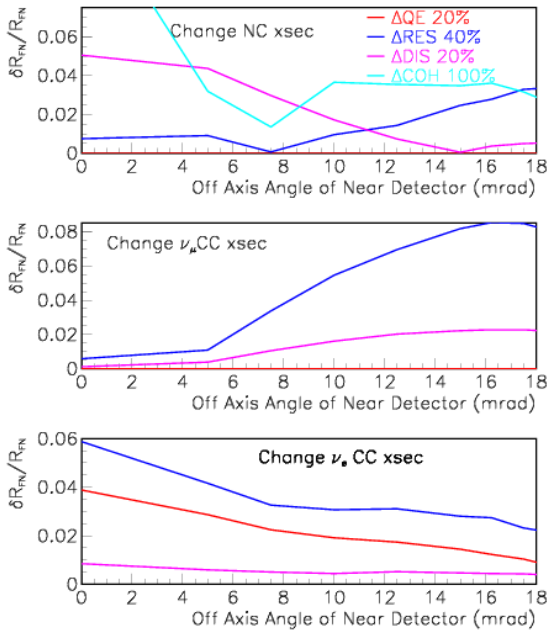

Fig. 9.8: Fractional changes in the far to near ratio (R_{FN}) due to current uncertainties in neutrino cross sections. Uncertainties on the energy dependences of the cross sections are not included.

Fig. 9.8 shows that, the farther off axis one places the near detector, the less the cross section uncertainties will contribute to the ν_e and neutral-current backgrounds. At such locations the $\nu_\mu$and ν_e fluxes have more similar energy distributions to those at the far detector flux, and so the same processes would dominate and there is some cancellation. However, for the ν_μ charged-current backgrounds, the farther off axis one goes, the more likely the events will pass the analysis cuts and so the background level rises.

Fig. 9.9 shows the errors from the above plots added in quadrature. Clearly at all off-axis angles there are significant uncertainties. One way to reduce these uncertainties is to increase the segmentation for sections of the off-axis near detector to better separate the various backgrounds from each other. However, there is currently an experiment proposed to do dedicated cross-section measurements in the NuMI beamline (i.e., MINERνA), and these measurements would reduce several of the cross section uncertainties described above.

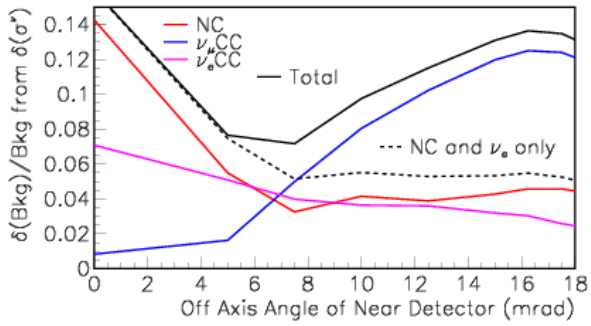

Fig. 9.9: Total cross section errors for a near detector that is identical to the far detector (without auxiliary measurements).

The following three sections describe some auxiliary measurements that could be made to reduce these background uncertainties. First, the charged current cross sections themselves can be better measured (on axis, for example). Second, if one can independently determine the ν_μ charged current backgrounds present in the near detector, the remaining error due to cross-section uncertainties will be reduced to about the 5% level (for a near off-axis detector located at least 8 mr off axis). To minimize the uncertainty due to the imperfect knowledge of the energy dependence of the remaining relevant cross sections, 12 mr would be where the electron neutrino fluxes (and hence the source of the largest background) are best matched to the far detector.

9.5. The MINOS Near Detector

The first question one might ask is whether or not the presence of the MINOS near detector, which is located on the NuMI beam axis, will help in reducing either cross-section or flux uncertainties. Unfortunately, the MINOS near detector will have a limited role to play in NOνA. The MINOS detectors are optimized for muon detection in the few GeV energy range and use 2.54-cm thick steel plates for the absorber material. At this segmentation, the ability of the MINOS detectors to separate electron neutrino events from neutral current events is significantly worse than for the NOνA detector [2]. A direct translation of the "*e*-like" sample measured on the beam axis by the MINOS near detector to a detector optimized for electron neutrino appearance, located off the beam axis,

will rely on detailed models of both detectors and the incident neutrino beam.

The most reliable procedure for estimating the off-axis electron-neutrino flux using the MINOS near detector would start with the measurement of the CC muon-neutrino event rate by the MINOS near detector. From this rate one can infer the ν_e rates using a Monte Carlo prediction of the (far ν_e)/ (near ν_e) ratio. A prediction of this ratio can be made to better than 5% on the beam axis because most uncertainties cancel. The last step is again to rely on a Monte Carlo prediction to translate the on-axis electron-neutrino flux to the off-axis location. Again, since this relies on ratios, many uncertainties cancel. The largest remaining source of uncertainties comes from the ratio of neutrino cross sections at the peak of the off-axis spectrum (2 GeV), to the cross-sections at the peak of the on-axis spectrum (6 GeV).

Using this method, we expect to be able to predict the electron neutrino flux at an off-axis detector with roughly 15% accuracy. Note, however, that this method yields the electron neutrino event rate before corrections for detector efficiencies or cross sections are taken into account. Unfortunately, these corrections will be large, since the ν_μ events that are detected in the MINOS detector are certainly a very different mix of DIS, resonance, and quasi-elastic channels than those events which would pass analysis cuts in a fine-grained near or far detector off the NuMI axis.

9.6. The MINERνA Detector

The proposed MINERνA detector can contribute substantially towards reducing the uncertainties on the backgrounds for NOνA. The MINERνA experiment is designed to measure neutrino-nucleon cross-sections in the few GeV region, and was proposed to Fermilab in late 2003 [3]. The detector has a completely active scintillator target, surrounded by electromagnetic and hadronic calorimetry. The transverse segmentation is 1.65 cm, and the longitudinal segmentation is 1.7 cm. Therefore by summing together two MINERνA planes and ignoring the following nine planes, one can approximately simulate the longitudinal granularity of the NOνA Near Detector, and also measure background rejection as a function of detector granularity. The proposal is to begin the MINERνA running with the detector on the NuMI axis, although the possibility of eventually running at an off-axis location is not precluded.

Even with the detector on axis, MINERνA can make significant contributions to NOνA. Because it is a purely active detector, it can identify ν_e and ν_μ quasi-elastic events with minimum backgrounds from resonant or DIS processes, and provide the cleanest measurement of the ν_e and ν_μ interaction rates as a function of neutrino energy. The fluxes themselves should be predicted to about 5%, from the MIPP experiment [4] combined with NuMI horn B-field measurements. This implies a measurement of the quasi-elastic cross section to about 5%, compared to the current 20% uncertainty. In addition, because of its final state reconstruction capabilities, MINERνA should be able to identify and measure the charged-current resonance processes and reduce the uncertainty on that cross section as well. Therefore, the ν_e flux and estimated background level in the near and far detectors should be predictable with MINERνA to the few percent level.

The MINERνA detector on axis can also provide an important constraint on the ν_μ charged current background. Because the MINERνA detector has very fine segmentation and is totally active, it has better low-energy muon identification than the NOνA detectors. Muons that range out will decay to electrons whose energy can be seen in the pure scintillator detector, while pions will more likely be captured before they decay. In addition, because the MINERνA detector is five times more segmented, low-energy hadronic interactions of pions are more likely to be identified. Although the on-axis and off-axis fluxes are quite different, the study of charged-current processes on-axis is still quite relevant because the total neutrino energy can be reconstructed and the ratio of ν_μ fluxes on and off axis will be well-constrained by MIPP measurements to the few percent level.

9.7. Auxiliary Near Detector Measurements

Besides measuring the sum of all the backgrounds in an identical material, the NOνA Near Detector can also provide an additional handle on the charged current background. In order to do this, it must be made several meters longer than would otherwise be needed to contain the ν_e signal events.

To determine the fraction of ν_μ charged current events that would pass all analysis cuts, one can measure that fraction for events with identified muons, and then predict the number of times that the muon is undetected. This procedure works in the limit that the nature of the hadronic system in a neutrino charged current interaction is dependent only on the hadronic energy of the system, and not on the neutrino energy.

In the analysis described in Chapter 8, in order for the ν_μ CC events to be misidentified as NC events, there has to be a track identified as an electron (most likely an asymmetrically decaying π^0) *and* the muon has to be missed. The cases where a muon is misidentified as an electron, thus fulfilling both conditions, appear to be rare. We define a muon as a non-shower-like track that traverses at least 8 planes, which is approximately 2.7 radiation lengths. Thus, high *y* events (where *y* is defined as the fractional neutrino energy loss) form the majority of the ν_μ CC background.

ν_μ CC events, to a very good approximation, are characterized by a flat *y* distribution near high *y*. Thus, to a good approximation, for a given neutrino energy, the distribution of these events with muon range >8 planes, which satisfy our signal criteria should be flat, when plotted as a function of muon range (equivalent to 1-*y*). The contribution to the background from ν_μ CC events with muon range <8 planes can just be obtained by the integral of this distribution for muon range between 0 and 7 planes, as obtained from the extrapolation of the observed distribution. In reality, the flatness expectation is altered by the fact that our selection criteria for the signal interact at some level with the energy of the muon. Moreover, our energy spectrum is not monochromatic. By allowing a slope in this distribution and its extrapolation, these effects can be incorporated.

The relevant length distributions for the different categories of events are shown in Fig. 9.10. The top figures show the range distribution for NC and beam ν_e events. Here the "muon" is most likely a charged pion (or less likely a proton) that has traveled far enough without interacting visibly to appear like a muon. As expected, there is a sharp increase in such events for short range, and for range >14 planes the contribution is very small. The distribution for the ν_μ CC events, as might be expected, extends to much larger ranges. Furthermore, a linear fit to this distribution not only fits the data with range > 14 well, but also appears to agree well with the predicted number of events with $5 \leq \text{range} \leq 14$. This vindicates our procedure and gives one confidence that linear extrapolation below range of 8 based on this fit is still valid.

The fourth plot gives the range distribution for all of the above backgrounds summed together. Clearly, this would be the only distribution accessible in the experiment. A fit to those data with range >14 can be used to extrapolate to the number of background events with "muon" range <8 planes. The answer obtained is about 20% ±30% higher than the actual number of ν_μ CC background events.

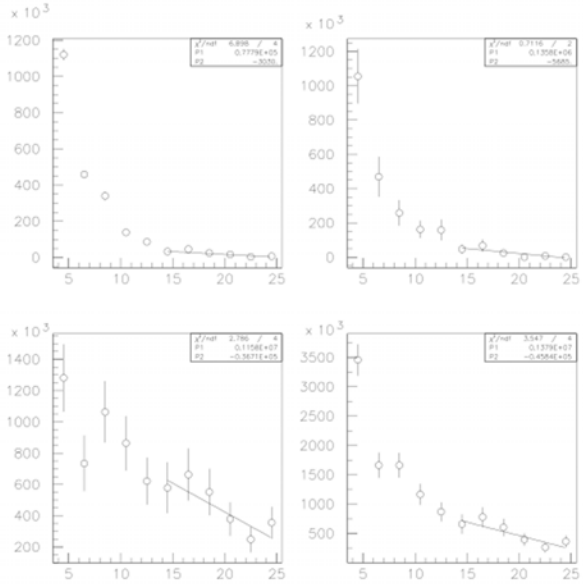

Fig. 9.10: Length distributions (in units of planes, where 1 plane is 0.33 radiation lengths) for the several categories of near detector events. Top left - NC; top right - beam ν_e; bottom left - ν_μ CC; bottom right - total event sample.

To show how much an error on the extrapolation would contribute to an error in the far detector background, we compare the number of background events in the far detector under two different assumptions about ν_μ CC. One is the correct assumption about the fraction of ν_μ CC events in the near detector background and the other when this fraction is either under- or overestimated. Fig. 9.11 shows the difference between the correct far detector prediction and the wrong one, assuming one has the fraction of ν_μ CC events wrong by

10% or 20%. Although the far detector background is small because of oscillations, it must be measured to better than 10% of itself to get a total uncertainty of less than 5% at a near detector location where other uncertainties are minimized.

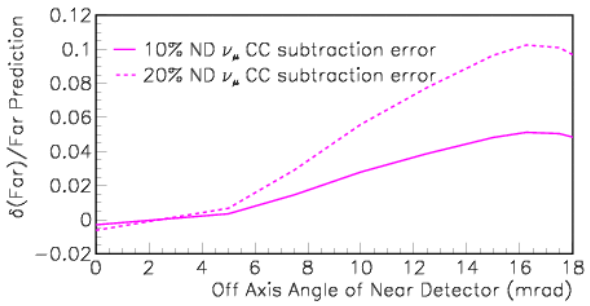

Figure 9.11: Fractional change in the total far detector prediction due to different charged current subtraction errors in the near detector.

9.8. Test Beam Program

The NOνA Near and Far Detectors will have to be calibrated *in situ*, as was the case for the MINOS detectors, and therefore will experience similar limitations to this process. Requirements for the absolute and relative (between the two detectors) energy calibration in the appearance experiment are not as stringent as for MINOS. However, the efficiency of event reconstruction, which is critical for NOνA, generally improves with better calibration. For NOνA disappearance measurements, we assume the same requirements as for MINOS: the energy scales should be determined with 5% absolute and 2% relative uncertainty. More critical for NOνA will be understanding of topological response (a pattern of hits) of electromagnetic interactions. The detailed response function of the low-density detector can be used to tune algorithms to identify an electron signal and to reject backgrounds, mostly from $\pi^0 \rightarrow \gamma\gamma$ followed by the photon conversions in the hadronic cascades.

We assume that the far detector will be located in a surface building with no overburden, while the near detector will be placed in the MINOS near-detector hall access tunnel. There will be a high rate of cosmic ray tracks in both detectors, which will provide a stable source of muons to monitor and calibrate detector response. Although cosmic rays are unlikely to pose a significant background problem, as described in Chapter 10, a detailed understanding of detector response will be essential to maximize the efficiency of event identification and the accuracy of energy determination.

Since neither of the two detectors can be directly exposed to a test beam to enable such calibrations, we plan an extensive test-beam program to expose a special calibration module, a smaller replica of the large detectors, to a charged-particle test beam. Using selectable beam momentum settings and a particle identification system, a full response matrix of the detectors can be measured. The special calibration detector will be constructed with longitudinal and lateral segmentations identical to that of the large detectors. The readout electronics will also replicate the techniques employed by the far and near detectors. The test beam program described here is derived from the MINOS experience and takes advantage of lessons learned there.

We envision several elements of the test beam program that can be executed in stages. Below we present a preliminary outline of the main goals of the program.

FY05 and FY06 (pre-construction period):

- Various prototype versions, consisting of a small number of the far and near detector cells, will be constructed and tested with prototype front-end electronics readout and data acquisition.
- Beam test data will be taken to verify the expected response.
- Response to cosmic ray muons will be studied simultaneously and compared to beam interactions.
- Test beam activities will provide feedback for the improved design and future fabrication and installation effort.

FY07 to FY09 (detector construction period):

- A final version of the calibration detector will be designed and constructed. The overall size of the detector will be large enough to contain electromagnetic and hadronic cascades of energy up to 5 GeV.
- As the first large-scale assembly of the final design components, the construction of the detector will teach lessons about installation of the far and near detectors.
- The calibration detector will be exposed to the test beam in a series of test runs, in both near and far detector configurations.

Collected data will provide a basis to determine a complete response matrix to all particle species at relevant energies and angles.

- A study of response to cosmic ray muons will be conducted simultaneously and compared to beam muons. The energy deposition by cosmic ray muons will provide the energy calibration link between the two detectors.
- Collected data will be analyzed to obtain the maximum information on the response topology of cells hit as a function of particle species and energy.
- The electromagnetic component of hadronic cascades will be studied.
- Collected data will be used to tune Monte Carlo simulations of the detector response and as an aid in developing the most efficient pattern recognition algorithms.

The main requirements for this calibration apparatus are:

- Identical structure and segmentation as the far and near detectors.
- Sufficiently long to contain hadronic cascades with energies up to 5 GeV.
- Sufficiently long to ensure detailed understanding of response to penetrating muons.
- The front-end readout electronics as similar as possible to both near and far detector configurations (probably different).
- Readout electronics capable of handling the higher intensity of interactions expected in the test-beam line.
- The front-end electronic readout that is triggerable by an external trigger (e.g., Cherenkov or TOF counters).

NOνA does not have any unusual demands for the performance of a test beam. However, the beam should have a momentum range of 0.1 to 5 GeV/c, with the absolute momentum known to a few percent, and an integrated particle identification system. It is desirable to have such a test beam at Fermilab, where the entire collaboration could easily contribute to its operation. We would rely on Fermilab support for beamline operation, instrumentation and monitoring, and for integrated data acquisition and processing. During the last three years of our test beam program we would need access to the beam for several months each year.

9.9. Conclusions

We have demonstrated in this chapter that, with a simple detector located around 12 m off the NuMI beam axis, along with the MINERνA detector on axis, each of the beam-related backgrounds can be predicted at the far detector with uncertainties of about 5%. Without the MINERνA detector, and the cross section and ν_e flux measurements it can provide, the NOνA Near Detector design would have to be modified. This would include small regions at the upstream end of the detector with increased longitudinal granularity to provide essential additional information for background determination.

A flexible and versatile test beam facility will significantly improve the sensitivity of our experiment. We would like to work with the Laboratory to plan for the construction or upgrade of a test beam facility that meets NOνA requirements..

Chapter 9 References

[1] G. Zeller, "Low-energy neutrino cross sections: comparison of various Monte Carlo predictions to experimental data," hep-ex/0312061, proceedings of NuInt02, Irvine CA, 12-15 December 2002.

[2] M. Diwan, M. Messier, B.Viren, L. Wai, "A study of $\nu_\mu \rightarrow \nu_e$ sensitivity in MINOS," NuMI-NOTE-SIM-714, February 2001.

[3] D. Drakoulakos *et al*., "Proposal to perform a high-statistics neutrino scattering experiment using a fine-grained detector in the NuMI beam," February 2004 (http://www.pas.rochester.edu/minerva).

[4] P.D. Barnes Jr. *et al*., "Proposal to measure particle production in the Meson Area using Main Injector primary and secondary beams," FERMILAB-PROPOSAL-0907, 1998 (http://ppd.fnal.gov/experiments/e907/)

10. Cosmic Ray Backgrounds and Active Shield

10.1. Introduction

The cosmic ray background will be strongly suppressed in NOνA by the very low duty cycle of the accelerator beam (~10 μs spill every 2 seconds), directionality of this incident neutrino beam (pointing from Fermilab) and its relatively high energy (1.5-2 GeV). Our preliminary estimates, described below, indicate that this background should not be a problem. Furthermore, this background can be measured with very high precision during the off-beam time. It is also our intention to test our estimates in a subsidiary experiment on the surface during the next year using a small version of a proposed detector.

The atmosphere behaves as a 10-interaction length, 25-radiation length calorimeter for the incident primary cosmic rays. The results of interactions in the atmosphere are extensive air showers, some of whose components persist to the surface: penetrating muons with ~4 GeV average energy, showering electrons and photons with average energies in the range of tens of MeV, and some hadrons, primarily neutrons, with hundreds of MeV, on average. To estimate the effects of these secondary particles on operation of the NOνA Far Detector we assume: that the detector is 28.8 m wide, 14.4 m high, and 185 m long; that the absorber is a wood product with density 0.65; and that the live-time of the detector is 100 seconds per year (10^7 spills per year, each 10 μs long). We discuss next the manifestation of each component on the detector separately.

10.2. Detailed Considerations—Muons

The muon flux at the surface of the Earth is approximately 120 $\cos^2\theta$ m^{-2} s^{-1} sr^{-1}, where θ is the zenith angle. This flux yields an average of 13 muon trajectories inside the detector per 10 μs spill-gate and a total of 1.3×10^8 muons per year in the Far Detector during the active spill. For the proposed 500 ns electronic gate, each gate will contain an average 0.65 muons over the approximately 5,000 m^2 area of the detector. This flux is a small perturbation on the overall single-element counting rates due to internal and external radioactivity and photodetector noise. Indeed, these muons provide an essential calibration and alignment tool. The muons have a median energy of 4 GeV, and 10 to 20% originate in the same air shower, appearing as in-time multiple tracks. Using an expression for the integral flux as a function of energy and zenith angle [1], we estimate that 51% of the muons will stop in the detector. Muons themselves clearly cannot simulate our signal, which could only happen through their interactions in the detector.

In a segmented detector, it is possible for muons to pass through absorber layers without being detected in the active scintillator. These muons can generate a possible background if they interact hadronicly and produce a charged track along the direction of the neutrino beam from Fermilab. Pion production in hadronic interactions of cosmic ray muons near the earth's surface has been measured; the rate is $(3.5\pm0.7)\times10^{-6}$ π^+/muon/g/cm^2 [2]. A calculation which agrees with these data has been made, and gives the π^+ production rate as a function of the energy of the incident virtual photon [3]. From this calculation, we estimate that the production rate of all pions above 2 GeV photon energy (and assuming that π^+: π^-: π^0 are produced in the ratio 1:1:2 at high energies) is ~5.6×10^{-6} /muon/g/cm^2. Fig. 10.1 shows the distribution of these muon-hadronic interaction points projected on to the face of the detector. The calculation assumes that the muon passes through either zero or one active detector plane, corresponding to a 30 cm wide passive absorber plane. Approximately one half of these interactions lie within 1 m of the detector sides. We estimate that 1000 such interactions will lie within the detector's fiducial volume during one year of operation.

The overall energy flow in these interactions is exactly orthogonal to the beam direction. The highest energy pions are therefore produced perpendicular to the neutrino beam (vector meson dominance), but some nucleon isobar production also occurs and isobar decay may produce tracks in the beam direction. In that case, there must also be particle emission in the opposite direction to balance momentum so that the probability that a track should appear electron-like, with the appro-

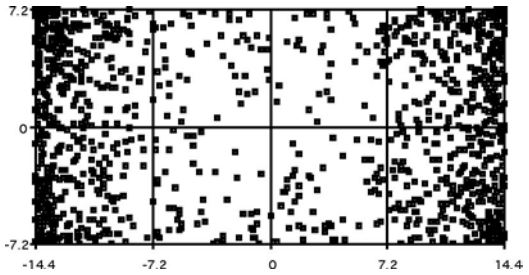

Fig. 10.1: Hadronic interaction points along trajectories of undetected muons. The interaction points are projected on to the face of the detector.

priate energy and interaction topology, makes this an unlikely source of background.

An active shield of scintillator modules around the outside of the detector would be a relatively easy and inexpensive way to efficiently indicate the presence of in-time muon responsible for such events and make the background negligible. The area of shield detector required is only ~ 3% of the total active scintillator planes used in the detector. Assuming that the shield scintillator strips are arranged parallel to detector layers, an interaction in a specific gap would be directly correlated with a corresponding scintillator strip.

10.3. Detailed Considerations—Electrons and Photons

A significant flux of electrons and photons from the extensive air showers survives at ground level. The net flux is about 50% the muon flux, but their average energy is less than 100 MeV [4]. They will generally produce small showers that penetrate short distances (less than 1 m typically) into the top of the detector. Only ~2% have energies above 1 GeV and are capable of producing a significant shower or "splash" at the top of the detector, causing multiple hits in the scintillator strips.

10.4. Detailed Considerations—Neutrons

A small component of hadrons survives to ground level. Neutrons are the most significant; they have an interaction length of ~1.5 m in the absorber material and their interactions are therefore a potential source of background. Their trajectories are much more vertical than the muons, with average angle ~20° from the zenith, and their median energy is ~100 – 200 MeV. Figure 10.2 shows the integral flux of neutrons incident on the top of the detector calculated from the measured

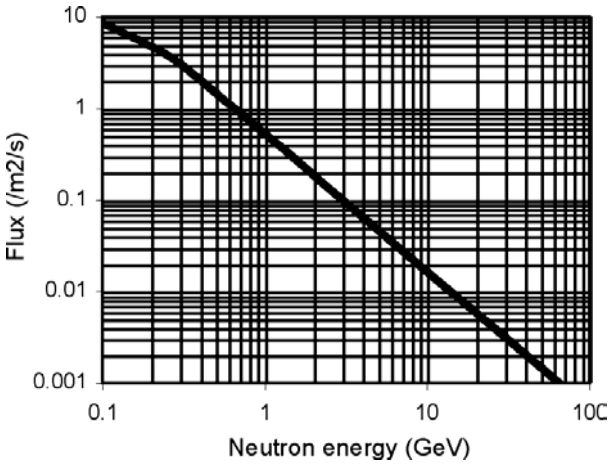

Fig. 10.2: Integral flux of neutrons at ground level

differential flux [5]. We estimate that 1.0×10^5 neutrons with energies above 2 GeV will interact in the detector per year within the neutrino spill gate; they will be concentrated near the top of the detector.

Even though neutrons at ground level are always accompanied by muons or electrons, this fact is not very useful as a veto for neutrons entering the detector because of large typical spatial separation. Using the generic cosmic ray code CORSIKA [6], we found that only 4% (10%) of the neutrons have an accompanying muon within 50 (100) m, providing no satisfactory veto power for the proposed detector dimensions.

In the few GeV energy region, ~20% of the inelastic neutron interactions produce a single pion, which, in principle, might simulate an electron track. 98% of all CC events have a track within 25^o of the neutrino beam direction and thus a pion from a neutron interaction must be emitted at an angle at least ~60° to provide a possible background to a beam neutrino event. From kinematics, the maximum possible energy of a pion to be emitted at 60° is 1.5 GeV, just at the edge of possible acceptance. With the addition of a topology requirement that the track should be electron-like, we estimate that background from neutron interactions will be at the level of only ~1 event/year.

10.5. Passive Overburden

One possible method to deal with background effects of cosmic rays, should they turn out to be more serious than the above estimates indicate, is through direct attenuation using a passive absorber

above the detector. While the absorber itself, crushed rock or soil, is cheap, supporting the absorber, both laterally around the detector and especially vertically over the detector, is expensive. It is therefore important to compare a passive absorber with an "active shield" either in the form of a detector fiducial cut or in special, active elements mounted over the upper portions of the detector, as discussed above in connection with muon identification.

Fig. 10.3 shows the relative effect of an overburden on the relative vertical intensities of muons, electrons and photons, and neutrons. The neutron interaction length λ has been taken as 115 g/cm^2 [7] and that for the electron-photon component, 175 g/cm^2, taken from electromagnetic shower attenuation after shower maximum. There is no particular limit to the thickness of an overburden: the neutron flux would be reduced a factor of 100 by a dirt or rock overburden of 500 g/cm^2, ~2 to 2.5 m. This reduction would also reduce the electromagnetic "splash" at the top of the detector. We note that hadronic interactions of the throughgoing muons also produce neutrons. For this thickness of absorber, the production rate of neutrons in the absorber by these muons is approximately equal to the flux of attenuated neutrons from interactions higher up in the atmosphere. The muon-initiated neutrons are typically produced in large hadronic showers. If they are produced in the absorber directly above the detector, they will always be closely associated with the very energetic initiating muon.

10.6. Need for an Active Shield

Possible cosmic ray backgrounds are significantly attenuated by both the short neutrino beam spill and by the orthogonality between the horizontal neutrino beam direction and the vertical maximal direction for cosmic ray flux. Nonetheless, cosmic rays are a potential background source, which will require monitoring effort by recording a large number of off-spill events. To reduce backgrounds from cosmic rays to a minimum, the installation of an active shield around the upper portions of the detector appears prudent. Such a shield is significantly less expensive than the support structure required for passive shielding of sufficient thickness to have a significant effect. We describe a possible shield in the next section.

10.7. Active Shield Design

As discussed above, an active shield may be useful in tagging cosmic rays entering the detector. This can be done by adding active elements on the sides and top of the detector as shown in Figure 10.4. We assume the active shield would be composed of elements similar to the 1.22 m by 14.6 m scintillator modules in the main detector. Since the detector is 29.3 meters wide and 171.3 meters long, it takes 280 modules to cover the top. Similarly since the detector is 14.6 meters high and 171.3 meters long, a set of 140 modules will cover one side as shown in Figure 10.4. The side sections of the shield would be attached to the building walls so that access to the sides of the detector

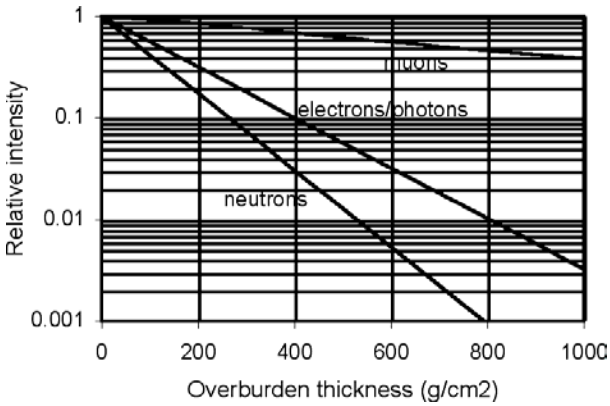

Fig. 10.3: Relative attenuation of muons, electrons and photons, and neutrons as a function of thickness of a dirt overburden.

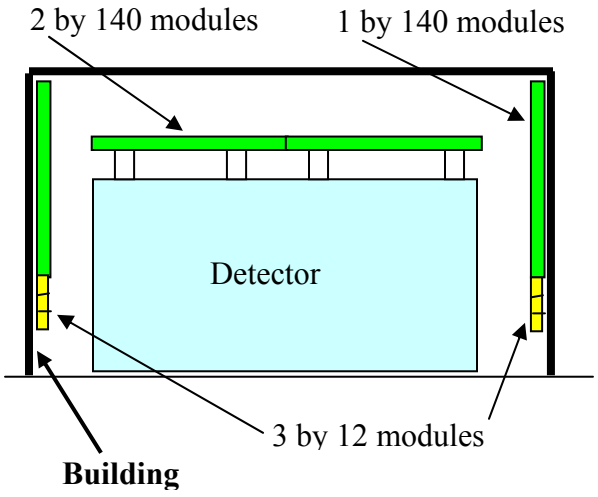

Fig 10.4: Beam's eye view of the detector and Active Shield.

and its electronics would be preserved, therefore an additional 36 modules are required on each side to cover the gap created by this access space. Active elements are not required on the front and back of the detector since the first and last planes in the detector effectively do the same job. The top section of the shield would be supported off the main detector about 2.4 m above the top of the detector so that access to the top of the detector would be preserved.

A single active layer is sufficient. This design requires 632 additional modules for an active shield, 176 to cover one side, 280 modules to cover the top, and with 30 cells per scintillator module, 18,960 APDs and electronics readout channels are also required.

10.8. Required R&D

The Active Shield is part of our cost estimate, but the need for the shield is not yet firmly established. Since the proposed 50 kiloton detector is live for only 100 seconds each year, it is possible to directly measure these cosmic ray rates with a smaller mockup if we run it continuously for a few days or months.

Through our Virginia Tech collaborators we have obtained the loan of 29 BELLE RPCs, each 2.2 meters by 2.7 meters. We are in the process of assembling about 20 of these RPCs into a detector mockup of particleboard absorber interspersed with RPCs to search for cosmic ray induced event candidates which simulate 2 GeV ν_e CC events. Two orthogonal views of the test setup are shown in Figure 10.5. The total mass of the RPCs and particleboard will be about 16 metric tons. For the 100 sec/year of far-detector live-time, (50 kT / 16 tons)×100 sec = about 3.6 days/year in our the background test setup. We estimate that fiducial volume cuts and readout deadtime will increase this by about a factor of four, so a 5-year NOνA run can be simulated in about 2.4 months.

Figure 10.6 shows our progress to date in assembling the test setup in Lab E at Fermilab. The RPCs have been leak tested, a gas system has been built, and we have begun to assemble the RPCs inside particleboard frames. Argonne National Laboratory has contributed a 30-channel Cockroft-Walton HV chassis, and they have designed and built a 64-channel RPC readout board in VME

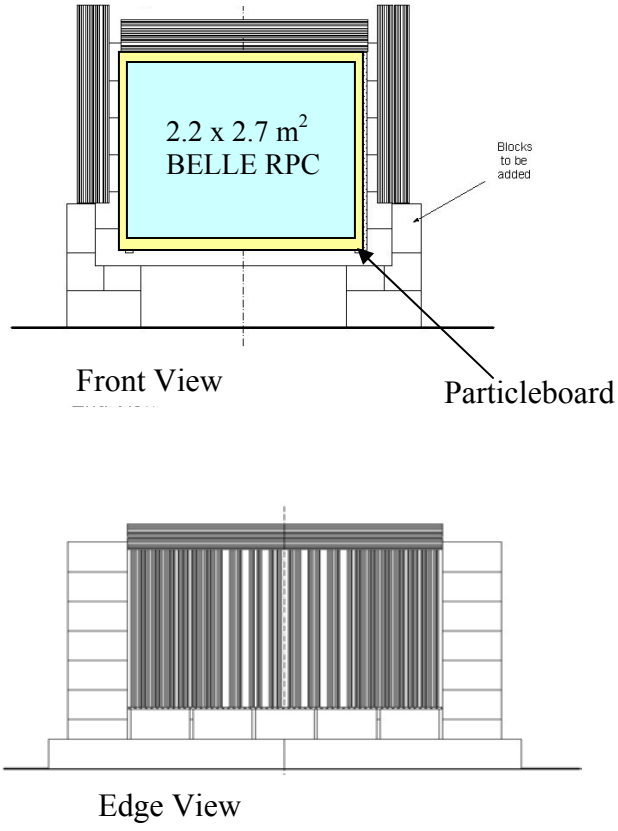

Figure 10.5: RPC front view and edge view of the R&D Cosmic Ray Background Test setup.

Figure 10.6: The beginnings of the Cosmic Ray Background Test setup in Lab E at Fermilab.

format. Our progress is now limited by the funding required to build the complete readout electronics for this test.

We also have another way to make this measurement. The MINOS collaboration recently completed their CalDet calibration run with a MINOS prototype in a CERN test beam. The sixty-five 1 x 1 m^2 arrays of MINOS solid scintillator strips are now available to the NOνA collaboration and could also be used in the Cosmic Ray Background Test setup. Due to this year's MINOS installation, it is not clear if sufficient photomultipliers and electronics will be available for such an test. If not, we are faced with a similar funding problem to acquire the PMTs and electronics to readout a reconfigured CalDet + particleboard mockup.

We believe this Cosmic Ray Background Test effort should have a high priority given its possible impact on the overall detector design and cost.

Chapter 10 References

[1] H. Jokisch et al., Phys. Rev. D19, 1368 (1979).

[2] R. Hertenburger et al., Phys. Rev. C52, 3449 (1995).

[3] J. Delorme et al., Phys. Rev. C52, 2222 (1995).

[4] R. R. Daniel and S. A. Stephens, Revs. Geophys.and Space Sci, 12, 233 (1974).

[5] F. Ashton, "Cosmic Rays at Ground Level', ed. A. Wolfendale (1974); W. N. Hess et al., Phys. Rev.116, 445 (1959).

[6] D. Heck et al., Report KfK6019, Forschungzentrum Karlsruhe (1998).

[7] Particle Data Group, "Review of particle properties," Phys. Rev. **D66**, 010001 (2002), "Atomic and nuclear properties of materials," p.84.

11. Far Detector Site and Building

11.1. Detector Site Criteria

We have examined more than a dozen possible sites for the NOνA Far Detector as well as multiple detector locations within several particular sites. Possible sites begin ~710 km from Fermilab, near the city of Aurora MN, and continue to the north-northwest until a point in Ontario that is about 900 km from Fermilab. Sites more distant than ~900 km are too far off-axis to have desirable beam characteristics because of the beam's upward inclination of 3.3° and the curvature of the Earth. The sites we have examined are all near the half-dozen or so east-west all-weather roads that cross the NuMI beamline.

The principal site selection criteria are:

• Approximately 10-14 km off-axis from the NuMI beam. The beam in this direction has a most probable energy of ~2 GeV. The optimal off-axis distance is not precisely known because of uncertainty in current best value of Δm_{32}^2. An additional issue is the question of strategy. Sites closer to the NuMI beam axis have increased flux and therefore a higher probability of observing the $\nu_\mu \rightarrow \nu_e$ transition. Sites further off-axis provide more sensitivity to matter effects and therefore possibly more accurate measurements of the mass hierarchy and CP violation.

• As far as practical from Fermilab. Beam lengths of ~775 to ~850 km from Fermilab are readily achievable. The dependence on beam length is not strong. A longer beam is more sensitive to matter effects, while a shorter beam and therefore higher flux may yield a better reach in $\sin^2 2\theta_{13}$. One argument for a longer beam is that it is more different from the K2K beam and the CERN-Gran Sasso beam and thus provide a better handle on resolving ambiguities in the neutrino mixing matrix parameters.

• An optimal site will have year-round road access at the maximum trunk highway weight limit, adequate electrical power and T-3 capable communications access. Other geographic criteria include access to workers, road transportation and airports and proximity to support services such as hotels, restaurants, gasoline and other retail outlets.

• An optimal site will have at least 20 and more likely 40 acres of usable land (not wetlands) and permit a layout of a ~200 m by ~40 m footprint for a detector building oriented with its long axis pointing towards Fermilab.

• An optimal site will enjoy strong local support and its selection should be unlikely to result in land use controversies or litigation. The characteristics of the site should also facilitate a straightforward environmental permitting process. Although the University of Minnesota has authority to determine zoning and permitting with respect to its property within Minnesota, minimal land use controversy will facilitate the laboratory construction.

11.2. Most Suitable Sites

While no site is perfect and a number of sites are more than adequate, three particular areas appear to best meet the selection criteria, while also providing considerable flexibility in deciding the actual detector "footprint." From south to north, these sites are: (1) on the Orr-Buyck Road (St. Louis County Highway 23) near the west end of Kjostad Lake, (2) on the Ash River Trail (St. Louis County Highway 129) near the entrance to Voyageur's National Park and (3) on Ontario Highway 11 north of Rainy Lake near Mine Centre ON (about 60 km east of Fort Frances ON). Sites (1) and (2) are west of the beam centerline. Site (3) is east of the beam centerline. Of these sites, the Ash River Trail location has the unique property of being the furthest site from Fermilab in the United States. For this reason, it is the baseline site. The locations of all three sites are shown on the map in Fig. 10.1.

11.2.1. Ash River Trail Site: The Ash River Trail site is located about 15 km east of U.S. Highway 53, about 40 km east south east of International Falls MN. By car, it is about an hour's drive further from the airports at Duluth and Minneapolis than is the laboratory at Soudan. Driving time from Soudan to Ash River is about 1.5 hours.

The access to the Ash River Trail site is via U.S. Highway 53, St. Louis County Highway 129 and then via a private road ~1-3 km in length, depending on the specific site that is chosen. Highway 129 has some spring weight restrictions that will necessitate some load rearrangements for ~45 days

each Spring. There is an existing 7.2 kV, 3 phase power line that runs essentially along the highway. The local power company estimates that 500 kW is readily available with existing facilities; 1 MW or more of power consumption would require an upgrade of the current line. There is an existing fiber optic line along U.S. 53 and along the Ash River Trail.

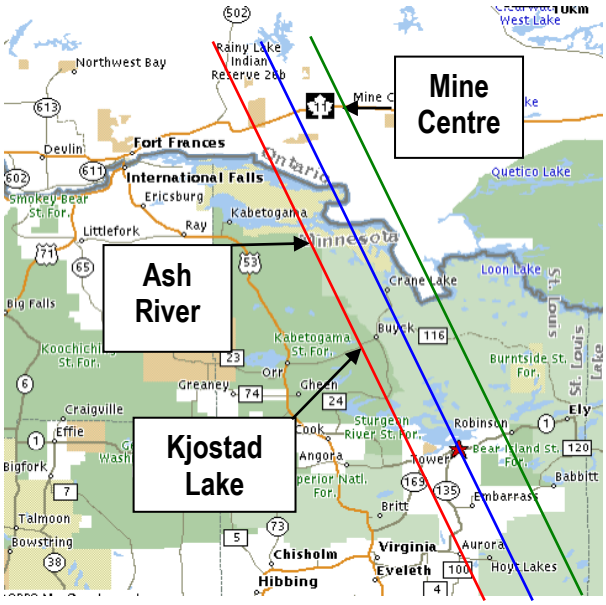

Fig. 11.1 Map showing all three preferred sites. The star indicates the site of the Soudan Underground Laboratory. The beam centerline passes through Soudan; the left line is ~13 km west of the centerline, while the right line is ~13 km east of the centerline.

The settlement of Ash River (U.S. Mail address: Orr MN 55771) is located at the end of the Ash River Trail, about 2 km east of the proposed detector site. This area has several motels and restaurants, although much of the activity is seasonal. (See www.ashriver.com for a listing of hotels and restaurants.) There is a new gas station and convenience store at the intersection of the Ash River Trail and U.S. 53, about 12 km from the laboratory site.

The actual detector laboratory locations at the Ash River Trail site are in Sections 12, 13 and 14 of Township 68 North, Range 15 West, St. Louis County MN. These locations are shown in Fig. 10.2 on the 1:24000 USGS topographic map. All locations would require upgrading of the access road, mostly with an improved gravel base and culverts for drainage (or a new road in the case of Site F). The sites are located near Voyageur's National Park, but GIS studies by the National Park Service suggest that the Detector Laboratory would be essentially invisible from the Park because of intervening high terrain (except for Site F). These sites are all ~810 km from Fermilab. The detailed parameters of all six locations are listed in Table 11.1.

All detector locations shown on the map are on relatively flat land with few, if any, obvious rock outcrops. Thus, it is reasonable to believe that all of these sites have at least a few meters of soil cover over bedrock. Core drilling will be required to more completely characterize a chosen location. Most of the locations are forested with small aspen trees. In forestry terms, they are generally described as areas of aspen regeneration.

All sites would require installation of utilities along the access road. Domestic water would likely come from one or more wells, which would also be used to fill a storage tank for fire protection water. Domestic sewage would require either a septic system or a holding tank with periodic disposal.

At this time, the University of Minnesota is taking preliminary steps towards land acquisition and environmental review of these sites. Our current strategy is to defer a specific selection among the sites for as long as possible, in order to have the best possible understanding of the relevant neutrino oscillation parameters before making a specific site selection.

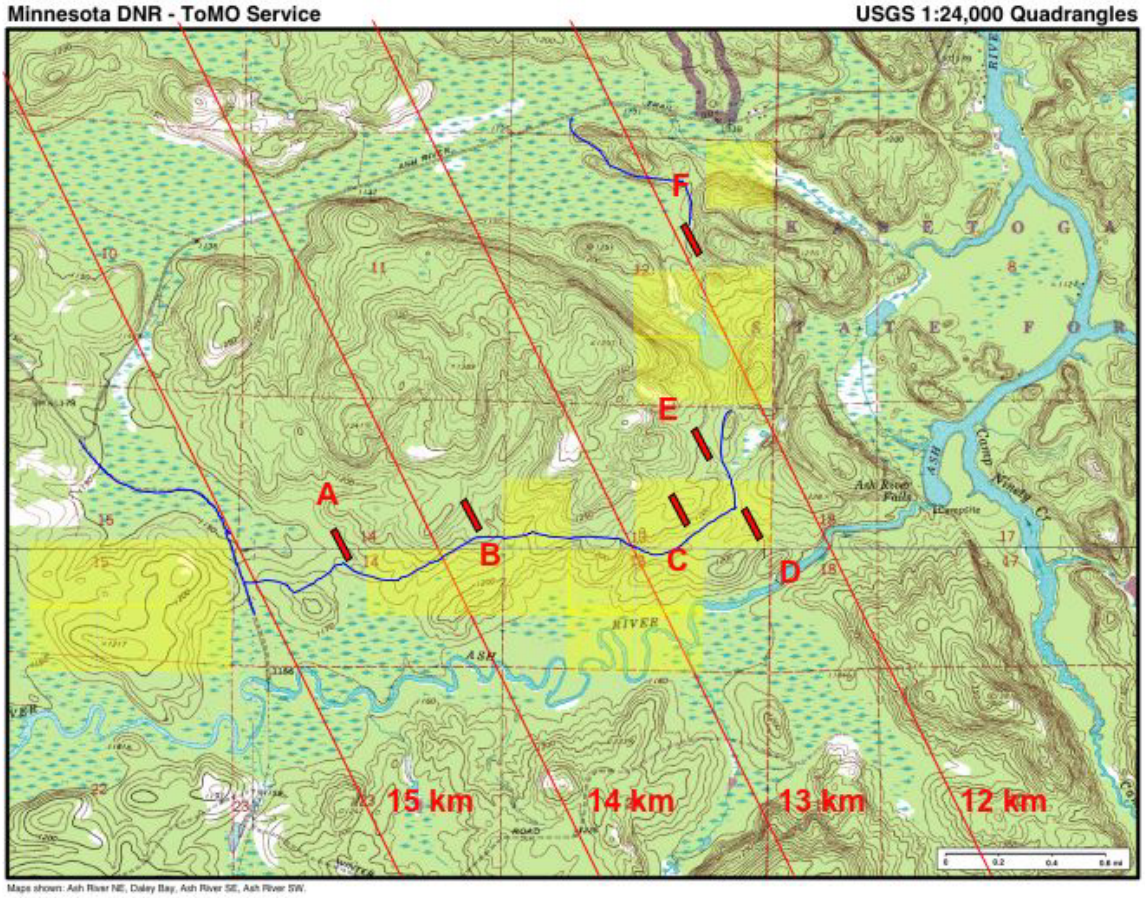

Fig. 11.2: The USGS topographic map for the Ash River Trail sites. The rectangles show a 200 m by 40 m laboratory footprint. The shaded land near the laboratory sites belongs to Boise Cascade. Unshaded land in this area belongs to the State of Minnesota.

Location	Description	Latitude	Longitude	L (km)	T(km)	Angle (mr)	Ownership
A	SENW Sec. 14	48.375°	92.869°	811.4	14.37	17.6	State
B	SENE Sec. 14	48.377°	92.857°	811.2	13.51	16.7	State
C	SWNE Sec. 13	48.378°	92.841°	810.7	12.46	15.4	BCC
D	SENE Sec. 13	48.377°	92.836°	810.5	12.19	15.0	BCC
E	NWNE Sec. 13	48.381°	92.840°	811.0	12.26	15.1	State
F	SWNE Sec. 12	48.391°	92.840°	812.0	11.81	14.5	State

Table 11.1: Parameters of Sites Near the Ash River Trail.

11.2.2. Kjostad Lake Site: The Kjostad Lake sites lie both north and south of St. Louis County Highway 23, approximately 8 km west of Buyck and 15 km east of Orr. Highway 23 is a two-lane, all-weather highway, which intersects U.S. 53 at Orr. North of Buyck, the road ends at Crane Lake, which is a U.S. port of entry for non-vehicular traffic from Canada. East of Buyck, the Echo Trail runs ~100 km to Ely. While the Echo Trail is usable most of the year, only ~15 km near Ely is paved. Orr has several gas stations and cafes, a supermarket, a bank and a few other stores, as well as a new AmericInn motel overlooking Pelican Lake. Buyck has several cafes and a golf course.

Electrical power and fiber optic cable run along Highway 23.

There are numerous possible detector sites in the Kjostad Lake area that lie 13±2 km off the central NuMI beam axis. All sites are ~775 km from Fermilab. Most of the sites are wooded, although often with only small aspen trees. Some of the possible sites belong to private owners, but much of the land belongs to the State of Minnesota, either outright or as tax-forfeit land. The largest private land owner in this area is the Potlatch Corporation.

At this time, we regard the Kjostad Lake detector locations as alternates to the Ash River Trail locations, so we are not currently pursuing detailed site selection in this area.

11.2.3. Mine Centre Site: The furthest practical site from Fermilab, ~845 km away, is on Ontario Highway 11, near Mine Centre ON, about 60 km east of Fort Frances ON. Ontario Highway 11 is an all-weather highway with electrical power, telecommunications and a rail line all running in a parallel corridor between Fort Frances and Thunder Bay ON. This site is east of the beam centerline on Crown (public) land. There are few constraints on land use in this area and it is likely possible to pick a specific detector location essentially adjacent to the highway and utilities at almost any desired distance off-axis by >5 km. We consider a site west of the centerline less practical, because the land in that area is a First Nation reservation.

We have had positive initial discussions with provincial and municipal officials regarding the feasibility of locating the NOνA Far Detector in the Mine Centre area. The disadvantages of a Canadian site are primarily more difficult logistics. Most detector elements and personnel will approach any of the NOνA Detector sites from the south, either on U.S. 53 or the adjacent Canadian National rail line. The Canadian site entails the additional complexity of another hour of driving time and the variable time required for the border crossing. For this reason, a substantial Canadian participation in NOνA would likely be important to managing logistics and facilitating work at Mine Centre or any other Canadian site.

11.3. Other Sites

We have also visited numerous sites close to Soudan. The distance from Fermilab for these sites varies from ~710 km at the Cliffs-Erie Mine site near Aurora to ~745 km for sites near Big Bay on Lake Vermillion, near the Fortune Bay resort complex. While these sites offer somewhat higher operational efficiency because they are in a more populated area than the sites further north, these sites have somewhat reduced matter effects because of the shorter baseline. For those reasons, we are not investigating these sites at this time.

A second Canadian site is available on Crown land on Ontario 502, which runs northeast from Ontario 11 to Dryden ON. This site would be the furthest possible location, ~900 km from Fermilab. However, although Ontario 502 is an all-weather highway, there is currently no electrical power or telecommunications along this route. This stretch of highway also has essentially no support services for about 100 km.

11.4. Building

The NOνA Far Detector requires a detector enclosure ~200 m long by ~35 m wide by ~24 m high. This is a substantial structure, so we commissioned two design studies to get a handle on the costs and cost drivers for such large buildings. The first study was sponsored by the University of Minnesota and was performed by CNA Consulting Engineers with subcontracts to Dunham Associates and to Miller-Dunwiddie Architects [1]. This CNA study focused on a cut and cover approach deep in bedrock with a 10-meter overburden to cover a "worst-case scenario" of a possible required cosmic ray shield.

The second study was done by the Fermilab Facilities Engineering Services Section [2] and focused instead on zero overburden. The Fermilab design is for an above-grade building with a minimal excavation just down to bedrock to ensure the 50 kilotons is sitting on a solid surface. Bedrock at most of the sites considered above is expected to be under only 10 to 15 feet of soil till. At the present time we do not anticipate using earth shielding around or over the detector building. These two design studies indicate that sufficient Earth shielding to have a significant effect (several meters in thickness) would increase the cost of the building by ~50%. Chapter 10 indicates that even this modest overburden is probably not necessary.

While the two building design studies had different goals, they did agree with each other in cost at the 20% level when the Fermilab surface design was compared to a similar subsection of the Minne-

sota design done by Miller-Dunwiddie. In addition, both designs had common assumptions about the general site, for example including modest costs for short roads connecting to existing roads and modest cost to bring in nearby power. Not all sites under consideration satisfy these assumptions, though the Ash River Site is a close match.

For the base detector design in this proposal, we anticipate constructing a 20-year life, metal-sided, metal-roofed building, similar to the usual experimental area buildings located at accelerator laboratories. The building would have an additional 20-meter long staging and assembly area at one end so that semi-trailers delivering either particleboard or PVC modules could be moved inside for unloading. This staging and assembly area would not require the full 20 m height. Another low-roof section would be attached to the middle of one side of the building to handle the scintillator fluor and mineral oil delivery, mixing, and storage. The details of the scintillator preparation and storage requirements are discussed in Chapter 7.

The building meets the horizontal wind stress loads, snow loads, and heating and cooling loads required in northern Minnesota. This area sits on the Canadian Shield and is seismically stable, so no special earthquake design features are required. The building would be insulated, heated and cooled to ~70 ± 10 F year round. The cost of appropriate humidity control (for particleboard) is still under investigation.

The building would be outfitted with a 20-ton building crane on a 35-meter bridge and two mobile gantry cranes for detector assembly. A small control room and a small technician work area would be included inside the main structure. In addition, this "outfitting" of the building would include a robust steel structure underneath the detector to allow access to the bottom. This bottom support would be a simple set of I-beams along the length of the building, each 2-foot high, 1 foot wide, and spaced 3 feet apart. The detector particleboard / PVC structure would sit on top of the I-beams. Another light structure on top of the detector would hold the active shield counters high enough off the top of the detector to allow easy human access. This top structure might be made of scaffolding and catwalk assemblies.

The scintillator oil delivery and storage tank section would require a fully engineered secondary containment. In the main detector building the concrete floors and walls below grade may suffice for secondary containment. For example, the Fermilab MiniBooNE oil tank is a sphere containing 0.8 kilotons of mineral oil and sits in a cylindrical vault of concrete as its secondary containment. In the MiniBooNE case, the only precaution taken in the vault section is that the ground water sump enclosure (for water entering the perimeter of the building and being ejected into the local ground water distribution) has walls high enough to be above the level of the oil even if all of the oil were to leak out of the spherical tank. No special containment pan was required inside of the MiniBooNE vault. In the case of the NOνA Detector, our cellular structure should allow arguments that the worst credible spills are much smaller than those mitigated in the MiniBooNE case. All these secondary containment issues and their associated costs are still under investigation and are of course dependent on possibly different environmental protection regulations in the different states / provinces.

11.5. Research and Development Topics

The constructing and outfitting of the detector building is a high cost element of this project. Since the detector itself can be considered as a structural element, there are potential trade-offs between the building and detector structure. Sufficient civil engineering needs to be available to make a conceptual building design that takes advantage of the detector structure and points out any detector decisions that may significantly increase the building cost. Obvious issues include detector construction speed, safety, and long-term detector stability.

Chapter 11 References

[1] Report for Off-Axis NuMI Neutrino Detector, U of M Project No. 298-03-1113, January, 2003.
[2] Off-Axis Detector Enclosure Design Study Report, Fermi National Accelerator Laboratory, FESS Engineering Project No. 6-2-22, June, 2003. Also available as Off-Axis Note #9.

12. Proton Beam Requirements

12.1. Introduction

This proposal assumes a 5 year run with the 50 kiloton (kT) NOνA far detector and beam intensity in the Main Injector such that the NuMI target receives 4 x 10^{20} protons on target per year (pot/yr). The delivered pot/yr comes from the assumption of 4.3 x 10^{13} protons per pulse (ppp) every 1.9 seconds and a Main Injector annual beam-on fraction of 0.56 (= scheduled beam time x operational efficiency). There are other possible ways of attaining this integrated number of pot/yr, as will be discussed in this chapter. We note that the Main Injector is not yet capable of delivering these protons and that a significant new investment in the accelerator complex will be required in order to achieve this. On the other hand, the NuMI beam has been designed for this ppp intensity which translates into approximately 0.4 MW of beam power.

In this chapter, we discuss some issues regarding the proton intensity, a sensible level of investment in that area for NOνA and the likelihood of achieving the assumed intensity. The most realistic means of delivering the expected protons will require a proton intensity plan, including a reduction of the Main Injector cycle time. We also look ahead to the pot/yr associated with this experiment's long range physics potential as discussed previously in Chapter 5.

12.2. Proton Intensity Investment Strategy

The sensitivity of NOνA depends on the simple product of neutrino flux times far detector mass. To very good approximation the integrated neutrino flux is determined by the number of 120 GeV protons that can be delivered to the NuMI target. Assuming a fixed total cost for the combination of the detector mass and the proton flux, it makes sense for the collaboration and the laboratory together to consider investment in both of these areas in order to optimize sensitivity. We note that, in order to achieve the proton intensity assumed here, the lab must undertake a substantial new investment in this area. Alternately, the lab could simply invest more in additional NOνA detector mass. We believe a joint approach, examining both mass and protons, is likely the most sensible path.

We recognize that investment in proton intensity has much broader usefulness for a variety of future physics programs at Fermilab. Hence, increased proton intensity may be attractive to the laboratory beyond a simple optimization for NOνA.

Viewed from the NOνA side, we believe it is important to assume a detector no smaller than 50 kT. At this time, a well defined plan to deliver the assumed proton intensity does not exist. Relatively risky investments in proton intensity should not be considered as an even trade-off in less risky construction of additional detector mass. The main investments in proton intensity should focus on relatively low risk means of delivering more protons even before a new Proton Driver can be completed. We believe that reduction of the Main Injector cycle time stands out as a unique opportunity that meets these criteria.

12.3. Current Planning for Proton Intensity

Fermilab has an ongoing investment in the accelerator complex to increase the proton intensity for a variety of experiments, including $\overline{p}$ production and Collider luminosity improvement. Recently a study [1] aimed specifically at proton intensity from the Booster and Main Injector was undertaken. The laboratory management directed the study to consider what could be accomplished with an investment of a few times $10M over a several year period. The committee was chaired by Dave Finley with input and participation from laboratory management, experiment collaborators, and Beams Division managers and technical experts. The primary charge to the Finley committee was to study the issue of proton intensity before the anticipated operation of an off-axis experiment. All aspects of the needs in the existing proton source and Main Injector were considered. On the timescale of 2008, the committee anticipated that significant effort and resources will have been invested in the LINAC, Booster and Main Injector.

The Finley Committee report recommends investment in several areas to meet these proton demands:

- Improve control over beam in the Booster to decrease losses and permit more total protons to be accelerated.
- Increase the average acceleration rate capability of the Booster from about 3 Hz to about 7-10 Hz.
- Improve collimation and notch cogging in the Booster to reduce losses and permit lower loss multi-batch stacking into the Main Injector.
- Solve the power tube problem in the LINAC.
- Improve the damping and beam loading compensation systems in the Main Injector to permit higher proton intensities and stacking.
- Develop and implement batch stacking systems in the Main Injector for $\bar{p}$ production and eventually for multi-batch operation.
- Implement a mild reduction in Main Injector cycle time if this can be done easily.

Some of the work recommended by the Finley Committee is already incorporated into Accelerator Division planning and some is underway. The Fermilab Accelerator Division has recently established a new project for increasing proton intensity, with a planned budget over the next several years of roughly $5M per year.

12.4. Possible Accelerator Investments

As discussed above, an important issue for Fermilab to consider in undertaking NOνA is an enhanced level of investment in the existing accelerator complex. The investments relevant to 120 GeV protons for NuMI can roughly be characterized in four categories:

1. Investment in the per-cycle proton intensity capabilities from the 8 GeV proton source. Examples include improvements in various systems to correct/compensate for space charge effects and other instabilities.
2. Investment in techniques to reduce or "hide" the cycle time of the current 8 GeV source from the cycle time of the Main Injector. Such investments would increase the rate of acceleration cycles in the current Booster and also develop techniques to hide the Booster cycle time from the Main Injector cycle time. One approach discussed for the latter is to use the existing Recycler Ring, along with a new transfer line, as a "proton stacker" so the Booster could fill this ring while the Main Injector ramps. Some type of Booster batch stacking into the Main Injector could potentially decrease the Main Injector cycle time by as much as 1 second. This assumes collider running has ended.
3. Investment in the ability of the Main Injector to handle higher proton intensities and techniques for establishing such intensities. This consists of various Booster batch stacking techniques (slip stacking, barrier stacking, and "ramp" stacking have been suggested) along with the RF power and feedback/stability systems necessary to deal with higher intensities.
4. Reduction of the Main Injector cycle time available for providing protons to the NuMI target. Studies suggest that, with adequate magnet and RF power systems, the Main Injector ramp time (not including the time to fill it from the 8 GeV source) could be reduced to as little as 600 ms [2]. The specific medium-term investment required will depend on some of the other parameters of the overall proton demands (protons for $\bar{p}$ production being a major consideration). However, an attractive feature of investment in this area is that the necessary medium-term improvements will be either essential or at the least very useful in the era of an 8 GeV Proton Driver.

We note that the Finley report has called out a faster Main Injector ramp as a likely prime direction for investigation as follows:

> "Increasing the Main Injector ramp rate can obviously increase the number of protons per hour delivered by the MI for the 120 GeV Neutrino Program. An ongoing recent study, if demonstrated to be technically feasible, shows the MI ramp time can be reduced from the current 1.5 sec to 1 sec, or perhaps less. This modification requires both more RF power and more magnet power supplies. This will provide more protons per year to the 120 GeV Neutrino Program as long as antiproton stacking for Run II does not slow the MI cycle time down. It appears to be a relatively low risk approach to getting more protons per year in that it requires engineering development to get more cycles per year rather than the beam physics R&D that is needed to get more protons per cycle. This modification alone is expected to cost a few $10M's. A decision on this must fold in with the recommendations of the Long Range Planning committee, since ideally a new Proton Driver would also make use of this modification."
>
> [reference 1, page 37, our emphasis]

The Proton Driver Study [3] suggests that the cost of the Main Injector cycle time work necessary for the magnet power upgrades is about $9M. The cost of additional RF cavities and power supplies is in the range of $14M. These are "unloaded" costs, so the real totals are more likely $20M and $30M. Hence, a very rough estimate for the total cost of the project is at least $50M. These "loaded" costs should be compared to our "loaded" detector costs outlined in Chapter 13. The cost will also depend on the specific goals of cycle time reduction, since there is a range of assumed intensities and features that one can tune in adding a second, NuMI-only cycle. We believe a directed study on this issue is essential and should be undertaken by the lab immediately.

12.5. NOνA and the NuMI Beamline with a Proton Driver

Over the last year, the idea of building a new 8 GeV Proton Driver has become a centerpiece of the recommendations of the Fermilab Long Range Planning Committee. Both synchrotron and LINAC options have been suggested, and in either case, the nominal design goal is that a total beam power of 2MW will be available from the Main Injector at 120 GeV. This corresponds to $2x10^{21}$ pot/yr delivered to the NuMI target (about 5 times the intensity assumed for this proposal).

The physics case for an enhanced second phase experiment ("SuperNOνA"?) with this beam power has been discussed in Chapter 5. A Proton Driver extends the reach of NOνA for virtually every measurement. Discovery or precision measurement of $\nu_\mu \rightarrow \nu_e$ oscillations is extended. High statistics anti-neutrino running and / or the possibility of running at the second oscillation maximum to resolve the mass hierarchy becomes real. Observing CP violation in the lepton sector may even be possible. A Proton Driver adds yet another exciting feature to an incremental program exploiting the existing MINOS detector, existing NuMI beamline and the NOνA detector. The incremental nature of the NuMI neutrino program is a powerful feature. Each step has a practical cost and we need not proceed unless the science indications warrant going ahead.

In either Proton Driver option, it is anticipated that improvements in the Main Injector are an intrinsic part of the accelerator upgrade effort. We note that the nominal 2 MW of proton beam power from the Main Injector corresponds to $2x10^{14}$ protons per cycle with a 2 second cycle time or 10^{14} protons per cycle with a 1 second cycle time.

Such changes in cycle time also impact the stability of the target and other systems in the NuMI beamline. A target to handle pulses of 10^{14} protons/second may be much easier to build than one to handle twice that number every 2 seconds. The overall issue of removal of the average heat is the same in either case, and will require non-trivial upgrades to the existing NuMI target facility. It is expected that a traditional carbon target like the existing NuMI target can survive 10^{14} protons per pulse but probably will fail with twice that number. The higher number may require the use of something like a liquid mercury target. Again, the shorter cycle time buys additional engineering certainty.

A final issue is whether there will be radiation problems in the NuMI beamline with 2 MW of protons. We do not anticipate any significant differences in this area with a 1 or 2 second cycle time. We anticipate that the NuMI beam design is sufficiently conservative that relatively small modifications should permit operation up to 2 MW. With the current design, it is anticipated that the first possible problems may come in the target hall. If may be possible to address these at relatively low cost, without additional civil construction. It is anticipated that the decay pipe region will be able to accommodate the higher flux, but perhaps will require additional cooling.

12.6 Summary on Proton Intensity

We believe that reduction of the Main Injector cycle time represents an essential investment for Fermilab to undertake as rapidly as possible for NOνA. Cycle time reduction can provide major improvements in the neutrino flux for NOνA in the near term and also match nicely with futures involving a Proton Driver.

We believe that discussions within the laboratory and between our collaboration and the laboratory could lead to a practical intensity vs. time model for the neutrino program. This model would be characterized by a "NuMI base proton level" (meaning likely to occur with a 90% confidence level) and a "NuMI design proton level" (meaning a 50% confidence level which may occur if many of the details go according to plan). This would

reprise the scheme recently used for Run II collider luminosity and would get us all on the same page regarding this issue.

We propose that Fermilab undertake a specific study for this purpose with a goal of completion by the end of 2004. This would mean merging information from the near term proton intensity project with the future Proton Driver possibility. Such a study would be an important next step in establishing a world-class program of neutrino physics with the NuMI beam.

Chapter 12 References

[1] Report to the Fermilab Director by the Proton Committee, October 26, 2003, http://www.fnal.gov/directorate/program_planning/studies/ProtonReport.pdf

[2] Proton Driver Study II, Part 1, Section 20, May 2002. http://www-bd.fnal.gov/pdriver/8GEV/

[3] Proton Driver Study II, Part 1, Appendix 1.

13. Cost Estimate and Schedule

13.1. Introduction

We have constructed a cost estimate for a project that will carry out the physics program described in this proposal. The entire cost estimate is available in an Excel Workbook format upon request. In this chapter we explain briefly the methods used and discuss some of the important features of the estimates for each of the major elements of the proposal. We have also included a brief discussion and summary of the costing that has been done for two alternative active detectors, namely solid scintillator and glass RPC chambers. In addition, we present discussions of our contingency analysis and a model for costing operational expenses, both during and after the completion of the construction project.

Table 13.1 presents a high-level summary of the second-generation cost estimate made for the baseline active-detector technology as well as other costs associated with the project.

Section 13.6 describes the schedule that we envision for the construction of the NOνA detectors, which is shown schematically in Figure 13.1.

Section 13.7 and Table 13.2 present a comparison of the costing for three active detector technologies, which used a preliminary conceptual design for each technology. The results of this exercise, along with evaluation of the detectors' physics capabilities, played an important role in the choice of baseline technology.

13.2. Cost Estimate Methodology

In preparing this cost estimate we have primarily followed the principles used in costing and tracking the MINOS Detector construction project. For each major system we have itemized the materials and services (M&S) that must be procured, fabricated or assembled. Each system is itemized to the lowest level that is realistic for the current state of the system design. For each cost estimate we indicate the source of the estimate as a vendor quote (VQ), engineer's estimate (EE) or physicist estimate (PE). These sources are used to distinguish the confidence level in each estimate and hence are used in the contingency determination.

For each system we also itemize the labor tasks associated with the construction of each system. The cost of each task is determined by identifying the type of labor and duration of time required to carry out the task. Each type of labor is assigned a labor rate. For the purposes of this preliminary estimate we have used labor rates based on Fermilab salaries and fringe (SWF) for technicians, designers, drafters, engineers and project management personnel. For staff and installers at the far detector site we have used the labor rates currently applicable at the Soudan Underground Laboratory. Labor estimates have been made by either engineers or physicists based on time and motion studies or recent experience with similar tasks.

For each detector system we have included costs for engineering, design and engineering oversight (EDIA) throughout the life of the construction project. At this stage we have done this by estimating the person-years required based on experience from similar scale projects. We have also included costs for project management and ES&H oversight through out the life of the construction project.

Our cost summary includes an estimate for institutional overhead based on percentages calculated from the actual costs incurred on the MINOS Detector project, namely 28% for SWF, 9% for M&S procurements under $500k, and 1.5% on the first $500k of procurements of $500k or larger, and 0% on the remaining amount of the procurement. This assumption about reduced overhead on large procurements must be negotiated with the Laboratory. We have included in our contingency funds to cover additional overhead in case such an arrangement is not agreed to.

Contingency is estimated on each item or task based on the confidence level of the estimate, or on an analytical calculation based on a plausible variation of the unit cost or labor estimate.

Table 13.1 summarizes the results of our cost estimate for the construction of this experiment. All costs are presented in FY 2004 dollars.

13.3. The Baseline Detector Cost Estimate

For this proposal we have selected liquid scintillator as the baseline technology for the active detector elements. In this section we briefly discuss each of the major pieces of the estimate.

WBS	Description	Base Cost	Overhead	Contingency	Sub-total
1.0	Near Detector	2,152,582	430,516	2,583,099	5,166,198
2.0	Far Detector				
2.1	Absorber	12,618,525	476,991	3,708,788	16,804,304
2.2	Active Detector	28,324,540	1,468,466	9,230,940	39,023,945
2.3	FEE, Trigger and DAQ	6,375,205	705,098	3,864,988	10,945,290
2.4	Shipping&Customs Charges	5,421,343	1,084,269	1,355,336	7,860,947
2.5	Installation	11,789,067	3,069,957	5,661,376	20,520,401
	Detector Sub-total	64,528,679	6,804,781	23,821,428	95,154,888
3.0	Building and Outfitting				
3.1	Building	16,634,800	499,044	9,971,283	27,105,127
3.2	Outfitting	4,745,748	142,372	4,888,120	9,776,240
	Building and Outfitting Sub-total	21,380,548	641,416	14,859,403	36,881,367
4.0	Active Shield	1,602,882	416,749	2,019,631	4,039,262
5.0	Project Management	3,935,000	1,085,650	1,004,130	6,024,780
TPC	**Total Project Cost**	**93,599,690**	**9,379,113**	**44,287,691**	**147,266,495**

Table 13.1: Work Breakdown Structure and second generation cost estimate for Liquid Scintillator as the Active Detector technology.

13.3.1. Absorber: There are two key elements in the costing of the absorber. The first is the unit cost of the particleboard and the second is the maximum size board available from the vendor. We have obtained quotes from three different vendors. We found that current prices range from $0.10 to $0.12 per pound, not including delivery and that 8-ft by 24-ft by 1.125-in sheets should be available. Quoted Delivery costs by truck to the detector site in northern Minnesota have also been included.

The cost estimate for the absorber system also includes the materials cost of glue, screws and brackets for assembling the absorber sheets into stacks. The cost of the detector support structure is included in the building outfitting

13.3.2. Liquid Scintillator Active Detector: There are three major components to the liquid scintillator active detector. These are the PVC extruded modules, the wavelength shifting fibers and the liquid scintillator, which is a 9:1 mixture of mineral oil and fluor (pseudocumene). The baseline detector requires the assembly of ~18,000 extruded modules with endcaps, fibers and manifolds. It is the simplicity of this assembly process that makes the liquid scintillator "win" as the most cost effective active detector. The time/motion analysis of the module assembly process indicates that a factory staffed with three assemblers and one supervisor can assemble 12 modules in one shift. At this rate, two assembly factories can produce the modules at a rate matched to the stack assembly and installation at the far detector site. Over the four-year production and installation period, the module assembly can be accomplished for under $2M, which is significantly cheaper than can be envisioned for the equivalent process for the alternative active detectors.

13.3.3. Front End Electronics, Trigger and DAQ: The key components in the detector readout are the APD arrays and the custom front-end electronics (FEE) to read out the APDs. The baseline design has just over 540,000 channels to be read out. Our vendor quote is $43 for a sixteen-pixel APD array.

The custom electronics require the development of two custom ASICs incorporating a pre-amplifier, integrating amplifier, Cockroft-Walton voltage generators, multiplexer and ADC. The current estimate for production, fabrication and assembly of the FEE system is ~$4 dollars per channel, bringing the overall production cost of the readout to ~$8/channel.

The FEE, Trigger and DAQ system is the only one where the EDIA estimate has been made based on specific tasks rather than as a top down assessment of the manpower requirements.

13.3.4. Shipping: For the baseline design the shipping estimates include shipping (via truck) the empty modules from the two factories to the installation site, mineral oil (via truck) from Texas to the detector site and absorber boards from a rail site to the far detector site.

13.3.5. Installation: We have developed an installation procedure that enables us to determine the number of people that will be required to install the detector and how long it will take. We have built into the estimate three phases of the installation: ramp-up, steady state and ramp down.

The installation cost estimate also includes the M&S costs of the specialized tools and fixtures required for the installation process.

13.4. Other Project Costs

13.4.1. Far Detector Site, Building and Outfitting: The current cost estimate does not include any land acquisition costs. However, the building cost estimate does include general preparation of the site such as clearing and grading. A one-mile access road is also costed. Additional access roadway costs ~$750k/mile.

The building cost estimate has been based on a simple industrial style building with no overburden. To estimate costs we are using an algorithm developed by Fermilab Engineering Services Section (FESS), which allows us to specify the detector dimensions, the desired depth below grade of the detector, as well as an installation staging area. The building estimate includes basic utilities such as electrical distribution, fire protection and HVAC but does not include any detector specific structures or outfitting.

Outfitting costs have been estimated for the baseline detector based on a model for materials staging and handling. The outfitting cost estimate also includes the cost of a conceptual design for a detector support structure.

13.4.2. Active Shield: We have estimated the cost of an active shield to identify penetrating cosmic ray muons, installed above and on either side of the detector. The front and back of the detector do not have an additional shield since the active planes of the detector serve the same purpose. The veto shield is composed of active detector modules read out by the same electronics as the main detector. Inclusion of this veto shield requires the production of an additional 560 modules and the corresponding 17,000 channels of electronics. We have included the cost of a simple support structure for the veto planes and an estimate of the additional person-hours required for the installation.

13.4.3. Near Detector: The off-axis near detector cost estimate is based on the conceptual design described in Chapter 9. The near detector is structurally similar to the far detector except for its smaller transverse and longitudinal dimensions (3.7 m wide by 4.9 m high by 10 m long). We have scaled the unit costs of the particleboard and the active detector elements from those used in the far detector by the amount of material used, because the components are identical except for the smaller transverse dimensions of the absorber and the shorter extrusions. We have assumed that the near detector is read out with Hamamatsu M64 PMTs, with readout electronics identical to that used for the MINOS Near Detector. The 44 planes of liquid scintillator modules (22 horizontal and 22 vertical planes) contain 4620 tubes, which are read out by the same number of electronics channels.

13.4.4. Project Management and ES&H: We have estimated the manpower needs and corresponding cost of a project office that would oversee the management and administration of this project. This category of project management includes the Project Manager, a deputy, “Level 1” managers for the detector and the conventional construction, a project scheduler, budget officer and administrative assistants. A full time ES&H professional is also included in the project management budget.

13.4.5. Operating Costs: We have used experience from the NuMI-MINOS Project to develop a model that costs those expenses incurred during the construction of a project, but are not appropriate to be funded by capital equipment funds. These are items such as temporary building rental, utilities in the buildings, telephone and network ex-

penses, etc. During the construction of the MINOS far detector these funds were about $350,000 per year. Upon completion of the construction project, a budget was developed for the annual laboratory operating expenses which is currently ~$1.3M per year to support the laboratory with a crew of 8 persons. At this time it is not obvious how the laboratory for the NOνA Far Detector would have to be staffed, but we do not anticipate that such expenses would be in excess of those currently needed at the Soudan Laboratory.

13.5. Contingency Analysis

We are at a very early stage of the design of this experiment. Most designs are only conceptual and still require detailed engineering. Therefore we feel that our overall contingency must be quite large, i.e. approaching 50% or greater on many of the items. Several of our procurements are from foreign countries and the stability of the US dollar against the foreign currency cannot be assured. Technical issues such as the need for an overburden on the building lead to a huge uncertainty in the cost of the civil construction. Finally, given the overall uncertainty in the timescale and funding profile for carrying out this project, we have adjusted our overall contingency accordingly.

13.6. Schedule

Figure 13.1 shows a "technically driven" schedule for the off-axis experiment. In addition to technical considerations, we have assumed that R&D funding will be available (from Fermilab and/or the NSF) in early FY 2005 and that DOE construction funding will be provided at the beginning of FY 2007. If the Laboratory grants final approval in June 2005, the construction project for the experiment could be baselined in time for construction funding to begin in early FY 2007. The near detector and the first 15% of the far detector would then be ready to start recording data from NuMI beam neutrinos two years later, in the fall of 2008. The 50 kT far detector would be completed at the end of CY 2011. We realize that this schedule is aggressive but we believe that it is technically achievable and that the required resources could be made available.

13.7. Evolution of the Cost Estimate

The proposed detector for the NuMI Off-Axis Experiment is a large but uses only a few types of simple components. This simplicity makes the cost estimating exercise straightforward and easy to understand. Most of the mass of the detector is passive absorber and there is only one active detector system, all read out by a single system of electronics. The detector is a monolithic structure assembled from stacks of particleboard interleaved with active detector modules and constructed by carpenter-type skilled labor.

On the other hand, a penny per pound increase in the cost of the particleboard translates into an almost $1M increase in cost.

Likewise, the detector has 540,000 channels of electronics, currently estimated at ~$8/channel. An increase of $2/channel will add another million dollars. Hence, we feel that at this early design stage it is important to allocate contingency in a very conservative manner.

In selecting the liquid scintillator for the active detector technology we have been driven primarily on the basis of a comparison of the cost with two other active detector technologies, namely solid scintillator and glass RPCs, each of which we believe would perform satisfactorily. We are retaining both as possible backup technologies.

Table 13.2 summarizes the cost estimate comparison of the four active detector options that were considered when the baseline technology was chosen for this proposal.

13.7.1. Solid Scintillator Active Detector: The MINOS Far and Near Detectors are tracking calorimeters composed of alternating layers of iron and solid scintillator read out by wavelength shifting fibers and photomultiplier tubes. The far detector has been installed and is currently operating at the Soudan Underground Laboratory and the Near Detector is currently being installed on the Fermilab site. The 5.4-kiloton Far and the one-kiloton Near Detectors were constructed for a total project cost of $42M, including EDIA and overhead, of which $19M was the active detector system. This included the cost of the scintillator strips, module construction, manifolds, fiber, connectors and multi-channel PMTs and bases. The MINOS detectors include 285,000 kg of scintillator, 782,000 m of scintillating fiber and 32,000 channels of PMTs.

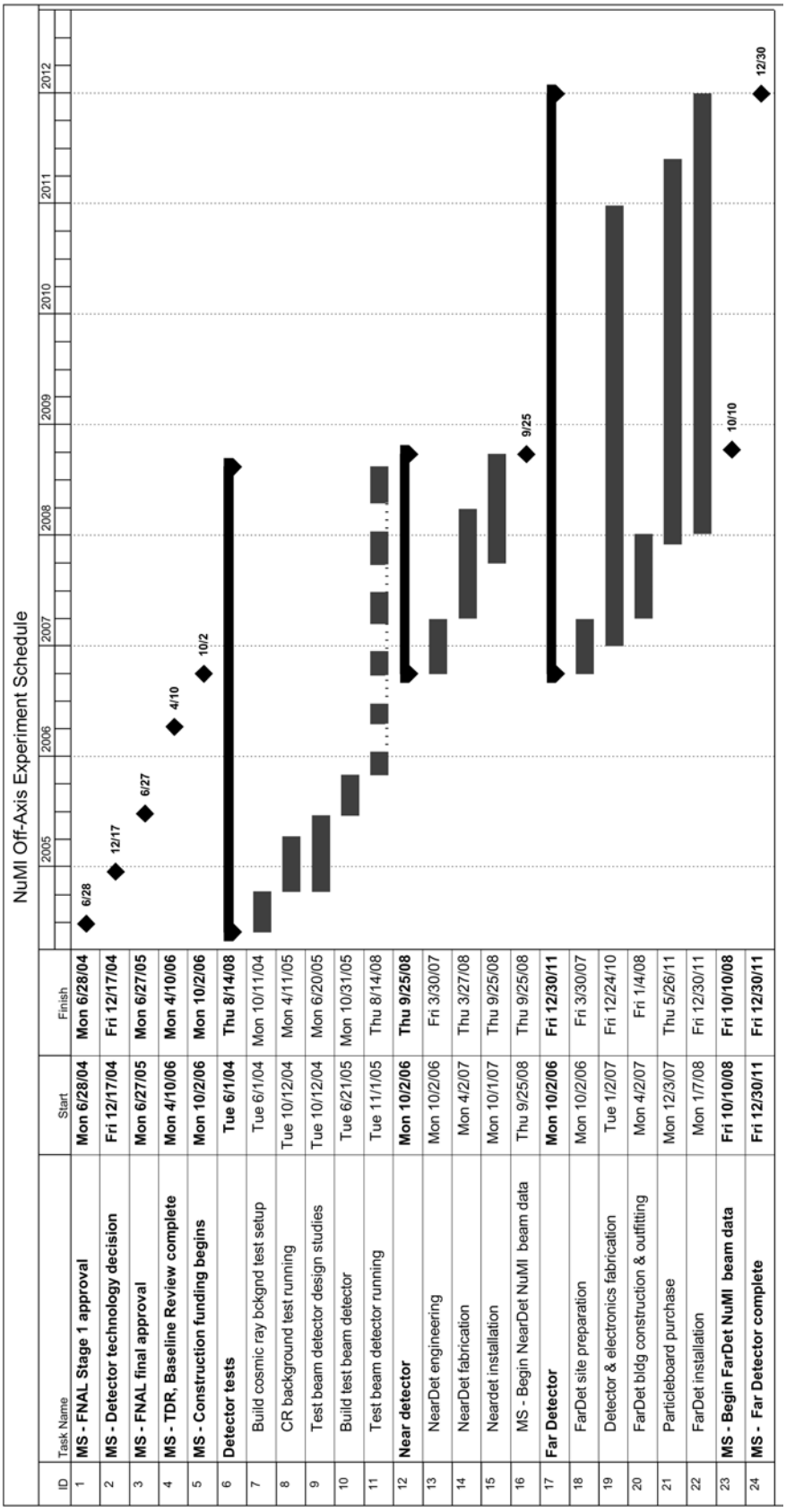

ID	Task Name	Start	Finish
1	**MS - FNAL Stage 1 approval**	**Mon 6/28/04**	**Mon 6/28/04**
2	**MS - Detector technology decision**	**Fri 12/17/04**	**Fri 12/17/04**
3	**MS - FNAL final approval**	**Mon 6/27/05**	**Mon 6/27/05**
4	**MS - TDR, Baseline Review complete**	**Mon 4/10/06**	**Mon 4/10/06**
5	**MS - Construction funding begins**	**Mon 10/2/06**	**Mon 10/2/06**
6	**Detector tests**	**Tue 6/1/04**	**Thu 8/14/08**
7	Build cosmic ray bckgnd test setup	Tue 6/1/04	Mon 10/11/04
8	CR background test running	Tue 10/12/04	Mon 4/11/05
9	Test beam detector design studies	Tue 10/12/04	Mon 6/20/05
10	Build test beam detector	Tue 6/21/05	Mon 10/31/05
11	Test beam detector running	Tue 11/1/05	Thu 8/14/08
12	**Near detector**	**Mon 10/2/06**	**Thu 9/25/08**
13	NearDet engineering	Mon 10/2/06	Fri 3/30/07
14	NearDet fabrication	Mon 4/2/07	Thu 3/27/08
15	Neardet installation	Mon 10/1/07	Thu 9/25/08
16	MS - Begin NearDet NuMI beam data	Thu 9/25/08	Thu 9/25/08
17	**Far Detector**	**Mon 10/2/06**	**Fri 12/30/11**
18	FarDet site preparation	Mon 10/2/06	Fri 3/30/07
19	Detector & electronics fabrication	Tue 1/2/07	Fri 12/24/10
20	FarDet bldg construction & outfitting	Mon 4/2/07	Fri 1/4/08
21	Particleboard purchase	Mon 12/3/07	Thu 5/26/11
22	FarDet installation	Mon 1/7/08	Fri 12/30/11
23	**MS - Begin FarDet NuMI beam data**	**Fri 10/10/08**	**Fri 10/10/08**
24	**MS - Far Detector complete**	**Fri 12/30/11**	**Fri 12/30/11**

Fig. 13.1: Proposed schedule for the NuMI off-axis experiment. This is approximately a technically driven schedule, in that a realistic timetable for the availability of funding has been assumed. The time scale is shown in calendar years.

A cost estimate for using a solid scintillator active detector for NOνA was made and found to be far more expensive than the two other alternatives that were considered, namely the liquid scintillator and the RPCs, mainly because of the cost of the extrusions and the photomultiplier tubes. Replacing the PMTs with APDs reduces the cost accordingly, but to date the cost of the extrusions keeps the solid alternative from being a competitive option. In MINOS the solid extrusions cost ~$10/kg. It is currently thought that this may be able to be reduced to $6-7/kg, but even this rate keeps the solid option prohibitively expensive.

In the cost comparison shown in Table 13.2, $6.4/kg and APD readout devices were used.

13.7.2. RPC Active Detector: A more cost competitive alternate technology for the active detector elements is glass resistive plate chambers (RPCs). A conceptual design for the NOνA Detector using RPCs contained in custom made modules, as described in the Appendix of this proposal, has been costed using the same methodology as for the baseline detector. The results of this costing exercise showed that the RPC active detector was more expensive than the liquid active detector for two main reasons. The first was because of the extra labor involved in the construction of the chambers and the containers. The second was because of the complex gas and high voltage systems. The RPC design incorporates readout of both the *x* and *y* coordinates, though it was noted that if an *x* or *y* readout scheme were adequate, there could be non-trivial cost savings in the readout board materials and the front end electronics. Proponents of the RPC technology are currently working on design modifications which would address these cost drivers and hence produce a more competitive alternative.

WBS		RPC 2-D (*x* and *y*) readout	RPC 1-D (*x* or *y*) Readout	Solid Scintillator	Liquid Scintillator
2.0	Far Detector				
2.1	Absorber	12.6	12.6	13.3	12.1
2.2	Active Detector	57.0	50.7	78.2	36.5
2.3	FEE, Trigger and DAQ	8.3	4.5	6.1	5.0
2.4	Shipping & Customs Charges	2.2	2.2	3.0	1.0
2.5	Installation	2.6	2.6	5.8	4.7
	Detector Sub-total	**82.7**	**72.6**	**106.4**	**59.3**

Table 13.2: Work Breakdown Structure and first generation cost estimate for the far detector using three active detector technologies. Note that these are "base costs" only and do not include EDIA, overhead or contingency. These costs were presented in the December 2003 Off-Axis Experiment status report and were the costs used in making the baseline technology choice. Cost estimates for the liquid scintillator technology have now been superceded and are presented in Table 13.1.

Appendix. RPC Detector Description

A.1. Overview

Detailed design studies for an off-axis experiment using both liquid scintillator and Resistive Plate Chamber (RPC) technologies were conducted in parallel during the past two years. Each design study produced a complete, stand-alone plan for constructing, installing and operating detectors for a 50-kiloton off-axis detector, including independent simulations, civil construction plans, cost estimates and schedules.

Chapter 6 describes how the selection of the liquid scintillator technology as the baseline for this proposal was made. This Appendix provides a description of the alternative RPC detector design at the same level as the technical description of the baseline liquid scintillator design in Chapter 7. Descriptions of RPC detector simulations, civil construction plans, cost estimates and schedules are not included here but are documented in detail elsewhere [1,2,3].

The low rate environment of a neutrino experiment makes it possible to utilize glass resistive plate chambers (RPCs) with strip readout as active detectors. Glass RPCs have an excellent track record (BELLE [4], HARP [5]) and should be distinguished from the traditional Bakelite RPC technology.

RPC chambers may be considered as detectors of choice for large area, low maintenance experiments in remote locations. Examples of uses or proposed uses of very large areas of RPC chambers include

- OPERA in Gran Sasso [6],
- ARGO experiment in Tibet [7],
- ATLAS and CMS at LHC [8],
- Indian Neutrino Observatory [9],
- Energy flow calorimeter [10] and muon detectors [11] for the Linear Collider experiment.

Attractive features of the glass RPCs include:

- Two-dimensional position information from every plane of detectors maximizes the topological information about neutrino events,
- Uniform response over the entire detector area,
- Very large induced signals (in streamer mode) require only simple and inexpensive electronics,
- Simplicity of construction leads to low production costs, typically \$100-150/m^2 [12].

An important advantage of the RPC technology is that it allows the detector to be constructed in a modular fashion. This facilitates detector construction and enables distribution of the production effort among a number of collaborating institutions. It could also allow the detector to be moved to another location, at least in principle, should the initial results indicate that moving would enhance the physics reach of the experiment.

The proposed RPC detector consists of 1200 identical 42-metric-ton modules, each 8.534 m (28 ft) long, 2.438 m (8 ft) high and 2.6 m deep. Modules are stacked in an array consisting of 75 planes along the beam direction, each plane being 2 modules wide and 8 high, as shown in Fig. A.1. This design provides a high degree of hermeticity; the gap at the center of the detector between two side-by-side modules is kept to 5 mm. The distance between the modules along the beam axis is chosen to simplify the stacking and unstacking procedure and is of the order of 5 cm. The dimensions of the full detector are 17.1 x 19.5 x 195 m^3.

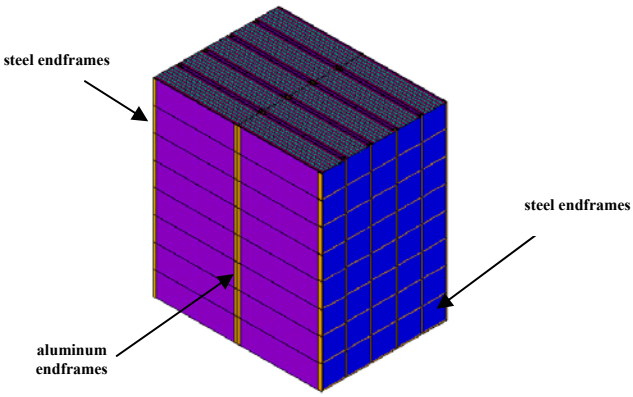

Fig. A.1: Five planes of the stacked modules.

Modules within each plane are interlocked by corner blocks (Fig. A.2), similar to those in commercial shipping containers. Endframes transmit the load of each module to its corner posts and those corner posts bear all the weight of modules stacked above. Readout electronics and gas distribution and recirculation lines are mounted on both sides of the detector and are readily accessible during the operation of the experiment.

Experience with large systems of glass RPCs indicates that there should be no need to replace or repair them. To further minimize any need for replacement, this design provides redundancy by constructing each active detector plane from two independent planes of chambers. Nonetheless, it is worth noting that each vertical column of modules can be unstacked without affecting its neighbors.

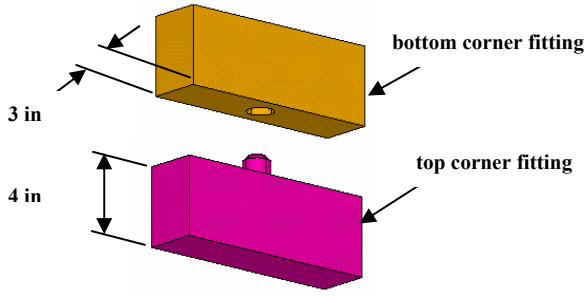

Fig. A.2: Module corner blocks. Aluminum blocks are embedded in the top and bottom of each composite column. The 3.8 cm diameter steel pins in top blocks fit into steel inserts in bottom blocks.

Table A.1 summarizes the parameters of the RPC far detector.

Detector mass	50 kT
Active detector mass	8.9 kT
Detector height	19.5 m
Detector width	17.1 m
Detector length	195 m
Absorber	Particleboard
Absorber density	0.7 g/cc
Active detector	Glass RPC
Active detector module	Single-gap (2 mm) RPC
Chamber height	2.425 m
Chamber width	2.844 m
Horizontal strip width	3.80 cm
Vertical strip width	4.44 cm
Strips per module layer	256
Chambers per module layer	6 = 3 double-gap RPCs
Module layers per module	12
Number of modules/plane	16
Number of module planes	75
Total number of modules	1200
Total number of module layers	900
Total number of chambers	43,200 double-gap RPCs
Total number of strips	3,686,400
Dead area fraction	1.98%

Table A.1: Parameters of the RPC far detector.

A.2. Detector Design

A.2.1. Module geometry: Each module consists of 13 vertical planes of absorber interleaved with double planes of RPCs. Two end plates, Fig. A.3, provide the mechanical rigidity of the module. In order to minimize the amount of dead material in the fiducial volume of the detector, the end plates located in the center of the detector are made of 0.3175 cm thick aluminum. The other end plates, located at the edge of the detector, are made of steel. The weight of the module is supported by two bottom angles, each 1.27 cm thick and 15.24 x 15.24 cm wide, and subsequently transferred to four corner posts. These posts ultimately transfer the load to the floor in a manner analogous to the posts in a standard shipping container.

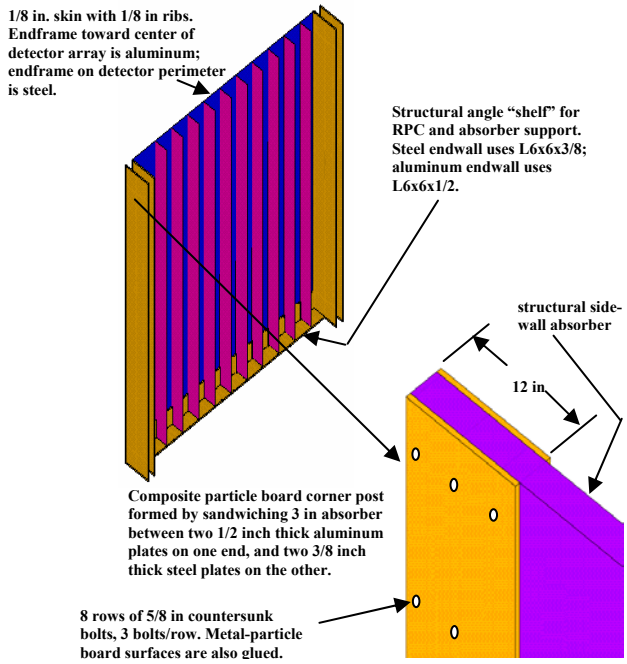

Fig. A.3: End plate and the corner post.

To minimize the dead material in the fiducial volume, the corner posts are composed of two aluminum plates, 1.27 cm x 30.5 cm x 243.8 cm, sandwiched around a 7.62 cm thick particle board. The corner posts are 1.27 cm longer than the vertical absorber height, leaving 6.3 mm vertical clearance between modules.

At the outer edge of the module, the plates are made of steel, which reduces the cost and reinforces the structure. These posts are part of the absorber structure and represent only a small degradation of the sampling of the detector: an addi-

tional 0.25 X_0 over 6% of the area of only 6% of the absorber planes.

To support the module weight, the bottom angles are reinforced by welding 10 ribs (aluminum at the center, steel at the periphery) 0.3175 cm thick and 15.24 cm wide. Absorber/RPC assemblies attached to the corner posts and to the ribs create a toaster-like structure, shown in Fig. A.4.

Module frames, after the proper checkout of the detector elements, will be shipped to the experimental site, where absorber planes are installed, as shown in Fig. A.5.

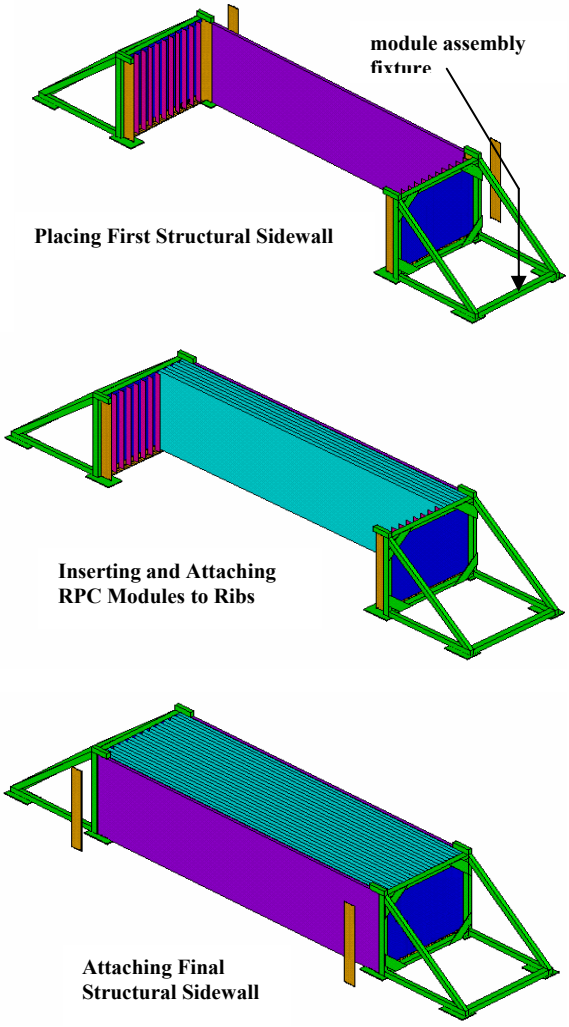

Fig. A.4: "Toaster"construction of a module.

A.2.2. Absorber planes: There are 13 absorber planes in a module. The central eleven are 10.2 cm thick and are assembled out of 4 boards 8.534 m long, 2.438 m wide and 2.54 cm thick, held together by glue and screws. The first and last absorber planes are constructed in a similar manner but are half as thick. Thus, when taken together with the first and last planes of preceding and succeeding modules, they result in a uniform sampling thickness across module boundaries. The absorber planes have 1.27 cm deep and 15.24 cm long notches at the bottom corners to accommodate the weight-supporting angles on which they rest. The support for the two end planes is provided by the corner posts, which are an integral part of them.

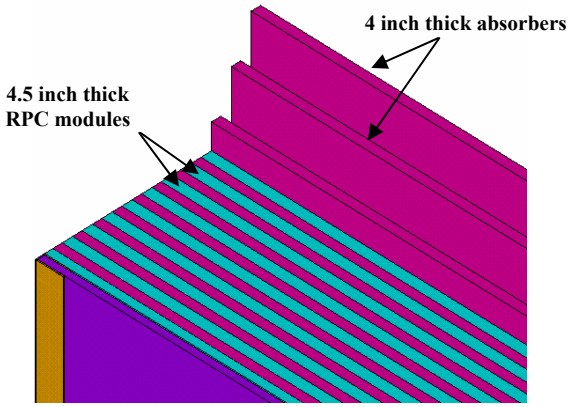

Fig. A.5: Insertion of the absorber planes into a "toaster."

A.2.3. Detector unit: A detector unit consists of two planes of RPCs sandwiched between two particleboards, the readout boards, one carrying the horizontal readout strips and the other the vertical ones. The boards also serve as protection for the glass chambers. A detector unit is 8.534 m long and 2.438 m high. It also has 1.27 cm deep and 15.24 cm long notches at the bottom corners to accommodate the weight-supporting angles on which they rest. The chambers cover an area of 8.534 x 2.425 m^2. Gaps between adjacent chambers and modules result in a total "dead" area fraction of 0.95%.

A.2.4. RPC chambers: Glass RPC chambers utilize inexpensive commercial float glass of high resistivity, 10^{12} Ω cm, instead of the traditional Bakelite used in other RPCs. An RPC, shown in Fig. A.6, is composed of two parallel glass electrodes, kept 2 mm apart by appropriate spacers. The gap between electrodes is filled with a suitable non-flammable gas mixture. The resistive coating on the outer surfaces of the glass connected to the HV power supply creates a strong electric field of about 4.5 kV/mm across the gap. An ionizing par-

ticle initiates a local discharge, which induces a signal on external pickup electrodes strips. The high resistivity of the glass and the quenching properties of the gas limit the discharge to a small area.

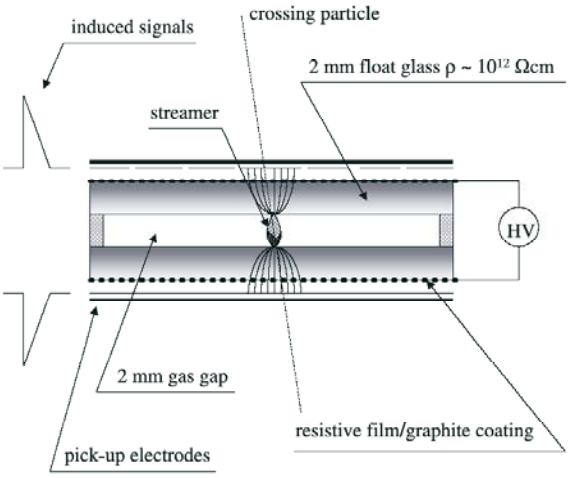

Fig. A.6: Glass RPC detector principle.

The development of an electron avalanche in an RPC gas gap has been simulated by a number of authors [1,13]. In the avalanche, a wave front of electrons moves rapidly (~100 microns/ns) toward the positively charged glass surface. On this time scale, the positive ions are nearly stationary. Simulations indicate that the separation of electrons and positive ions generates a dipole-like electric field extending beyond the gas gap, which induces a signal on the RPC readout strips.

Each pickup electrode is a plane of metallic strips glued to an insulating layer, on the other side of which is glued another metallic plane held at ground. This transforms the pickup strips into transmission lines, allowing the signals to be transported over long strip lengths. The induced pulses are typically 100-300 mV/50Ω with few ns time resolution. These large signals (100-200 pC in streamer mode) allow for the possibility of a variety of cost saving options in the readout electronics. Pickup electrodes are located on both sides of the chamber with strips oriented orthogonal to each other, so that two coordinates can be obtained from a single RPC gap.

Chambers for the NOνA detector are constructed in a manner very similar to the BELLE chambers, which have operated reliably for over four years at KEK. Each RPC plane is made up of three separate chambers with a daisy-chained gas supply and a separate high voltage and current read-back for each chamber. The 2.844 x 2.425 m^2 chambers are built from 3-mm thick float glass. A uniform distance between the glass plates, which defines the electric field in the chamber, is ensured by 2 mm thick Noryl spacers, 20 cm apart and glued to both glass plates. These spacers, glued in a maze-like pattern, serve several purposes:

• Ensure uniform gas flow over chamber area,
• Maintain uniform spacing of the glass plates,
• Protect the chamber from breaking in the event of a sudden change in atmospheric pressure.

The BELLE chambers were built with 2 mm glass. The thicker 3-mm glass in the NOνA detector allows the separation of spacers to be increased from 10 cm to 20 cm, while still withstanding a difference between the internal and atmospheric pressures of up to 20 cm of water. Reducing the number of spacers has two advantages. It reduces the dead space, and therefore the inefficiency, and also reduces the required manpower, and therefore the cost, of gluing the spacers.

The outer perimeter of the glass plates is sealed with a T-shaped extruded Noryl border to provide a gas-tight volume. The corners of the chambers are cut at a 45° angle. Triangular, injection molded plastic pieces glued in the chamber corners contain the gas inlet and outlet. Edge seals and corner cutouts result in a dead area fraction of 1.03% that, combined with the dead area between chambers, gives a total dead area fraction of 1.98%

The outer surfaces of the glass are painted with a resistive paint. High voltage leads are soldered to a copper pad glued to these resistive layers. An insulating plastic sheet covers the entire surface of the chamber.

A.2.5. Readout boards: Two particleboards, 8.534 m long and 2.438 m high, form the covers of the detector unit, with glass RPCs sandwiched between them. Both surfaces of both particleboards are laminated with thin copper foil glued to them. Copper foils on surfaces facing the chambers (inner ones) are cut into strips; the other surface is a ground plane which creates a transmission line.

Horizontal strips are 3.7 cm wide with 3.8 cm pitch, whereas vertical strips are 4.34 cm wide with 4.44 cm pitch. Thus one detector unit has 192 vertical readout strips and 64 horizontal ones.

A.2.*6. Performance of RPCs:* We have studied the performance of RPCs in the laboratory using a cosmic ray telescope and a set of small prototype

chambers. Each prototype is 25 x 25 cm^2 and is built out of two 2-mm thick glass plates. The chamber gas was a mixture of 8% isobutane, 61% R134a (tetrafluoroethane) and 31% argon. A three-fold coincidence of scintillation counters selected particles that traversed a stack of three chambers.

The efficiency of these chambers as a function of high voltage is shown in Fig. A.7. It reaches 92% at 8.3 kV and remains flat for several hundred volts beyond this voltage. The dead space introduced by the spacer can account for about 1-2% of the 8% inefficiency.

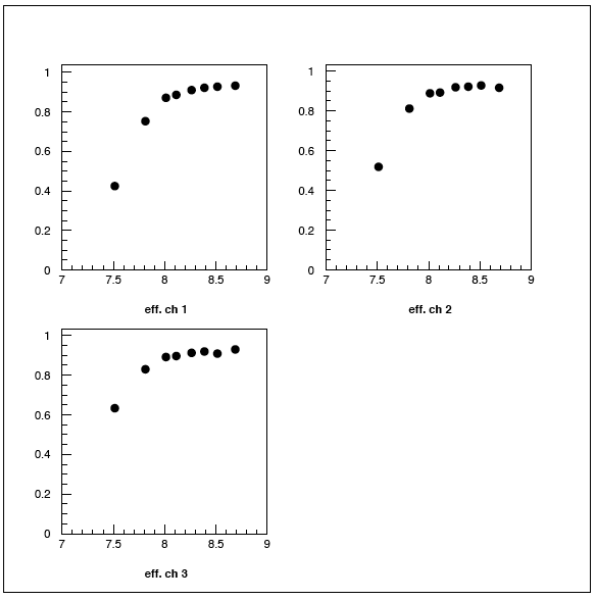

Fig. A.7: Efficiency as a function of high voltage for three chambers.

In BELLE, in order to compensate for the inefficiency of single chambers, two RPCs were sandwiched between a single pair of readout planes. This makes each readout plane sensitive to the sum of the pulse heights generated by the streamers in both RPCs. The positions of the spacers in the two RPCs were staggered so as not to overlap. A similar solution has been adopted for the NOνA detector, with two planes of RPCs positioned between two readout boards.

The pulse height induced by the streamer on the pad increases almost linearly with high voltage as shown in Fig. A.8.

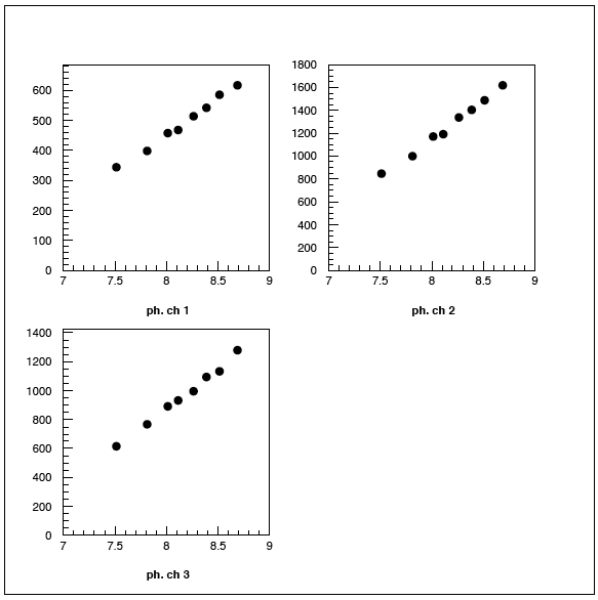

Fig. A.8: Pulse height as a function of high voltage for three chambers.

The dependence of the pulse height on the distance between the readout board and the RPC was measured using the same three chambers and is shown in Fig. A.9. Increasing this distance from 0 to 9 mm results in a factor of two loss in pulse height. Note that in the configuration in which two RPC planes are read out by a single pair of readout boards, each of the two chambers will be at this distance from one of the boards.

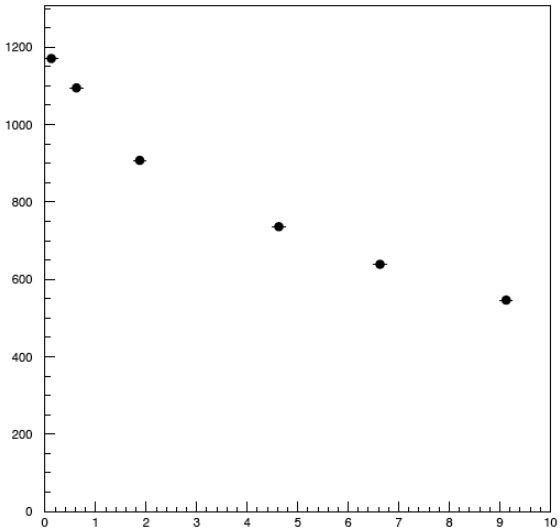

Fig. A.9: Pulse height vs. readout spacer thickness in mm.

The crosstalk, defined in this instance as the number of times a particle gives a signal in two

strips, the one it traverses and an adjacent one, was studied by using a chamber with a 3-cm-pitch strip readout instead of a single pad readout. It goes from 100% when the particle passes just at the edge of the adjacent strip to 3% when the particle is in the center of the neighboring strip.

A.3. Readout Electronics

A.3.1. Overview: When operated in streamer mode, RPC detectors produce a large pulse in response to gas ionization. The signals are large so that a significant voltage (100 mV or more) can be developed across a 50 or 100-ohm resistor. Because the measurement of events requires only recording hits in the detector, it is sufficient to use a simple discriminator as the front-end electronics, without the need for additional amplification or signal processing.

To facilitate event reconstruction, the output of each discriminator latches a timestamp, formed using local counters that receive common clock and counter reset signals from a global timing system. In this way, all timestamp counters across the detector are synchronized. When an RPC channel is hit the value of the timestamp counter is stored in a local memory for later readout. A block diagram of showing the functionality of the system is shown in Fig. A.10. The resolution of the timestamp is determined by the clock speed, which might be 100 ns (10 MHz.) The number of bits in the counter is determined by the frequency of the counter reset, which might be 1 Hz.

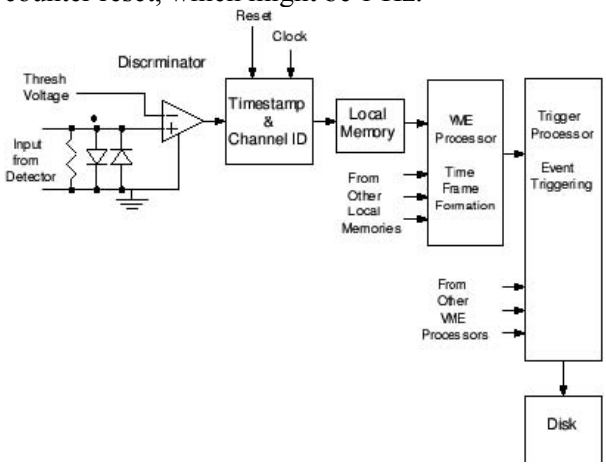

Fig. A.10: Functional block diagram.

Because the data rate is low, it is envisaged that no trigger hardware is needed. Instead, the formation of a trigger and the analysis of events are done using a series of processors. This is similar to the data acquisition system of MINOS. The initial sorting of hits by timestamps is done using a VME-based processor in the front-end crate. The processor would form "time frames" using the time-sorted data. The time frames are then sent to a trigger processor, which receives time frames from the entire detector. The trigger processor runs algorithms that look for tracks and discard noise hits. Those events that pass are either written to disk, or passed to another processor for further analysis.

The functionality of the basic system described above would be configured into the components shown in Fig. A.11 The basic components are: the Front-end ASIC, which processes the detector signals and forms timestamps; the Data Concentrator, which coalesces data streams from the front end ASICs to reduce the number of readout boards; and the Data Collector, which is a VME board that receives the data streams from the front end and makes data available for readout by the front end processor; and the Trigger Farm, which performs the event reconstruction, triggering, and event selection. These components are described below.

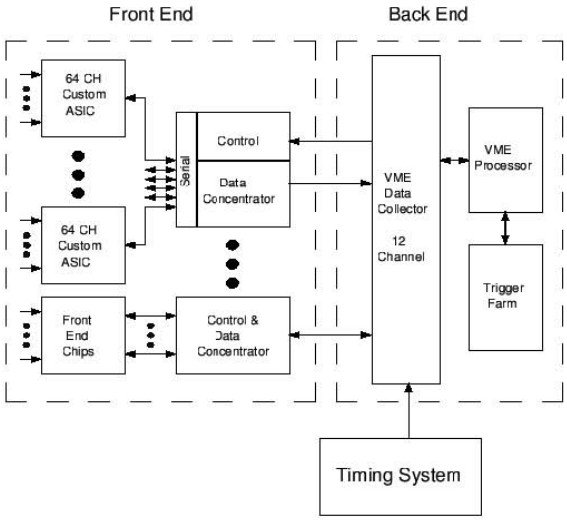

Fig. A.11: RPC electronics system block diagram.

A.3.2. Front-end ASIC: The high channel count and relatively simple front-end configuration make it practical to reduce the cost of the readout system by implementing the functionality in a custom front-end Application Specific Integrated Circuit (ASIC). The discriminator, timestamp counter, and local memory are easily realized in silicon. A block diagram of the ASIC is shown in Fig. A.12.

The ASICs would be mounted directly on the detector.

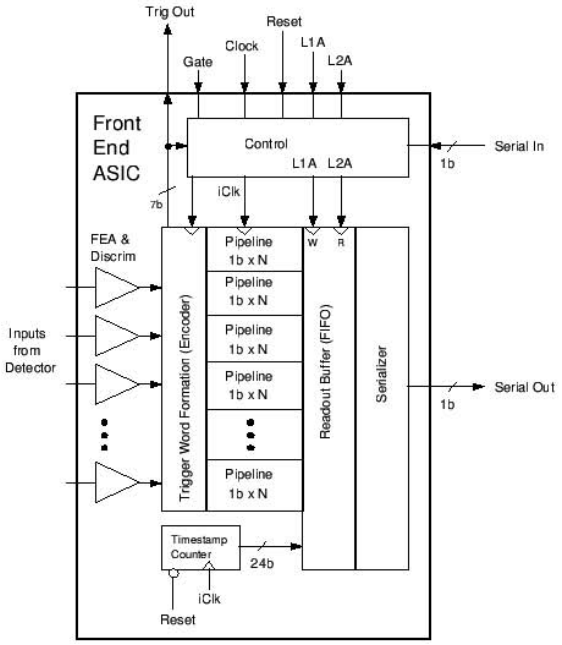

Fig. A.12: ASIC block diagram.

The ASIC would have 64 input channels. Each channel is composed of a fully differential instrumentation amplifier, an optional preamplifier with shaping, and a discriminator, as shown in Fig. A.13. There is a common threshold for all channels on the chip. Since the amplifier is differential, it may be used for either positive or negative input signals.

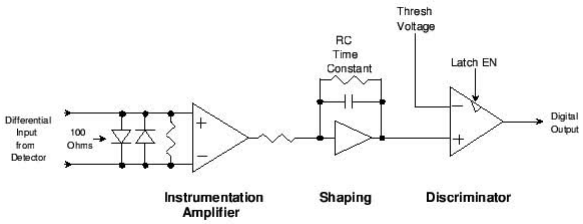

Fig. A.13: Front-end amplifier.

When a discriminator fires, the change in output state is clocked into a shift register at the fundamental clock frequency. The value of the timestamp register is also stored. At the output of the shift register, the decision is made to either write the data to a readout buffer or to reject it. The data are composed of the timestamp and the hit pattern. On-board logic can be configured to auto-accept any nonzero event, or to apply more complicated acceptance criteria.

Once data are stored in the readout buffer, they are serialized, buffered and transmitted out. An on-board UART controls the data transmission whenever the readout buffer is not empty. The readout buffer can store multiple events pending transmission. The output link runs at 100 MHz. An output word consists of 88 bits, which represents the state of the discriminators in one clock period. With control bits, the chip can transmit 1 event in 1 μsec.

A.3.3. Data Concentrator: We expect that the event rate from the NOνA detector will be low. To reduce the cost of back-end electronics, the system would have an intermediate Data Concentrator that coalesces the data streams from the front-end ASICs in an entire plane into one stream. A block diagram is shown in Fig. A.14. The Data Concentrator would reside on the detector, close to the front end ASICs. Essentially, this device is a multiplexer, although it must add an identifier to each data stream. It also must have buffering and flow control. The realization might be achieved using either an FPGA or a custom ASIC.

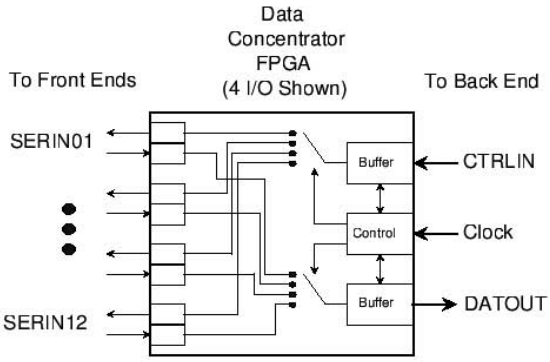

Fig. A.14: Data Concentrator block diagram.

An additional level of data compression may be achieved by concatenating the output data streams from several data concentrators into one "super concentrator." The output would run at 1 GHz and would be serially transmitted over fiber. There would be one super concentrator per module.

A.3.4. Data Collector: The serial data streams from the detector would be received by custom modules that reside in VME Crates, called Data Collectors. A block diagram is shown in Fig. A.15. It is implemented as a 9U by 400 mm card that has

12 inputs for serial data. The data are received, buffered and written into one of two readout buffers. One buffer is made available for reading by the VME processor in the crate while the other is used for writing new data. The state of the buffers changes at a set frequency, synchronized across the system, to facilitate the formation of "timeframes" of data. The Data Collector also provides control for the front ends, including the setting of threshold voltages, the fan-out of clock signals, and diagnostics.

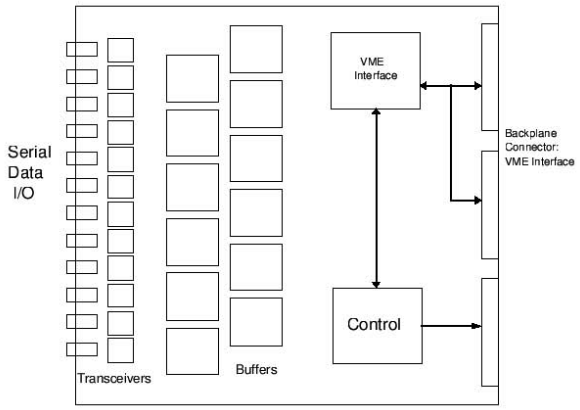

Fig. A.15: Data Collector block diagram.

A.3.5. VME crate: There would be multiple Data Collectors in a VME crate, as shown in Fig. A.16. The crate would also have a Timing Module for synchronizing the formation of timeframes of data. The Timing Module generates Interrupt Service Requests (ISRs) at a predetermined frequency.

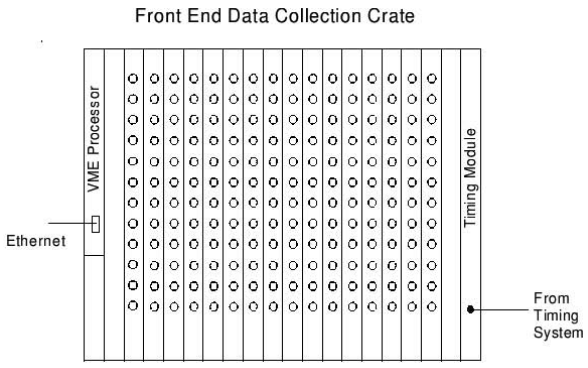

Fig. A.16: VME crate diagram.

When an ISR is received by the VME processor it reads data from the buffers on all of the Data Concentrators associated with that ISR. The next ISR would be generated to read from the other buffer. The VME processor collects blocks of data to form timeframes, which might be nominally 1 second worth of data. At the end of the formation of a timeframe, the VME processor would send the collected data to the Trigger Processor, where event reconstruction and triggering done.

A.3.6. Physical configuration on detector: Each detector module has 12 planes, each with 192 vertical strips and 64 horizontal strips. The horizontal strips come out to the vertical sides of the detector. The front-end ASICs for the horizontal strips reside on a small printed circuit board on the edge of the detector. There is one 64-channel chip per plane for the horizontal strips. The vertical strips have signals brought from the top of the plane over to the side of the detector by flex cables. Thus all of front-end ASICs are located on the side of the detector, providing easy access for servicing. The vertical strips are serviced by three 64-channel ASICs for a total of four chips per plane.

Each plane has one Data Concentrator and each module has one Super Concentrator, producing one serial data stream per module.

Each Data Collector has 12 inputs, requiring 100 Data Collectors to read out the 1200 detector modules. Assuming no limitations due to data rates or data transmission, this could be realized by having six VME crates, three per side.

A.4. RPC High Voltage System

A.4.1. Overview: The high voltage system is composed of distributed HV supplies, with one HV supply per RPC. The NOνA detector then requires approximately 104,000 individually controlled supplies, each with HV reference and current readback. The system is operated via a "slow control" serial network based on the CANbus commercial protocol. CANbus nodes contain multiplexed DAC and ADC modules to set RPC voltage and to read reference voltage and current. Current readback for individual RPCs is an important diagnostic of the operational state of an RPC.

In terms of the detector layout, each of the 1200 detector modules has one CANbus node and 72 Cockroft-Walton (C-W) high voltage supplies, with 6 C-W supplies per HV board. One HV board provides voltage to a full plane of double-layered RPCs, for a total of 12 HV boards per module.

Table A.2 contains the list of HV-system building blocks.

Item	Location	Total Count
C-W Supply	1 of 6 on a C-W board	86,400
C-W Board	1 of 12 on a detector module	14,400
CANbus node	1 per detector module	1,200
24V power supply	1 per 8 detector modules	150
PCI card	On C-W PC	3
PC	Control Room	1

Table A.2: Components of the RPC high-voltage system.

A.4.2. High voltage generation: Six C-W HV supplies are housed on a single 4-inch x 12-inch HV board that powers one plane of RPCs. The board is located on the outside edge of an absorber plane, adjacent to the RPC plane, and feeds HV to the RPCs on 20 kV insulated wires. Wires are soldered to the C-W board and to the RPC. Each wire is routed to an RPC in a groove at the top of the RPC carrier board.

A C-W supply is composed of diodes, capacitors and a transformer. Although the capacitors operate at 200 V the C-W boards use 500V-rated capacitors with a very reliable X7R dielectric (as opposed to the troublesome Z5U dielectric capacitors initially used on the ZEUS experiment).

A.4.3. HV system control: The system is controlled by a PC with three PCI cards (NI PCI-CAN/2). Each PCI card can communicate serially with 500 nodes via two CANbus controllers on the card. The CANbus node sets HV and reads back HV and current for all of the RPCs in a module. The node is a PC board that contains a CANbus processor and other electronics, including a multiplexed DAC and a multiplexed ADC. The processor communicates with the PCI card, executes routines and controls the multiplexed DAC and ADC modules.

Each C-W supply receives a command voltage from the multiplexed DAC to set the HV output. Two reference voltages, proportional to the high voltage and to the current, are read back by the multiplexed ADC. This information is relayed to the PC for monitoring and the possibility of fine-tuning the set point.

Physically, the node board has one connector for the CANbus serial communications bus, one connector for power input and twelve connectors to communicate with all C-W boards on a module.

A.4.4. HV system power: The power consumption per C-W supply is calculated as follows. An RPC draws 1 μA per square meter under good conditions and up to ~5 $\mu A/m^2$ before becoming inefficient. The RPC size is 6.9 m^2, so the current will range from 7 to 35 μA. In addition the no-load current is presently 40 μA (which can be reduced). An average total current of 50 μA is reasonable to expect, with possible surges up to 75 uA. The average power per C-W supply is ~ 400 mW with a maximum of 600 mW. If one includes inefficiencies, the resulting average power consumed is about 1 W per C-W, with surges up to 1.5W.

One module consumes ~72 W for C-W supplies plus ~8 W for the CANbus node, for a total of 80 W. Peak demand if all RPCs draw maximal current is 116 W. A vertical stack of 8 modules draws 640 W average and 928 W peak. Therefore, each vertical stack of 8 modules requires one 1 kW power supply. For a detector 75 modules deep, the number of low voltage power supplies is 150, each using 1 kW at +24V.

A.5. RPC Gas System

A.5.1. Overview: The RPC baseline gas used in our prototype tests and detector design study is a mixture of 8% isobutane, 61% R134a (tetrafluoroethane) and 31% argon. The total gas volume of the RPC detector is approximately 700 m^3, which is recirculated at a rate of one volume change per day. Individual RPC chambers are assumed to have leak rates of less than 10 cc/hr.

Gas will be stored and mixed at a central location from which it will be distributed through manifolds to the 1200 modules. On the supply side, gas within each module is distributed by 24 branch lines supplying 3 RPCs each. On the return side, gas is collected in manifolds, compressed and returned to the central supply.

Table A.3 summarizes the components of the gas system.

The design and fabrication will follow Fermilab PPD practices to ensure gas system reliability [14]. Gas system operation will be largely automatic, with provision for remote monitoring and operation, and gas supplies will be large enough to run for several months at the estimated leak rate.

Item	Features	Total Number
Mixing systems	3 flow meters, pressure control valve	2
Module supply manifolds	W/strainer, flow transmitter	1,200
RPC inlets	W/strainer, flow restriction	28,800
RPC outlets	Large enough for barometric pressure	28,800
Module return manifolds	W/pressure transmitter, relief valves	1,200
Return compressors	Dual compressor stations	10
Gas storage	Mixture storage vessel	1
Mass spec gas analysis	Analyzer with multiple sample points	1
Moisture analyzer	Local analyzers, one sample point	2

Table A.3: Components of the RPC gas system.

The gas system will mix, dry and recirculate the mixture through the RPCs. Flow restrictors will limit variations to less than 15% but flow balancing among RPCs is not critical. The main materials used for gas distribution will be stainless steel, copper or brass, with welded or brazed joints used wherever possible.

Estimates of gas system operating costs and applicable Federal environmental regulations are summarized in Ref. [15]. The gas mixture is non-flammable but precautions will be taken to ensure that the isobutane fraction does not exceed the nominal value. The isobutane storage area will be designed to meet applicable safety regulations.

A.5.2. Barometric pressure changes: Withstanding barometric pressure changes is a fundamental design requirement. The nominal RPC glass thickness of 3 mm is adequate to support the gas system overpressure [16] and pressure-relief valves will be used to ensure that pressure differentials do not exceed acceptable values.

Three criteria were used to specify gas system performance [17]:

• Contain gas for barometric pressure within one inch of mercury of the mean. The gas storage capacity is designed to handle this range so that gas will need to be vented only on rare occasions.

• Contain gas for changes in barometric pressure up to 0.75 inches of mercury/hour. Almost all barometric pressure changes are slower than this. The pumps and tubing will be sized to handle the resulting flow rate.

• Relief capacity for reductions in barometric pressure up to 2.5 inches of mercury/hour. Relief devices will vent directly to the atmosphere.

Pressure-relief devices will be installed on the exhaust of small groups of chambers (e.g., on individual modules) with pressures set to 2 inches of water (based on BELLE experience). Our baseline design uses check valves with the spring removed, a technique which has been shown to work reliably in previous Fermilab experiments.

A.5.3. Gas distribution, storage and circulation: Figure A.17 shows the gas distribution system. Gas from the mixing system, storage and RPC return feeds into a buffer tank, which supplies the detector through 40 branches. Each branch includes a pressure control valve, which allows flow to be varied, and is further split into thirty branches. Each of the 1200 branch lines includes a block valve, strainer and a flow transmitter.

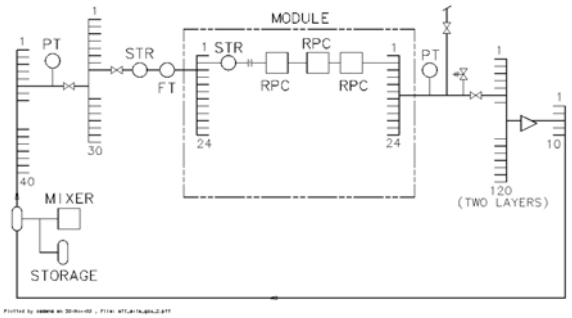

Fig. A.17: RPC gas distribution system.

At the module level the supply is split into 24 branches, each with a strainer and a flow restrictor allowing flows to be balanced to 15%. Each branch supplies 3 RPCs in series. Each module return line has a pressure transmitter, a vent valve, a relief valve and a block valve.

There are 10 return-side compressor stations, each serving 120 module lines. The discharge from the compressor stations is returned to the buffer tank.

The buffer tank is a 500 ft^3 stainless steel vessel used to receive or supply gas during barometric pressure swings. It also provides a buffer to allow brief mixing and purification interruptions. Tank pressure will vary between 0.5 and 35 psig.

The gas mixing system will use mass flow controllers to maintain the desired composition. Similar systems used at Fermilab for two, three and four component mixtures and have proven reliability. Two mixing systems will be used, one sized for filling and purging at 400 SCFH and the second for leakage makeup at 40 SCFH.

The component gases will be delivered and stored in tube trailers. For the estimated leak rate of 5%/day, an isobutane trailer would last 455 days, an R134a trailer would last 75 days and an argon trailer would last 73 days.

A.5.4. Control of gas contaminants: Gas contamination is minimized by material selection, cleaning and leak testing. To keep contaminants from accumulating to unacceptable levels, gas can be vented continuously at a low rate. For example, if a contaminant adds 10 ppm to the gas in one pass, then venting 5% of the circulated gas will limit the contaminant to 200 ppm. When substantial amounts of gas are vented as much of the R134a will be recovered as possible.

Stainless steel pipe, tubing and valves with welded connections would provide the cleanest and most robust distribution system. However we are studying less costly designs using brazed copper tubing for the smaller branches of the system. Connections that must be separated will be either quality compression fittings or O-ring fittings. Neoprene compatible with argon, isobutane and R134a has good long term characteristics and a usable temperature range.

Moisture is known to be detrimental to glass RPCs due to the formation of hydrofluoric acid. Dual molecular sieve driers will remove moisture, with one being regenerated while the other is in operation.

A.5.5. Instrumentation: An ABB IMSQ4 mass spectrometer or equivalent will measure contaminants and the mixture ratio. The mixture ratio data can be used to automatically adjust the mixing system. A single analyzer can be connected to multiple sample points through valves that can sequence automatically through the sample points.

Each module will have pressure and flow transmitters. An industrial programmable logic controller (PLC) will control mixing, circulation, alarms, etc. A commercial human machine interface (HMI) will be used to monitor and control the PLC and gas analyzer. It records historical data and can transmit alarms by Email or telephone. A web interface will be integrated with the HMI to provide remote access.

A.6. Detector Construction

A.6.1. RPC/Readout Board Assemblies: There are twelve RPC/Readout board Assemblies (RRAs) in each module. These are separated by eleven 10.2-cm thick particleboard absorber planes and bounded by two 7.6-cm thick absorber planes at the ends. An RRA is composed of six RPCs, three chambers adjacent in two layers, sandwiched between sheets of particleboard outfitted with readout strips and ground planes. Another 2.5-cm thick particleboard is attached to the outside of each of the two readout boards to protect the flexible circuit cables overlying the ground planes. The layout and assembly of these structures is shown in Fig. A.18 and described below.

The RPC signals are analyzed by discriminators packaged in a 64-channel chip (see Section C). Discriminator chips are mounted on interface boards that are in turn mounted directly on the readout boards. Signals from the readout board strips are collected and transported to connectors on the interface board.

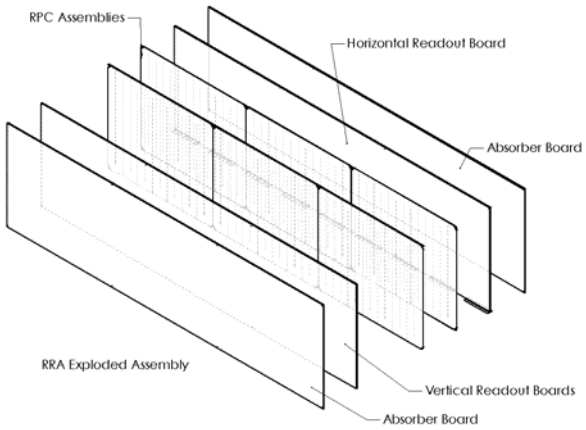

Fig. A.18: Components of an RPC/Readout Assembly (RRA).

A.6.2. RPC construction: Each RPC consists of two glass plates, 3 mm thick held 2 mm apart. The 2 mm separation is ensured by a T-shaped gas seal around the perimeter of the chamber and by a series of 2 mm wide long Noryl spacers positioned 20 cm apart. Each spacer extends from one side of the chamber almost all the way to the opposite side. Alternate spacers start on opposite sides of

the chamber. This maze-like configuration, together with the positioning of the gas inlets and outlets on opposite sides of the chamber, ensures a uniform flow of gas throughout the chamber.

RPCs are produced with a rectangular shape, 284 x 243 cm^2. The corners of each glass plate are cut away, with the resulting discards in the shape of isosceles triangles, 5 cm on shorter sides, as shown in Fig. A.19. The cut out corners are replaced with injection-molded Noryl pieces that act as a gas manifolds and have holes for positioning pins or through-bolts (Fig. A.20).

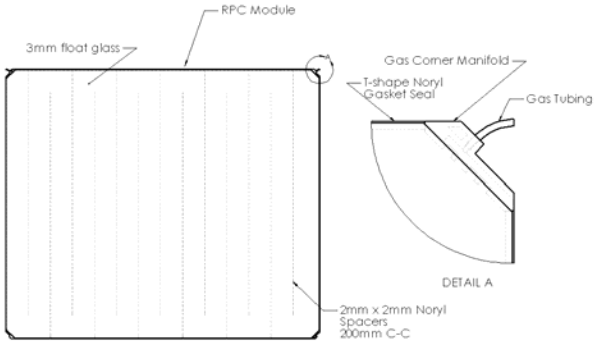

Fig. A.19: Glass RPC design with corner gas manifolds.

The outside faces of RPCs are coated with a conductive acrylic paint [18] resistivity ~1 MΩ/□ (100k-8M Ω/□). Two insulated wire stubs, rated to withstand 20 kV, are attached, one to each side. After installation on the readout board the wires are spliced to a longer harness of 20 kV wires and routed to the outside of the assembly, where a solder connection to the high voltage supply is made.

The injection-molded triangular gas manifolds are installed at the time when RPCs are assembled. Gas connections are made by gluing flexible tubing onto an injection-molded pipe stub. The gas manifolds also have holes for through-bolts and alignment/ retention pins.

A.6.3. Readout boards: Each RPC plane is sandwiched between two readout boards with the copper readout strips facing inward. The readout boards are made of particleboard absorber material with dimensions 243 x 853 x 2.54 cm^3. One board has 64 horizontal strips (3.80 cm pitch) and the other has 192 vertical strips (4.43 cm pitch), as shown in Fig. A.21. To create transmission lines, each board has a solid sheet of copper on the back side.

The horizontal readout boards support the RPCs with a built-in ledge along the bottom of the board. Also, gas tubing and high voltage wires are routed through or behind the top of the horizontal board. In the assembly process, RPCs are attached to the horizontal boards and later covered with vertical readout boards.

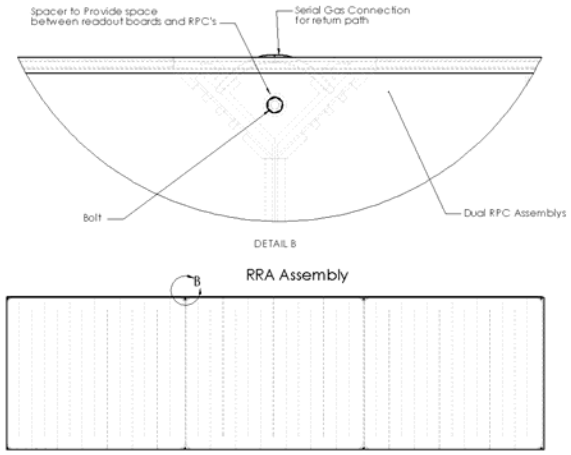

Fig. A.20: Assembly of three RPC chambers bolted to the readout boards.

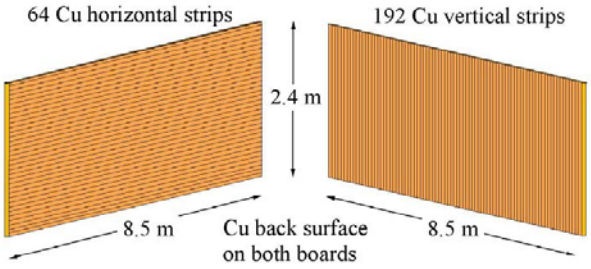

Fig. A.21: The readout boards required for each RPC plane.

The copper-strip side of a readout board is coated with a thin (0.5 mm) plastic sheet to insulate the readout strips from the HV side of the RPCs, to protect the copper strips during the assembly process (when RPCs slide over the strips) and to facilitate the sliding process.

A source for copper foil (1.34 m wide) has been identified. The least expensive unit area cost is obtained if the foil is purchased in a 17-micron thickness (1/2 oz/sq ft). We have contacted several firms who can laminate this foil to the 2.4 m wide

particleboard surfaces and cut the strips. One company gave us a budgetary cost estimate based on a custom-built production line. Strips would be cut with roller cutters specifically designed to prevent bulging on sides of the wedge blades, as shown in Fig. A.22. The company would set up the line and operate it for 2.5 years to produce a total of 28,800 boards plus spares.

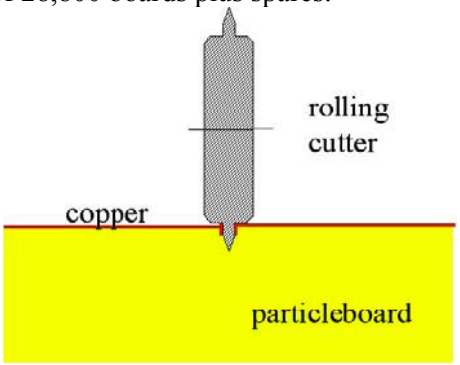

Fig. A.22: Detail of roller cutter shape.

We will use flexible (flex) circuit boards and flat conductor cables as the collection and transportation path, which will maintain the transmission line impedance of the readout strips (~100 Ohms).

A single-sided flex circuit board has been designed with 32 pads on the same pitch as the readout strips, as shown in Fig. A.23. The pads are glued face down on the end of the readout strips with an adhesive (3M z-phase) that makes connections through the glue, but does not conduct between pads. The circuit has a 32-channel fan-in to a neck 6.5 cm wide. Mating to the conductors at the neck of the flex circuit, and permanently attached by the manufacturer, is a 32-channel flat conductor cable with 1 mm wide conductors on a 2 mm pitch. The flat conductor cable will be made in seven different lengths; six for the vertical strips and one for the horizontal strips. The flex circuits bend over the edge of the readout board, lie flat and are taped against its back side, as is shown in Fig. A.24.

A dielectric sheet separates the flex circuit from the back conductor. The thickness of the dielectric is chosen to match the fan-in and cable impedance to the impedance of the strips. The cables must make 90° folds to reach the outer edge of the boards. In each fold it may be necessary to insert a conductor and (or) the proper thickness of dielectric to prevent an impedance mismatch. At the outer edge of the readout boards the flexible flat conductor cables will insert and lock into mating connectors on the discriminator interface cards. The flat conductor cable will extend beyond the end of the readout boards but will fold back into a 2.5 cm wide slot, created by attaching a another particleboard "spacer" on the back side of each readout board, as shown in Fig. A.25.

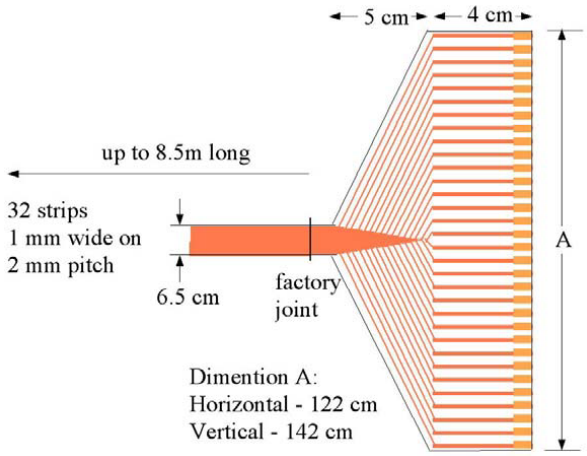

Fig. A.23: Signal collection flex-circuit and flat conductor cable (not to scale).

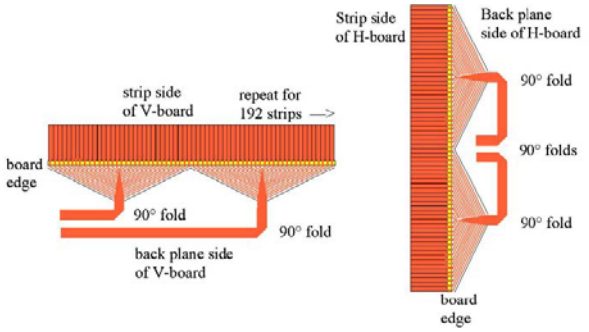

Fig. A.24: Routing of signals on backplane side of horizontal and vertical readout boards.

This arrangement is designed so that electronics can be mounted and tested on the RPC detector package. The package can then be inserted into an absorber module without modification.

A.6.4. Absorber boards: The absorber boards are made of particleboard with similar dimensions to readout boards, except that the absorber board attached to the horizontal readout board is 1.27 cm shorter (241.7 cm). The bottoms of the readout and absorber boards overlap exactly, but the top of the absorber board is 1.27 cm shorter than the readout board. This forms a slight depression that is used

to route gas tubing and high voltage wires to the RPCs.

The absorber boards are connected to readout boards with screws that penetrate about halfway into the readout boards through the ground plane. Care will be taken to avoid using screws in areas where flexible cable is routed.

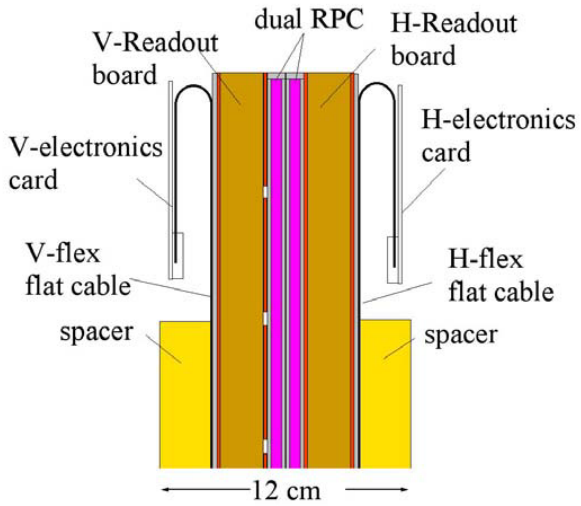

Fig. A.25: Routing of flat conductor cables to allow connection to discriminator interface cards.

A.6.5. RRA Assembly: The RRA assembly process starts with the following preassembled components:

- Horizontal readout boards,
- Vertical readout boards,
- RPCs,
- Gas tubing harness,
- High voltage harness.

A.6.5.1. Horizontal readout board units: To assemble a horizontal readout board unit (HRU), a horizontal readout board is first attached to an absorber board with screws. Recall that the absorber is 1.27 cm shorter on the top side and 2.54 cm longer on the "outside" to protect the front-end electronics connections. RPC support ledges are attached to the lower portion of the absorber board, with the requirement that the attachment is flush with the backside of the absorber (counterbored surface). The ledge supports the readout board and the eventual RPC layers and vertical readout board unit. Finally, the through-holes and alignment holes are drilled into the strip-side for eventual insertion of pins to align the RPCs via the injection-molded manifolds.

The HV and gas harnesses are attached to the HRU and, where appropriate, routed through the HRU to the inside surface for attachment to RPCs.

A.6.5.2. Vertical readout boards: To assemble a vertical readout board unit (VRU), a vertical readout board is first attached to an absorber board with screws. Recall that the absorber is 2.54 cm longer on the "outside" to protect the front-end electronic connections. Care is taken to avoid screwing through any flexible cables.

A.6.5.3. RPC layers on HRU: The next step in the assembly process is to attach RPCs to the HRUs. To facilitate this process a moveable table, equipped with height and tilt adjustment, is placed next to, and at equal height with, the supply of RPCs. The RPCs are installed by sliding them onto the HRU, so that the bottom of the RPC is in contact with the support ledge and the alignment holes are properly positioned. Temporary alignment pins are placed in the holes, gas connections between adjacent RPCs are made and high voltage wires are spliced to the harness. Conductivity is verified and gas connections are checked for leaks.

The table is lowered to facilitate sliding of the next layer of RPCs in a similar fashion. Temporary alignment pins are replaced with the longer, permanent pins. Gas and HV connections are made and tested. Note that the gas connections, although serial in one plane, are totally independent between layers.

Next, the VRU is lowered onto the RPC-HRU assembly on the table. The VRU is supported on the bottom with the HRU ledges. It is tied to the HRU using through-bolts in the clear areas provided at the corners of the RPCs.

The RRA assembly is ready to be rotated to a vertical orientation for insertion into the preformed absorber module.

The RPC chambers are supported from the bottom by support shelf attached to the readout boards, as shown in Fig. A.26.

A.6.5.4. HV, signal and gas connections: After the assembly of the RRA structure is completed, C-W supplies are mounted to absorber planes and the HV harness is soldered to the supplies. Readout front-end chips are attached at this point, along with the gas connections to the supply and vent manifolds.

Gas supply lines are routed inside a cutout in the HRU, as shown in Fig. A.27.

Front-end electronics chips are mounted on the sides of the readout boards and the signal cables are attached. The readout boards are 1.27 cm shorter than the backing absorber boards, so the absorber protects the electronics from accidental damage.

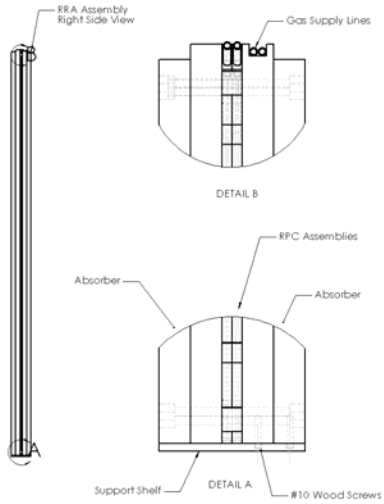

Fig. A.26: Side view of the RRA assembly showing the chamber support shelf in detail.

A.6.6. Detector Installation: To complete the installation of the far detector in 4 years we must construct and test 88 RPC chambers per day. Our construction plan assumes 4 RPC fabrication facilities with large floor space and highly automated equipment. Appropriate lifting fixtures for safe handling of large sheets of glass will require special attention. The completed RPCs will be assembled into RRAs at a rate of 16 per day, probably at two facilities that may be located away from the RPC fabrication sites. Separate fabrication facilities will provide a total of 30 readout boards and 16 Cockroft-Walton HV supply boards to RRA assembly facilities each day.

The far detector contains a total of 1200 modules, requiring 1.2 modules to be produced per day. Finished modules weigh about 42 tons, which is too heavy to transport over most roads and would require special equipment at the module assembly sites. We plan to assemble the module "toaster" structures at the two RRA assembly facilities. These facilities would build the toasters, attach the RRAs and electronics and perform final module quality control tests. The gas manifolds and wiring for electronics and high voltage power supplies are also installed. Substantial floor space and a 20 ton crane will be required to assemble the modules and load them onto trucks for shipping to the final site. The absorber boards would be installed in the modules at the detector site. Figure A.28 summarizes the flow of detector components during module construction.

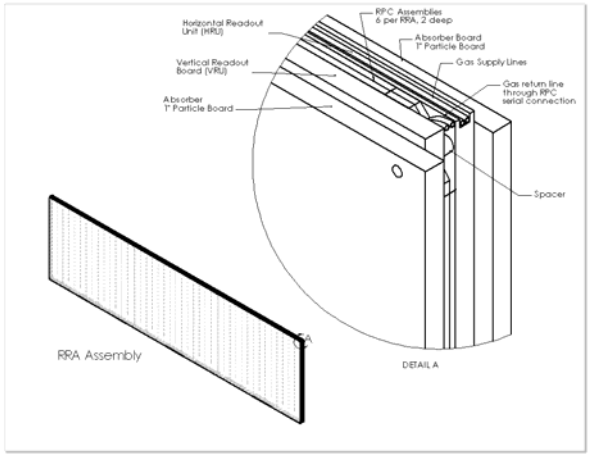

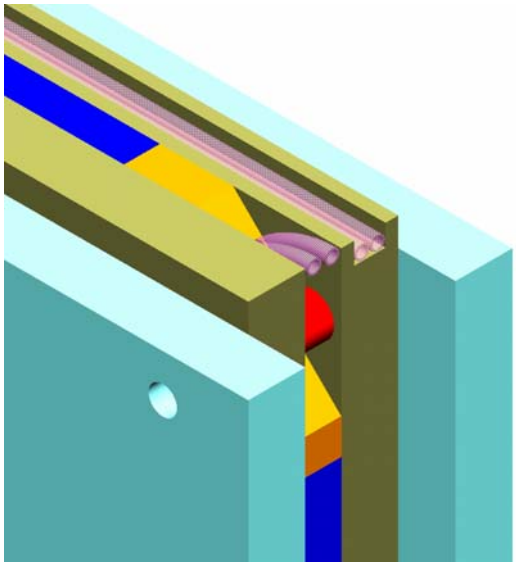

Fig. A.27: Corner of the RRA assembly showing the routing of the gas lines.

Final module testing includes the following:

- The RPCs will be tested for leaks and gas flow will be checked to ensure that the tubing to each set of chambers is clear.
- A high voltage test will ensure that the RPCs are functioning properly.

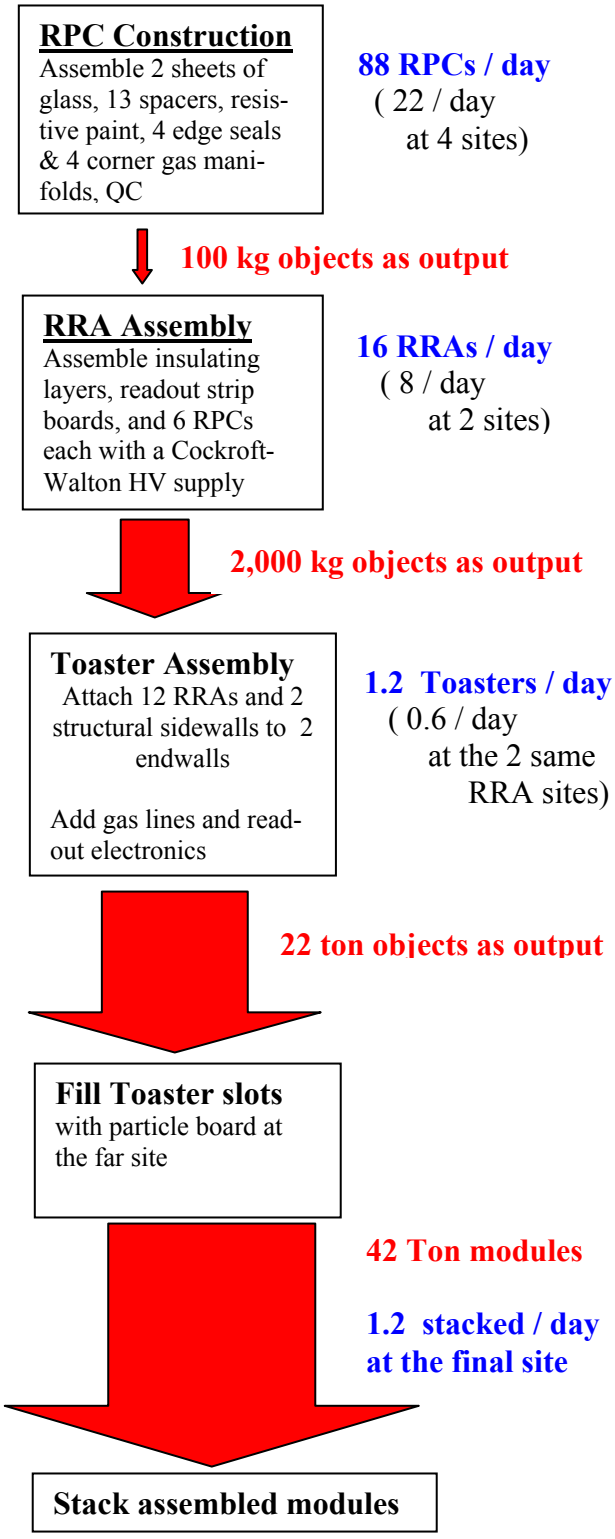

Fig. A.28: Flowchart of detector construction.

• The final test will use cosmic rays to measure performance after a module has been installed in the detector. Each module will be installed in such a manner that it remains accessible until this test is complete, allowing it to be removed for repairs before it is buried under other modules.

The detector is assembled as stacks of modules, 2 wide by 8 high by 75 deep, occupying a total area 17.1 m wide x 19.5 m high x 195 m long. In the initial stacking the modules will be installed to form a working face of the detector that is stepped like stairs. This will allow the final testing to proceed without burying untested modules.

Columns along each side of the detector footprint will support the gas manifolds and signal and power cables. These will be installed before the detector stacking begins. Each side of the detector will also have an aisle way just outside of the columns, wide enough to allow a man lift to make electrical and gas connections as detector modules are added.

Modules will be rigged by a 50-ton overhead crane using a spreader bar and four swivel hoist rings. This will require a total detector building height of about 33 m. Each module has corner blocks at the top drilled and tapped for the hoist rings. After a module is placed in position the hoist rings are removed and tapered pins are screwed in the same holes. These pins match the holes in the bottom corner blocks of the modules and are used for alignment as the modules are stacked up.

During and after assembly the detector will require access to the long (195 m) sides of the detector parallel to the neutrino beam. There will be two lanes on each side of the detector. The outside lane would be about 1 meter wide and primarily for personnel access. The inside lane next to the detector would be reserved for scissor-lifts, boom-and-bucket devices or a warehouse distribution system on rails (see Fig. A.29), allowing a person to reach the entire outside surface for installation, debugging, and maintenance of electronics, high voltage and gas systems. This lane would be approximately 3 meters wide. The access lanes add about 8 meters to the width of the building, giving a total width of 25 m.

The RPC detector building will need to be about 25 m longer than the 195 m length of the detector itself in order to provide room for final module assembly, component storage, the gas system and

office space. The overall building dimensions are then 220 m long x 33 m high x 25 m wide.

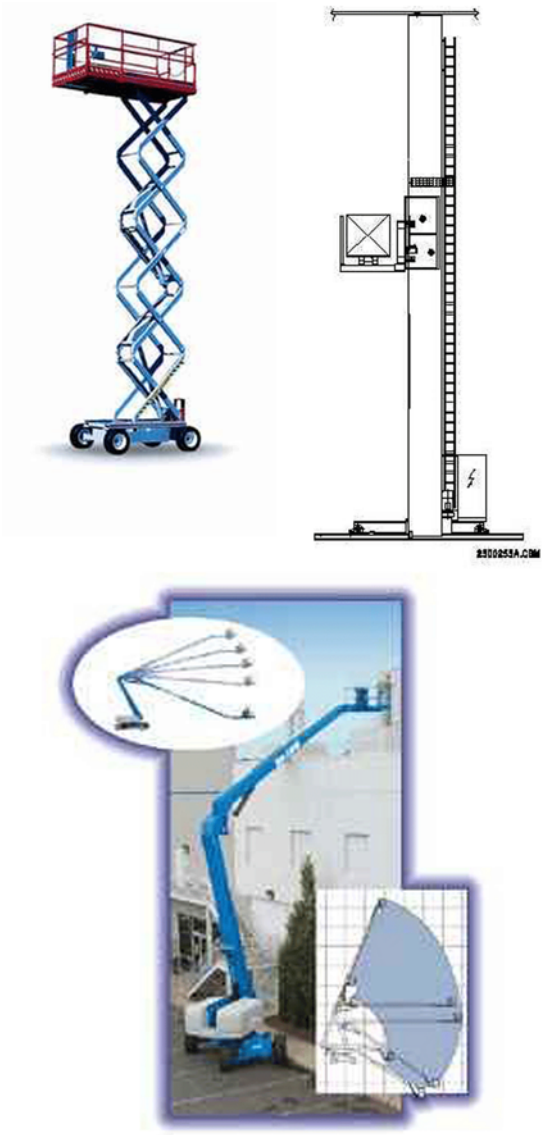

Fig. A.29: Possible access vehicles.

A.7. Cosmic Ray Active Shield

Just as in the Liquid Scintillator design, the RPC design would have a layer of counters on the top and the two long sides of the 75 rows of stacked modules. The side counters would be attached to the building walls, and the top counters would just be set on top of the stack of 8 modules, since there are no signals to access on the top of the detector. Each counter would be a RRA-like object with a double layer of single-gap RPCs. This would require an additional 3,000 RPCs of the type used in the RRAs.

A.8. Near Detector

The near detector could be constructed as a stack of 6 or 8 modules, of the same construction as the far detector modules, arranged in 3 or 4 walls, 2 modules high. Due to space limitations of the existing near-detector hall access tunnel, the modules would have to be shorter than far detector modules: about 4 m wide x 2.438 m high x 2.6 m deep.

Limitations of the access shaft to the Near NuMI hall will require the absorber planes and RRAs to be lowered separately and installed in modules underground. The upstream modules could have improved sampling at twice the frequency of standard RRAs.

A.9. RPC ES&H Considerations

Several ES&H issues must be considered during construction and operation of the RPC detector.

A.9.*1. Fire:* The detector's principal component is wood and represents a substantial fuel load at any module fabrication site as well as at the final location. Assembly methods chosen must ensure that module construction areas meet fire safety codes. It may be necessary to paint the completed assemblies with fire retardant paint to limit their flammability. Housekeeping will also be important because sawdust is more flammable than particleboard planes.

A.9.2. Lifting heavy loads: Every stage of construction will require commercial or specially designed lifting fixtures to handle the wood panels, glass plates and the finished modules. All fixturing must meet the requirements of the OSHA standards. These fixtures will include vacuum fixtures for handling glass plates and container-style lifting fixtures for the modules. Rigging procedures will be reviewed in advance of construction and operators will be trained in the proper use of hoisting equipment.

A.9.3. Glass handling hazards: Handling thousands of square meters of glass is potentially hazardous and procedures must be worked out to protect workers from the occasional broken pane. We will investigate the procedures and equipment used by large glass making companies to protect their employees.

A.9.*4. Oxygen deficiency hazard:* For such a large detector the inventory of gas is significant. Standard Fermilab ES&H rules will be followed to

minimize this hazard at every location, including all gas storage and mixing areas.

A.9.5. Fall protection: Because of the height of the detector fall protection must be provided for work on the detector stack. This might include railings and certainly will require harnesses and lanyards compliant with OSHA regulations. Crane cages, if used to lift personnel to the top of the detector, must be certified for that service. The present design does not include any need for working on top of the detector stack for operations or maintenance.

A.10. R&D for the RPC Design

As noted in Chapter 7, the RPC Design performance is essentially equal to the Liquid Scintillator Design performance and therefore our choice of Liquid Scintillator as the baseline is determined mostly on the issue of price (see Chapter 6). It follows that all our R&D efforts on the RPC Design will be aimed at reducing the price of this option. The object of the collaboration is to explore the parameter space of these options to find the best cost-performance solution.

A.10.1. RPC parameters: One simple change to the RPC design would be to construct "double gap" chambers using three pieces of glass instead of the four required for the two RPCs in each plane. This scheme has been used elsewhere and we will explore some prototypes for the NOνA detector. In this scheme the center glass plate polarizes so that each gap has the appropriate HV gap, requiring a higher voltage across the outside two glass plates.

The double layer of RPCs in each plane was motivated by our desire to have high efficiency in each plane and the efficiency reached in streamer mode is limited to 93 – 95%. However it is possible to operate RPCs in avalanche mode with very high efficiency, 98 – 99%. The signals become 100 times smaller, so this change would require amplification in the electronics. We are exploring this option in collaboration with the Linear Collider Hadron Calorimeter group and in fact are working with them to produce an ASIC which can handle either streamer or avalanche mode.

The readout strips in our basic RRA unit are made of copper laminated to particleboard. The cost of doing the lamination ourselves is high, estimated at about $ 0.30 per square foot of material and we need 6.5 million square feet. One possibility to reduce this cost would be to use a standard building material composed of polyisocyanurate foam faced with aluminum on both sides. The idea is to take advantage of existing large scale industrial output of a pre-laminated product. In this case we would be confronted with making grooves in the aluminum facing to form strips, but we think this can be done cheaply. The real R&D in this effort involves understanding how to make robust electrical connections to aluminum: the solution may be to capacitively couple our signals. Small prototypes will answer these questions.

A.10.2. HV System Simplification: The Cockroft-Walton HV system was designed so that each individual RPC chamber had its own HV and its own current readout. This count of 86,400 HV channels could be reduced by ganging the three or more RPCs in one Toaster module layer together.

A.10.3. Gas System Simplification: Our gas system design is based on copper tubing and we continue to search for a cheaper alternative. Any solution has to be impervious to water vapor.

In our base design described above, only 3 RPCs are in series in the gas flow. We could combine the gas path so that one set of six RPCs in a layer had only one gas path. The total pressure drop of the system would need additional study.

We could also simplify our gas system manifold on each Toaster module. The base design has expensive sintered metal filters and small diameter flow restrictors in front of each set of 3 RPCs. This was done to ensure balanced flow. We will do R&D on different schemes and understand just how balanced the gas flow has to be.

Our gas system design is a recirculating system with one volume change per day. BELLE operates with only 0.5 volume changes per day. If we could lower our gas flow a bit further than BELLE, say to 0.1 or 0.2 volume changes per day, we could eliminate the recirculation and just pass the gas once through each set of chamber, venting to the outside. This actually could be viewed as a less risky design since recirculation entails the possibility of contamination of the total detector if something goes wrong in just one small part. Our R&D here has to focus on how the pressure in the chambers can then track the outside atmospheric pressure without introducing oxygen and water vapor back through the outlet line (we contemplate

a long exhaust line with no bubbler, as was done 30 years ago on large spark chambers).

A.10.4. Exploring a Monolithic RPC Design: Our base RPC design is modular but there seems to be a cost advantage to construction of a monolithic device as is outlined for the liquid scintillator in Chapter 7. We will investigate if the assembly could be done at the far site using single RPCs and particleboard sheets as the basic units to be shipped.

A monolithic design should have a clear advantage in the number of electronics channels required for our RPCs. The modular design breaks the vertical strips into 8 parts, since we stack up 8 modules to make the detector. Reducing the number of vertical strips by 8 would result in a large cost savings.

A.10.5. Exploring a Commercial Modular RPC Design: Our design described in this Appendix relies on a custom container-like structure which is rather expensive to build. In addition, each of the modules is so large that we can't transport them on US Interstate highways unless they are only half-full. Thus this design suffers from having assembly labor at both ends of a transportation pipeline. This custom "container" was motivated by a desire to keep the dead space in each module at a minimum and our design did achieve a dead space of only 1.98 %.

Our "container-like" modules were in fact inspired by standard ISO Intermodal Shipping Containers. One avenue of R&D is to see if these existing cheap containers can be used in the NOνA detector. Standard ISO Containers come in a 20 foot long, 8.5 foot high, 8 foot wide version and can be purchased for about on-third the cost of our custom designed module. The one drawback of ISO Containers is that they have dead space at the bottom of the container where there are open pockets for forklifts and a steel grid structure which supports a plywood floor on the interior of the container. Use of these containers with such a dead area (about 7.5 %) between vertically stacked modules will require investigation of more sophisticated event tracking algorithms than those we have studied to date. The R&D here focuses on the tracking algorithms and simulations. We have to see if we can follow a track across a dead area and yet not label the track interruption as a real gap, which might be indicative of a π^0.

ISO Containers do have additional advantages other than the purchase price vs. custom-built price. One is that the steel gridwork and plywood floor support the load directly, allowing different building materials to be considered for the absorber. One such attractive alternate is gypsum in the form of sheetrock or drywall, which has the same density as particleboard. This material works well at supporting itself inside an 8 foot high container and appears to be available at about one-third the price of particleboard. This would give a very substantial cost savings. The radiation length of gypsum is about 37 cm vs. 53 cm for particleboard, but we will have to understand that effect on the detector performance.

A second additional advantage is that ISO Containers can be stacked quite high. They are routinely stacked 10 high on container ships and we have calculated they can be stacked 13 high on land when loaded at our projected density. This could make the profile of the NOνA detector higher and narrower. Our studies indicate that the detector enclosure building will be substantially cheaper (at equal volume) if the building is higher with a smaller footprint area.

We believe we can bring all these R&D ideas together into a few new RPC based re-designs during the next year. In each case, we have to develop a full model of detector construction and understand the attendant transportation costs and labor costs for assembly. We need the complete picture in hand to judge one scheme relative to another.

Appendix References

[1] A. Para, "RPC detector simulation using GMINOS," NuMI Off-axis Note 10, August 2003.

[2] A. Para, "Fiducial volume of the RPC detector," NuMI Off-axis Note 16, September 2003.

[3]A. Para, "Resistive Plate Chamber detector for NuMI off-axis experiment - collective work," NuMI Off-axis Note 21, September 2003.

[4] BELLE KLM detector group, Nucl. Instrum. and Meth. A 449 (2000) 112-124, and Nucl. Instrum. and Meth. A 456 (2001) 109-112.

[5] L. Linssen, HARP detector talk at the 7th Workshop on RPCs and Related Detectors, Claremont-Ferrand, France, Oct. 2003 (to be published in NIM A).

[6] A. Paolini, OPERA detector talk at the 7th Workshop on RPCs and Related Detectors, Claremont-Ferrand, France, Oct. 2003 (to be published in NIM A).
[7] C. Bacci et al. (ARGO experiment), Nucl. Instrum. and Meth. A 508 (2003) 110-115.
[8] P. Iengo (ATLAS) and B. Pavlov (CMS), talks at the 7th Workshop on RPCs and Related Detectors, Claremont-Ferrand, France, Oct. 2003 (to be published in NIM A).
[9] The Indian Neutrino Observatory design study is described by M. Goodman in "New Projects in Underground Physics," proceedings of the Tenth International Symposium on Neutrino Telescopes, Venice, Italy, March 2003.
[10] J. Repond, "A Digital Hadron Calorimeter for the Linear Collider," to appear in the proceedings of the 9th Pisa Meeting on Advanced Detectors, La Biodola, Isola d'Elba, Italy, May 2003.
[11] M. Piccolo, "Report on Muon Activities," ECFA Study of Physics and Detectors for a Linear Collider, Montpellier, France, Nov. 2003.
[12] C. Gustavino et al., "A glass resistive plate chambers for large experiments," Nucl. Instrum. and Meth. A 457 (2001) 558-563.
[13]W. Riegler, C. Lippmann, R. Vennhof, "Detector Physics and Simulation of Resistive Plate Chambers," Nucl. Instrum. and Meth. A 500 (2003) 144-162, and references therein.
[14] T. Gasteyer, "Fixed Target Gas Systems," Fermilab PPD Internal Note, March 1995.
[15] I. Ambats and R. Schmitt, "RPC Gas System Operation," talks given at the 2nd NuMI Off-axis Detector Workshop, April 2003. (http://neutrinooscillation.org/offaxisworkshop.htm)
[16] R. Schmitt, "Study of RPC Glass and Spacer Parameters," NuMI Off-axis Note 14, Aug. 2003.
[17] Data to determine these specifications were obtained from the National Climatic Data Center, International Falls (2002) and the Soudan 2 experiment, 80,200 measurements (1989 to 2001).
[18] G.C. Trinchero *et al*., Nucl. Instrum. and Meth. A 508 (2003) 102; M. Ambrosio *et al*., Nucl. Instrum. and Meth. A 508 (2003) 98.